

# Development of the Aerogel RICH counter for a super B-factory experiment

Shuichi Iwata

A dissertation submitted in partial fulfillment of the requirements  
for the degree of Doctor of Science

*Department of Physics, Tokyo Metropolitan University  
1-1 Minami-Osawa, Hachioji, Tokyo, Japan*

February, 2016



## Abstract

The framework to explain various phenomena in elementary particle physics, known as the standard model (SM), had completely been established by the experimental discoveries, such as the CP violation in a  $B$  decay system and the existence of a Higgs boson expected by the SM. The next aim in elementary particle physics is a search for the new physics (NP) beyond the standard model. As one of the approach of explore NP, a super  $B$ -factory experiment, which is named as Belle II experiment, is in construction stage at High Energy Accelerator Research Organization (KEK), Tsukuba, Japan. Belle II is the successor to Belle I is an asymmetric energy  $e^+e^-$  collider experiment, which uses the superKEKB accelerator, and the Belle II spectrometer. That is the project upgraded from the Belle experiment that contributed to discover the CP violation in  $B$  meson system and achieved the world record of the highest peak luminosity.

The aims of a super  $B$ -factory experiment is to search for NP and to investigate properties e.g. flavor structure of NP through a measurement of  $CP$  asymmetry and/or the branching fraction of rare  $B$  decays, which had been difficult to be measured in the previous  $B$ -factory experiments. For an example of the rare  $B$  decay,  $B \rightarrow \rho\gamma$  and  $B \rightarrow K^*\gamma$  are strongly suppressed in the SM because these processes are the Flavor Changing Neutral Current (FCNC) process, that is forbidden at the tree level diagram in the SM. They are, therefore, one of the good probe to verify the existence of NP. In order to discuss the effect of NP from those experimental result, we have to suppress the various experimental uncertainty at a super  $B$ -factory experiment.

Due to this requirement, a super  $B$ -factory commonly requires a high precision particle identification (PID) device. The  $\pi/K$  separation with high precision is required to discriminate  $B \rightarrow \rho\gamma$  and  $B \rightarrow K^*\gamma$  efficiently as they decays into  $\pi\pi\gamma$  and  $K\pi\gamma$  respectively. As a new PID device for the forward end-cap region of the Belle II spectrometer, an proximity-focusing type Ring Imaging Cherenkov (RICH) counter with a silica aerogel as a radiator, which is named Aerogel RICH (ARICH) counter, has been developed. The ARICH counter is designed to provide the  $\pi/K$  separation at  $4\sigma$  level in the wide momentum range up to about  $3.5\text{ GeV}/c$ . In particular, we aim to perform  $\pi$  identification with a few %  $\pi$  inefficiency and with a few %  $K$  fake probability at  $3.5\text{ GeV}/c$ , which is the highest momentum of daughter particles of a rare  $B$  decay.

The ARICH counter have 144-ch multi-anode Hybrid Avalanche Photo Detectors (HAPDs) as position sensitive photon detector. One of the important concern in the ARICH development had been the radiation hardness of an HAPD. We had studied and improved the HAPD to sustain the radiation damage during the 10-year Belle II operation of the expected fluence ( $< 10^{12}$  one MeV-equivalent neutrons/cm<sup>2</sup>) and the dose ( $< 100\text{ Gy}$  for  $\gamma$ -ray).

As the final step of the development, we constructed a prototype ARICH counter using the developed HAPDs and large size aerogel tiles. We verified the performance of the prototype ARICH counter using a beam test, and succeeded to observe the Cherenkov ring images for  $5\text{ GeV}/c$  electrons. As a result, we obtained the number of the detected

photoelectrons and Cherenkov angle resolution to be 10.71 photoelectrons per a track and 14.47 mrad, respectively.

In order to estimate the PID performance of the ARICH counter at Belle II, we demonstrated an event-by-event analysis based on the likelihood method for the beam test data. We defined the probability density functions (PDFs) for distribution of the accumulated Cherenkov angle and the number of detected photoelectrons per a track. In order to emulate  $\pi/K$  identification of the ARICH counter, we prepare the PDFs for signal and background assumption, and calculated likelihoods for an event of the beam test. Finally we estimate the  $\pi$  identification efficiency  $\varepsilon_\pi$  as 97.4% with the  $K$  fake probability as 4.9% at 3.5 GeV/ $c$ . We demonstrated that these results were mostly acceptable to our target performance.

In this thesis, we present the development of the ARICH counter especially the study and improvement of the HAPD, and estimation of the PID performance through a beam test using the prototype ARICH counter.

# Contents

<b>1</b>	<b>Introduction</b>	<b>1</b>
1.1	Short history of $B$ -factory experiments . . . . .	1
1.1.1	$CP$ violation in baryogenesis . . . . .	1
1.1.2	Discovery of the $CP$ violation in the $K$ meson system . . . . .	2
1.1.3	Origin of the $CP$ violation in the $K$ meson system . . . . .	3
1.1.4	Discovery of the $CP$ violation in the $B$ meson system . . . . .	5
1.1.5	Search for physics beyond the standard model . . . . .	10
1.1.6	Possibility of new physics models . . . . .	12
1.1.7	New physics search in the super KEK $B$ -factory . . . . .	13
1.2	Importance of particle identification device in the super KEK $B$ -factory .	19
1.3	Motivation of this thesis . . . . .	23
<b>2</b>	<b>The Belle II detector</b>	<b>24</b>
2.1	Upgrading to Belle II . . . . .	24
2.1.1	SuperKEKB accelerator . . . . .	24
2.2	Belle II sub-detectors . . . . .	28
2.2.1	Vertex detector: PXD, SVD . . . . .	28
2.2.2	Central Drift Chamber: CDC . . . . .	28
2.2.3	Particle Identification devices: TOP, ARICH . . . . .	29
2.2.4	Electromagnetic Calorimeter: ECL . . . . .	29
2.2.5	$K_L^0$ and Muon detector: KLM . . . . .	29
<b>3</b>	<b>Overview of RICH counters</b>	<b>33</b>
3.1	Introduction . . . . .	33
3.1.1	Cherenkov radiation . . . . .	33
3.1.2	Number of Cherenkov photons . . . . .	34
3.1.3	Radiators . . . . .	36
3.2	Classification of Cherenkov counters . . . . .	37
3.2.1	Threshold type Cherenkov counter . . . . .	38
3.2.2	Ring imaging type Cherenkov counter . . . . .	40
3.3	Particle identification using a RICH counter . . . . .	42
3.3.1	Definition of separation power of PID . . . . .	42
3.3.2	Maximum momentum for particle identification . . . . .	42
3.4	RICH counters in high energy physics . . . . .	43
3.4.1	HERMES RICH at HERA . . . . .	43

3.4.2	HERA-B RICH at HERA . . . . .	44
3.4.3	BaBar DIRC at PEP-II . . . . .	46
3.4.4	LHCb RICH at LHC . . . . .	46
3.4.5	Belle II TOP at Super KEKB . . . . .	49
<b>4</b>	<b>The ARICH counter</b>	<b>52</b>
4.1	Design concepts . . . . .	52
4.2	Photon detector . . . . .	53
4.2.1	Photo multiplier tube (PMT) . . . . .	54
4.2.2	Micro Channel Plate PMT (MCP-PMT) . . . . .	55
4.2.3	Multi Pixel Photon Counter (MPPC) . . . . .	56
4.2.4	Hybrid Photo Detector (HPD) . . . . .	56
4.3	Radiator . . . . .	57
4.3.1	Choice of the refractive index . . . . .	58
4.3.2	Thickness of a radiator . . . . .	59
4.3.3	Dual radiator focusing . . . . .	59
4.4	Structure design . . . . .	61
4.5	Readout electronics . . . . .	64
<b>5</b>	<b>Development of the HAPD</b>	<b>67</b>
5.1	Specifications . . . . .	67
5.2	Basic performances . . . . .	68
5.2.1	Detection of single photon . . . . .	68
5.2.2	Detection efficiencies . . . . .	69
5.2.3	Operation in a magnetic field . . . . .	69
5.3	Radiation hardness of HAPD and its improvement . . . . .	74
5.3.1	Neutrons . . . . .	74
5.3.2	$\gamma$ -rays . . . . .	74
5.3.3	Verification of improvements . . . . .	75
<b>6</b>	<b>Beam test using the prototype ARICH counter</b>	<b>77</b>
6.1	Prototype ARICH counter . . . . .	77
6.2	Overview of the beam test at DESY . . . . .	78
6.3	Measuring Cherenkov angle $\theta_C$ and number of photoelectrons $N_{pe}$ . . . . .	83
6.3.1	Reconstruction of the Cherenkov angle $\theta_C$ . . . . .	83
6.3.2	Cherenkov angle resolution $\sigma_\theta$ . . . . .	84
6.3.3	Cherenkov photon yield $N_{pe}$ . . . . .	88
6.3.4	Summary of prospectons . . . . .	91
6.4	Analysis . . . . .	91
6.4.1	Analyzed data set . . . . .	91
6.4.2	Single-track extraction . . . . .	91
6.5	Results . . . . .	95
6.5.1	Observation of a Cherenkov ring . . . . .	95
6.5.2	Measurement of Cherenkov angle $\theta_C$ . . . . .	95
6.5.3	Photoelectron yield . . . . .	96

6.5.4	Estimation of $\pi/K$ separation power . . . . .	96
<b>7</b>	<b>Evaluation of the PID performance</b>	<b>99</b>
7.1	Particle identification using a Likelihood method . . . . .	99
7.2	Definition of the Likelihood . . . . .	99
7.3	Construction of Probability Density Functions . . . . .	100
7.4	Analysis and results . . . . .	101
7.5	Discussion . . . . .	106
<b>8</b>	<b>Conclusion</b>	<b>108</b>



# Chapter 1

## Introduction

As the introduction of this thesis, the recent status of elementary particle physics and the motivation of a super  $B$ -factory experiment are overviewed. The importance of a Aerogel Ring Imaging Cherenkov (RICH) counter as a particle identification device in the Belle II experiment is also described.

### 1.1 Short history of $B$ -factory experiments

#### 1.1.1 $CP$ violation in baryogenesis

According to the current cosmology, our universe had been created about 13.8 billion years ago, which is estimated from astro-physical observations such as precise measurements of an anisotropy of the cosmic microwave background and measurements of the Hubble constant through Doppler shift of spectra of type II-a supernovae. Current universe is composed of huge number of galaxies, stars, planets such as our Earth and other creations like human-beings, which are composed of matters. However, at the creation of our universe particles and antiparticles were produced exactly same amounts, which could naturally produce same amount of matters and antimatters. A tiny unbalance between particles and antiparticles which is estimated to be  $10^{-9}$  was established within less than one second after the creation of our universe. This tiny unbalance can explain the ratio of the number of baryons to that of photons in the current universe. In 1967, a Russian physicist A. D. Sakharov pointed out that three conditions were necessary to make this matter universe [1]:

1. There should be an interaction that breaks baryon number conservation.

Since our universe started from vacuum, the total number of baryons should be zero at first. However, there are huge number of baryons now in our universe. Hence baryon number is not conserved, and we can expect that protons decay into leptons by this interaction ultimately.

2. There should be some mechanism that violates  $C$  and  $CP$  conservation.

Baryon number can be created when antibaryons decay into leptons, however baryons should decay into leptons in the same manner if  $C$  and  $CP$  are conserved. Hence  $C$  and  $CP$  violation are essential for baryogenesis.

3. Equilibrium condition should not be satisfied.

Even though baryon number is created through different decay rates for baryons and antibaryons, if equilibrium condition is satisfied, the reverse interactions can take place and eliminate the baryon number.

According to the Sakharov's condition, in order to create our universe that is only made with matters,  $C$  and  $CP$  conservation must be violated by same mechanism.

### 1.1.2 Discovery of the $CP$ violation in the $K$ meson system

Until the 1960's, physicists believed that any interaction process conserves the  $CP$  symmetry. However, in 1964, J. W. Cronin and V. L. Fitch discovered that  $K_L^0$ , which was believed to have the negative  $CP$  eigenvalue at that time, decays into two pions having the positive  $CP$  eigenvalue with a decay rate of  $2 \times 10^{-3}$  [2].

#### Definition of $CP$ operation

Here, in order to understand this  $CP$  violation in the neutral  $K$  meson system, let us review the mathematical definition of  $C$ ,  $P$ , and  $CP$  transformations in the system. A charge conjugation transformation is caused by the  $\hat{C}$  operator, which changes the sign of the electric charge, and other internal quantum numbers such as a Strangeness  $S$ . Therefore the  $\hat{C}$  operator toggles between a particle-state  $|f\rangle$  and an antiparticle-state  $|\bar{f}\rangle$ , and this operation is defined as follows:

$$\hat{C}|f\rangle = \eta_C |\bar{f}\rangle, \quad (1.1)$$

where  $\eta_C = \pm 1$  is a eigenvalue of the  $\hat{C}$  operator. When the eigenvalue to be  $\eta_C = -1$ , both state of  $|f\rangle$  and  $|\bar{f}\rangle$  are distinguished each other. In contrast, eigenvalue  $\eta_C = +1$  indicates that an antiparticle of  $|f\rangle$  corresponds to itself. Neutral  $K$  mesons  $K^0$  and  $\bar{K}^0$ , which consist of  $(\bar{s}d)$  and  $(s\bar{d})$ , respectively, are defined as  $\hat{C}|K^0\rangle = -|\bar{K}^0\rangle$  or  $\hat{C}|\bar{K}^0\rangle = -|K^0\rangle$ .

A parity transformation is caused by the  $\hat{P}$  operator, which changes sign of the particle momentum  $\vec{p}$  to  $-\vec{p}$ . Therefore, the  $\hat{P}$  operator inverts the moving direction of the particle  $\vec{p}$ . If the  $\hat{P}$  operator is applied to a state  $|f(\vec{p})\rangle$  twice, it returns to the initial state:

$$\hat{P}^2 |f(\vec{p})\rangle = \hat{P}\{\hat{P}|f(\vec{p})\rangle\} = \hat{P}\{|f(-\vec{p})\rangle\} = |f(\vec{p})\rangle. \quad (1.2)$$

Thus  $\hat{P}^2$  is an identical operator with the eigenvalue of  $\eta_P^2 = 1$ , therefore  $\eta_P = \pm 1$ . The eigenvalues of  $K^0$  and  $\bar{K}^0$  are known to be  $\eta_P = -1$  as they are pseudo-scalar particles. Therefore, we obtained  $\hat{P}|K^0\rangle = -|K^0\rangle$  and  $\hat{P}|\bar{K}^0\rangle = -|\bar{K}^0\rangle$ .

$\hat{C}\hat{P}$  operator is equivalent to the  $\hat{C}$  and  $\hat{P}$  operators applied to a state  $|f\rangle$  subsequently. Therefore, the  $CP$  transformations of  $|K^0\rangle$  and  $|\bar{K}^0\rangle$  are obtained as follows:

$$\hat{C}\hat{P}|K^0\rangle = \hat{C}\{\hat{P}|K^0\rangle\} = \hat{C}\{-|K^0\rangle\} = |\bar{K}^0\rangle, \quad (1.3)$$

$$\hat{C}\hat{P}|\bar{K}^0\rangle = \hat{C}\{\hat{P}|\bar{K}^0\rangle\} = \hat{C}\{-|\bar{K}^0\rangle\} = |K^0\rangle. \quad (1.4)$$

The transformation property of  $K^0$  and  $\bar{K}^0$  under the  $CP$  transformation indicates they can form  $CP$  eigenstates  $K_1$  and  $K_2$  as follows:

$$|K_1\rangle = \frac{1}{\sqrt{2}} (|K^0\rangle - |\bar{K}^0\rangle), \quad (1.5)$$

$$|K_2\rangle = \frac{1}{\sqrt{2}} (|K^0\rangle + |\bar{K}^0\rangle), \quad (1.6)$$

where  $CP$  eigenvalues of  $|K_1\rangle$  and  $|K_2\rangle$  are  $+1$  and  $-1$ , respectively. Thus we believe that the  $|K_1\rangle$  state can only decay into states with the  $CP$  eigenvalue of  $+1$  such as two pions, in contrast, the  $|K_2\rangle$  state can only decay the  $CP$  eigenstate with  $-1$  such as three pions.

Experimentally we can observe short-lived kaon  $K_S^0$  with lifetime of  $\sim 90$  ps and long-lived kaon  $K_L^0$  with lifetime of  $\sim 50$  ns as the eigenstates of the weak interaction. Because  $K_L^0$  was believed to be the  $CP$  eigenstate with  $-1$ , it can only decay into a state with the same eigenvalue, i.e. three pions. But Cronin and Fitch had been observed  $K_L^0$  decays into two pions with the  $CP$  eigenvalue of  $+1$ . That result indicates that  $K_S^0$  and  $K_L^0$  consist of the combination of  $CP$  eigenstates with the small complex parameter  $\varepsilon$  as follows:

$$|K_S^0\rangle \equiv \frac{1}{\sqrt{1+|\varepsilon|^2}} (|K_1\rangle + \varepsilon|K_2\rangle), \quad (1.7)$$

$$|K_L^0\rangle \equiv \frac{1}{\sqrt{1+|\varepsilon|^2}} (\varepsilon|K_1\rangle + |K_2\rangle). \quad (1.8)$$

$\varepsilon$  determines the indirect  $CP$  violation in the neutral  $K$  meson system. The  $\varepsilon$  of non-zero indicates the  $CP$  symmetry is violated in the neutral  $K$  meson system at least.

### 1.1.3 Origin of the $CP$ violation in the $K$ meson system

In order to explain the  $CP$  violating interaction in the neutral kaon system a number of theories were proposed. L. Wolfenstein proposed to introduce the super-weak model in order to explain the  $CP$  violation within the  $K^0$ - $\bar{K}^0$  mixing in 1964 [3]. The super-weak interaction has a very weak Hamiltonian, which can introduce a phase which violates the  $CP$  symmetry and contribute to only  $s$ -quark transition with a Strangeness exchange  $\Delta S = 2$ , i.e.  $K^0$ - $\bar{K}^0$  mixing. In 1973, another theoretical explanation for the origin of  $CP$  violation, which is known as the Kobayashi-Maskawa (K-M) model, was proposed by M. Kobayashi and T. Maskawa [4]. Their proposal indicates that one irreducible complex phase remains in the quark-mixing matrix, which is known as the Cabibbo-Kobayashi-Maskawa (CKM) matrix, when six types of quarks exist. Due to the existence of that complex phase in the mixing matrix, the  $CP$  symmetry in the quark-sector can be broken.

Both proposals predict the  $CP$  violation through the  $K^0$ - $\bar{K}^0$  mixing, i.e. the indirect  $CP$  violation parameter  $\varepsilon$  to be non-zero. The decay process, which has  $\Delta S = 1$  such as  $K^0 \rightarrow \pi\pi$ , can also violate the  $CP$  symmetry, but the super-weak model does not contribute to the  $\Delta S = 1$  decay, then this model predicts that the direct  $CP$  violation parameter  $\varepsilon'$  should be zero. While the K-M model can explain the  $\Delta S = 1$  decay process due to the quark-mixing matrix, and it predicts  $\varepsilon' \neq 0$ . NA48 experiment [5] at CERN in 1997–1999 and KTeV experiment [6] at Fermi Lab. in 1996–1997 established  $\varepsilon' \neq 0$ . Thus the super-weak model had been rejected and the K-M six quark model is considered to be most promising theory to explain the  $CP$  violation in the kaon system. However, in order to confirm the K-M model other  $CP$  violation phenomena than the kaon system had been desired.

### Kobayashi-Maskawa model

The K-M model and its mathematical expressions are described in the following. In order to explain the  $CP$  violation in the  $K$  meson system, Kobayashi and Maskawa introduced the  $3 \times 3$  orthogonal matrix  $V_{\text{CKM}} = \{V_{ij}\}$  named as CKM matrix, and the matrix is defined as follows:

$$\begin{pmatrix} d' \\ s' \\ b' \end{pmatrix} = V_{\text{CKM}} \begin{pmatrix} d \\ s \\ b \end{pmatrix} \equiv \begin{pmatrix} V_{ud} & V_{us} & V_{ub} \\ V_{cd} & V_{cs} & V_{cb} \\ V_{td} & V_{ts} & V_{tb} \end{pmatrix} \begin{pmatrix} d \\ s \\ b \end{pmatrix}, \quad (1.9)$$

where  $(d, s, b)$  and  $(d', s', b')$  indicate the down-type quark fields in the mass eigenstates and the  $CP$  eigenstates, respectively. In general, these elements  $V_{ij}$  are complex numbers. In order to evaluate the matrix elements, conventionally we use the Wolfenstein parametrization for the CKM matrix as follows:

$$V_{\text{CKM}} = \begin{pmatrix} 1 - \lambda^2/2 & \lambda & A\lambda^3(\rho - i\eta) \\ -\lambda & 1 - \lambda^2/2 & A\lambda^2 \\ A\lambda^3(1 - \rho - i\eta) & -A\lambda^2 & 1 \end{pmatrix} + \mathcal{O}(\lambda^4), \quad (1.10)$$

where  $\lambda$ ,  $A$ ,  $\rho$ , and  $\eta$  are real parameters. In particular,  $\lambda$  is known to be 0.22 which is equivalent to  $\sin \theta_c$  with the Cabibbo angle  $\theta_c$ . Conventionally it is feasible to ignore higher order factors of  $\mathcal{O}(\lambda^4)$  in  $V_{\text{CKM}}$ . In Eq.(1.10),  $V_{ub}$  and  $V_{td}$  involve the complex phase  $\eta$ , thus these elements are source of the  $CP$  violation in the quark sector.

Because  $V_{\text{CKM}}$  is a unitarity matrix, the matrix satisfies the following relation:

$$V_{\text{CKM}} V_{\text{CKM}}^\dagger = \begin{pmatrix} 1 & 0 & 0 \\ 0 & 1 & 0 \\ 0 & 0 & 1 \end{pmatrix}, \quad (1.11)$$

where  $V_{\text{CKM}}^\dagger = \{V_{ij}^*\}^T$  is the Hermitian conjugate of  $V_{\text{CKM}}$ . From Eq.(1.11), the following

six relations are obtained:

$$V_{ud}V_{us}^* + V_{cd}V_{cs}^* + V_{td}V_{ts}^* = 0, \quad (1.12)$$

$$V_{ud}V_{cd}^* + V_{us}V_{cs}^* + V_{ub}V_{cb}^* = 0, \quad (1.13)$$

$$V_{us}V_{ub}^* + V_{cs}V_{cb}^* + V_{ts}V_{tb}^* = 0, \quad (1.14)$$

$$V_{cd}V_{td}^* + V_{cs}V_{ts}^* + V_{cb}V_{tb}^* = 0, \quad (1.15)$$

$$V_{ud}V_{td}^* + V_{us}V_{ts}^* + V_{ub}V_{tb}^* = 0, \quad (1.16)$$

$$V_{ud}V_{ub}^* + V_{cd}V_{cb}^* + V_{td}V_{tb}^* = 0. \quad (1.17)$$

These unitarity relations are expressed as six triangles in the complex plane, which are called unitarity triangles as shown in Fig.1.1. These triangles are used for tests of the K-M model to measure whether every triangle is completely closed.

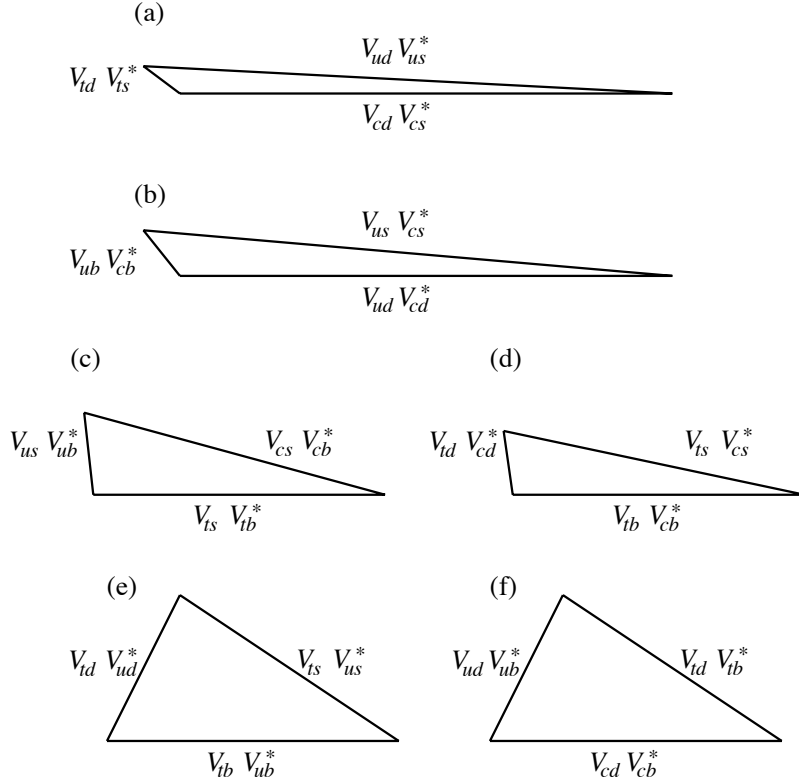


Figure 1.1: Unitarity triangles led by Eq.(1.12)–(1.17) corresponding to (a)–(f), respectively.

#### 1.1.4 Discovery of the $CP$ violation in the $B$ meson system

In 1980, A. Carter, I. I. Bigi, and A. I. Sanda pointed out that the sizable  $CP$  violation can be observed in the  $B$  meson decays in contrast to the case of the  $K$  decays. In order to measure the  $CP$  violation in the  $B$  meson system, specific  $B$  meson decay processes

were suggested. For example,  $B^0 \rightarrow J/\psi K_S^0$  is one of the most promising decay processes to measure the  $CP$  violation in the  $B$  meson system.  $B^0$  ( $\bar{B}^0$ ) can directly decay into  $J/\psi K_S^0$  as shown in Fig. 1.2. In addition, another decay process should be also considered such that  $B^0$  ( $\bar{B}^0$ ) exchanges to  $\bar{B}^0$  ( $B^0$ ) through the  $B^0$ - $\bar{B}^0$  mixing as shown in Fig. 1.3 and decays into  $J/\psi K_S^0$ .

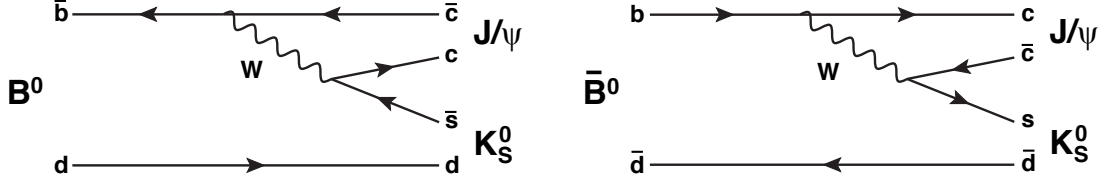


Figure 1.2: Two Feynman diagrams representing the decay of  $B^0(\bar{B}^0) \rightarrow J/\psi K_S^0$  through a tree diagram.

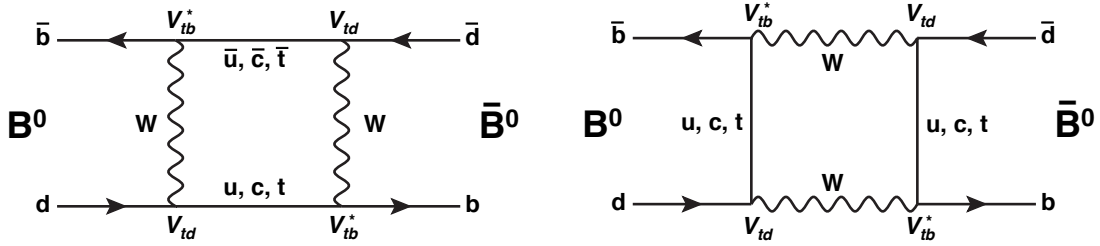


Figure 1.3: Two Feynman diagrams for the  $B^0$ - $\bar{B}^0$  mixing.

These two processes have different phases and interfere with each other. Therefore the  $CP$  asymmetry appears could manifest. The interference effect can be observed as the time dependent asymmetry between the decay processes from  $B^0$  and  $\bar{B}^0$ , and which is represented as follows:

$$a_{CP}(t) \equiv \frac{\Gamma_{\bar{B}^0 \rightarrow J/\psi K_S^0}(t) - \Gamma_{B^0 \rightarrow J/\psi K_S^0}(t)}{\Gamma_{\bar{B}^0 \rightarrow J/\psi K_S^0}(t) + \Gamma_{B^0 \rightarrow J/\psi K_S^0}(t)} = \sin(2\phi_1) \sin(\Delta M t), \quad (1.18)$$

where  $\Gamma(t)$  is the time dependent decay fraction, and  $\Delta M$  is the mass difference between  $B_L$  with a lighter mass and  $B_H$  with a heavier mass, which are the  $CP$  eigenstates of  $B^0$  mesons.

Fig. 1.4 shows one of the unitarity triangle corresponding to Fig. 1.1 (f). This triangle is consisted from elements associated with  $B^0$ - $\bar{B}^0$  mixing. An inner angle  $\sin 2\phi_1$  as shown in Fig. 1.4 indicates magnitude of a  $CP$  asymmetry, and if  $\sin 2\phi_1$  is non-zero, it means that the  $CP$  symmetry is violated.  $\phi_1$  is defined as the Eq.(1.19) using the CKM matrix elements.

$$\phi_1 = \arg \left( -\frac{V_{cd}V_{cb}^*}{V_{td}V_{tb}^*} \right). \quad (1.19)$$

Other inner angles  $\phi_2$  and  $\phi_3$  are also defined as follows:

$$\phi_2 = \arg \left( -\frac{V_{tb}V_{td}^*}{V_{ud}V_{ub}^*} \right), \quad (1.20)$$

$$\phi_3 = \arg \left( -\frac{V_{ub}V_{ud}^*}{V_{cd}V_{cb}^*} \right). \quad (1.21)$$

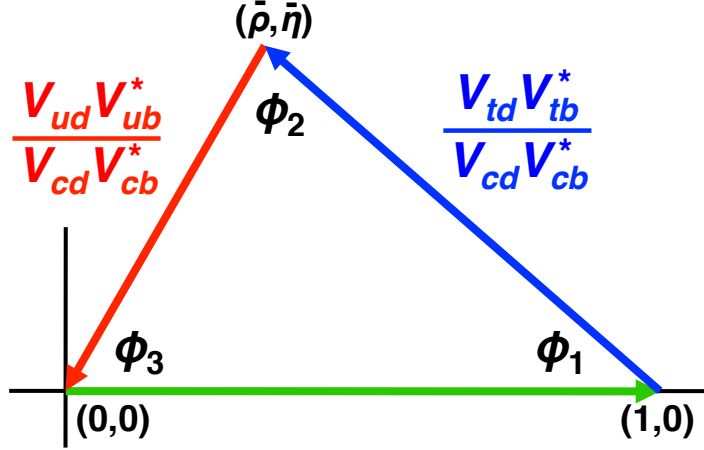


Figure 1.4: The unitarity triangle for  $B^0$ - $\bar{B}^0$  mixing from Eq.(1.17) corresponding to Fig. 1.1 (f). Three side of the triangle is scale by  $1/|V_{cd}V_{cb}^*|$ .

If the K-M model is correct, a large  $CP$  asymmetry can be observed as the time difference  $\Delta t$  between two  $B$  mesons decay time  $t_1$  and  $t_2$  as shown in Fig.1.5. Fig.1.6 shows time dependent decay rates for  $B^0 \rightarrow J/\psi K_S^0$  (dotted blue line) and  $\bar{B}^0 \rightarrow J/\psi K_S^0$  (solid red line), respectively. Here, we assumed that the  $CP$  asymmetry parameter  $\sin 2\phi_1$  to be 0.60. Therefore, the difference between both  $\Delta t$  distributions arises as Fig.1.6. However in the experimental point of view, it is difficult to directly measure the time difference of the decays of two neutral  $B$  mesons, because their lifetimes are too short ( $\tau_{B^0} \sim 1.5$  ps) compared to the time resolution that can be achievable in the currently available technology.

The second difficulty is accumulation of huge numbers of neutral  $B$  meson decays; more than  $10^8$   $B$  meson decay events were necessary to observe  $CP$  violation in  $B^0 \rightarrow J/\psi K_S^0$  decays, since the branching rate of  $B^0 \rightarrow J/\psi K_S^0$  is expected to be  $10^{-4}$ . Luminosities of the  $e^+e^-$  colliders operated at  $\Upsilon(4S)$  state ( $= b\bar{b}$ ) such as DORIS [7] at DESY<sup>1</sup> and CESR [8] at Cornell accelerators are only around  $10^{31}$  /cm<sup>2</sup>s<sup>-1</sup> and they accumulated about  $10^5$   $B$  mesons at most.

In addition, full reconstruction of one of the two parent  $B$  mesons decaying into a flavor-specific state, while the other  $B$  meson decays into the  $CP$  eigenstate, is very important to measure the  $CP$  asymmetry at  $B$ -factory experiments.

In order to observe the  $CP$  violation in the  $B$  meson system and to verify the K-M model, in 1987, P. Oddone proposed a novel concept of an circular  $e^+e^-$  collider with

<sup>1</sup>Deutsches Elektronen-Synchrotron, Hamberg, Germany

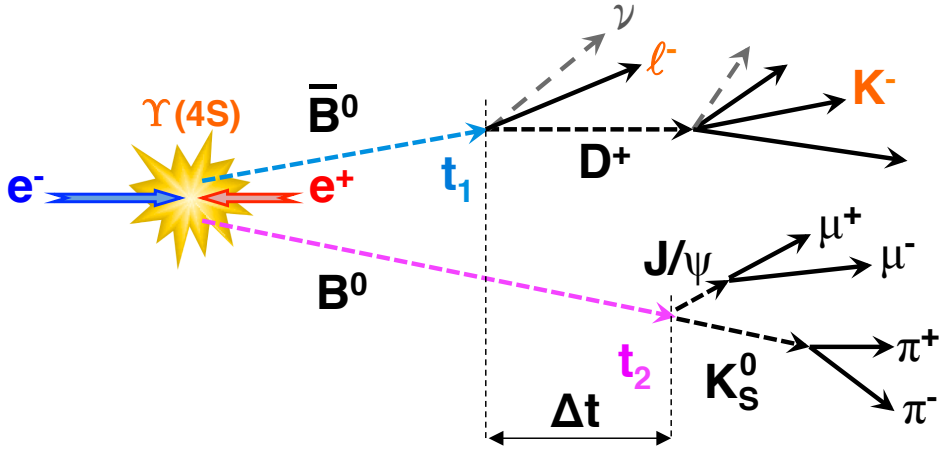


Figure 1.5: The illustration of the time dependent  $B^0$  decay processes with a  $CP$  asymmetry. The flavor of  $B$  decaying  $J/\psi K_S^0$  can be identified by determining the sign of daughter lepton  $\ell$  and  $K$  in the other side of  $B$  decay.

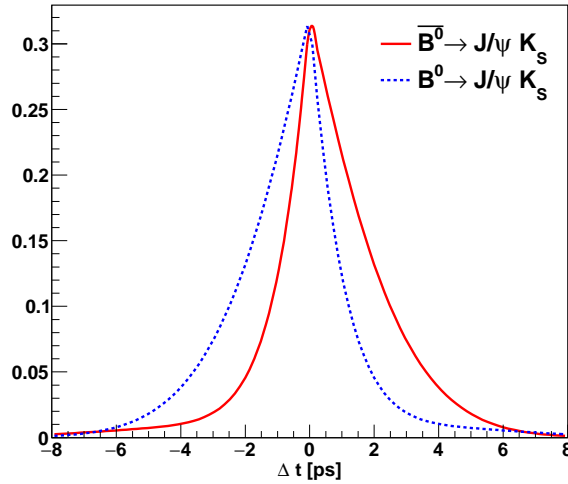


Figure 1.6: The distributions of time dependent decay rate for  $\bar{B}^0 \rightarrow J/\psi K_S^0$  (solid red line) and  $B^0 \rightarrow J/\psi K_S^0$  (dotted blue line). These plots are assumed  $\sin 2\phi_1$  to be 0.60.

asymmetric energy [9]. In the collider total energy in the center-of-mass system is adjusted to be 10.58 GeV, which corresponds to  $\Upsilon(4S)$  mass. A  $B$ - $\bar{B}$  pair from  $\Upsilon(4S)$  are generally generated at rest state because  $\Upsilon(4S)$  is the lowest bound state that can decay into the  $B$  meson pair. Due to the lifetime of  $B^0$  to be about 1.5 ps, the  $B^0$  or  $\bar{B}^0$  generated from  $\Upsilon(4S)$  quickly decays into  $J/\psi K_S^0$  in the center-of-mass system. By assuming the crossing angle between the  $e^+$  and  $e^-$  beams is (approximately) zero, the Lorentz boost factor  $\beta\gamma$  of  $\Upsilon(4S)$  in the laboratory frame corresponding to the detector's rest frame is given by following equation:

$$\beta\gamma = \frac{E_- - E_+}{2\sqrt{E_- E_+}}, \quad (1.22)$$

where  $E_-$  and  $E_+$  are beam energies of  $e^-$  and  $e^+$ , respectively. For example, if an  $E_- = 8.0 \text{ GeV}/c$  electron collides with an  $E_+ = 3.5 \text{ GeV}/c$  positron, the total energy of the center-of-mass system becomes  $10.58 \text{ GeV}$ , thus  $\beta\gamma$  is to be  $0.425$  and produced  $\Upsilon(4S)$  moves with the velocity of  $\beta\gamma c = 0.425c$ . Hence a  $B^0\text{-}\bar{B}^0$  pair decayed from  $\Upsilon(4S)$  also move with the same velocity  $\beta\gamma c$ , then the difference of their decay time of about  $1 \text{ ps}$  corresponds to a few hundreds  $\mu\text{m}$ . This is large enough to be measured with a high precision silicon vertex detector.

In early 1990's, several high luminosity machines with asymmetric energy to produce a huge number of  $B$  mesons, so called  $B$ -factories, were proposed in the world and two of them were realized. One  $B$ -factory experiment is BaBar [10] with the PEP-II accelerator [10] at SLAC<sup>2</sup>, and the other is Belle experiment [11] with the KEKB accelerator [12] at KEK<sup>3</sup>. The KEK  $B$ -factory was designed to achieve a luminosity of  $10^{34} \text{ cm}^{-2}\text{s}^{-1}$  with a finite crossing angle and a crab crossing scheme, while the SLAC  $B$ -factory was designed to achieve  $5 \times 10^{33} \text{ cm}^{-2}\text{s}^{-1}$  with zero crossing angle. The KEK design was rather aggressive compared to the SLAC design. Primary parameters of PEP-II and KEKB accelerators are summarized in Table 1.1.

Table 1.1: Main machine parameters of PEP-II and KEKB during the last stage of their operation [9].

Parameters	PEP-II	KEKB	Units
Beam energy ( $e^-/e^+$ )	9.0/3.1	8.0/3.5	GeV
Lorentz factor $\beta\gamma$	0.56	0.425	
Beam current ( $e^-/e^+$ )	1.8/2.7	1.3/1.8	A
Beam size at IP (x/y/z)	140/3/8.5	80/1/5	$\mu\text{m}/\mu\text{m}/\text{mm}$
Luminosity	$1.2 \times 10^{34}$	$2.1 \times 10^{34}$	$\text{cm}^{-2}\text{s}^{-1}$
Number of beam bunches	1732	1584	
Bunch spacing	1.25	1.84	m
Beam crossing angle	0 (head-on)	$\pm 11$ (crab-crossing)	mrad

In order to measure the time dependent  $CP$  asymmetry shown in Fig. 1.6, we have to reconstruct the flavor-specific  $B$  decay mode. Because a  $B^0\text{-}\bar{B}^0$  pair is produced from a  $\Upsilon(4S)$  decay and is entangled in a coherent quantum state, we can recognize the flavor of a  $B$  meson by identifying the flavor of the other  $B$  meson. For example, if the decay  $B^0 \rightarrow J/\psi K_S^0$  takes place, flavor of the other  $B$  meson should be observed as  $\bar{B}^0$ . A  $\bar{B}^0$  meson is composed of a  $b$ -quark and an anti- $d$  quark, and the  $b$ -quark predominantly decays to  $c$ -quark and subsequently to  $s$ -quark in cascade. If  $b$ -quark decays to  $c$ -quark at a time  $t_1$  through a process such as  $b \rightarrow c\ell^-\nu$  corresponding to  $\bar{B}^0 \rightarrow D^+\ell^-\nu$ , the sign of the lepton charge should be minus ( $\ell^-$ ). An  $s$ -quark produced in the cascade decay tends to appear as  $K^-$  rather than  $K^+$  as the result of hadronization. Thus, if we find an  $\ell^-$  with a large transverse momentum  $p_t$  or a  $K^-$  in the decay products, the flavor of the parent  $B$  meson of them can be determined as  $\bar{B}^0$ . The side of the  $B$  decay cascade used for determining the flavor of the parent  $B$  meson, is name as **tag-side**  $B_{\text{tag}}$ . When the  $B$

<sup>2</sup>National Accelerator Laboratory, Stanford, USA

<sup>3</sup>High Energy Accelerator Research Organization (KEK), Tsukuba, Japan

meson in the tag-side was determined as  $\bar{B}^0$ , the flavor of the parent  $B$  meson that decays into  $J/\psi K_S^0$  at  $t_2$ , can be subsequently determined as  $B^0$  (not  $\bar{B}^0$ ) in a high probability. The method above mentioned is called **flavor tagging**. The  $B$  meson decaying into a  $CP$  eigenstate is named as **CP-side**  $B_{CP}$ .

The time difference  $\Delta t$  is defined as the distance of two decay vertex  $\Delta z$  between  $B_{\text{tag}}$  and  $B_{CP}$  provided by a vertex detector, and can be obtained by following equation:

$$\Delta t \equiv \frac{\Delta z}{\beta\gamma c}. \quad (1.23)$$

In Fig. 1.6 the  $\Delta t$  distribution, for  $B_{CP} = \bar{B}^0(B^0)$  is shown as the red solid (blue dashed) line.

For such flavor tagging a high efficiency kaon identification in the tag-side is essential. In order to perform the flavor tagging, the Belle detector at the KEK  $B$ -factory adopted a threshold type Cherenkov counters [13], and the Babar detector at the SLAC  $B$ -factory adopted a total internal reflection type ring imaging Cherenkov counter [14].

Belle experiment and BaBar experiment started almost at the same time in 1999, and announced the first result of measurement of the  $CP$  asymmetry in the  $B$  meson system in 2001. The results of BaBar [15] and Belle [16] were as follows:

$$\sin 2\beta(\text{BaBar}) = 0.59 \pm 0.14(\text{stat}) \pm 0.05(\text{syst}), \quad (1.24)$$

$$\sin 2\phi_1(\text{Belle}) = 0.99 \pm 0.14(\text{stat}) \pm 0.06(\text{syst}), \quad (1.25)$$

where the parameter  $\beta$  corresponds to  $\phi_1$ <sup>4</sup>. The deviation from the  $CP$  conserved expectation are confirmed with  $4.1\sigma$  and  $6\sigma$  by BaBar and Belle, respectively. Both results clearly established the existence of the  $CP$  violation in the  $B$  meson system, and the K-M model is proven to be valid for the explanation of  $CP$  violation in quark sector. Finally Kobayashi and Maskawa received the 2008 Nobel Prize in Physics.

Both  $B$ -factories also measured other angles of the unitarity triangle, namely  $\phi_2$  and  $\phi_3$ . Both experiments had succeeded in improving precision of the unitarity triangle parameters by increasing the amount of data. BaBar experiment finished in 2008 and Belle experiment finished in 2010. Fig. 1.7 [17] shows constraints on parameters of the unitarity triangle obtained as combination of various measurements.

### 1.1.5 Search for physics beyond the standard model

In the summer 2012, LHC experiments ATLAS and CMS at CERN<sup>5</sup> announced a discovery of Higgs boson at  $126 \text{ GeV}/c^2$ . The discovery of the last long-awaited missing particle of the standard model (SM) established reliability of the SM. The SM can explain all phenomena below  $100 \text{ GeV}$  with high precision, hence is regarded as the most successful theory ever established.

Here, I briefly summarize contents within the SM framework as follows:

<sup>4</sup>The different naming notation for the three phases in the CKM matrix is used by BaBar and Belle.  $\phi_1$ ,  $\phi_2$ , and  $\phi_3$ , which are used by Belle, are corresponding to  $\beta$ ,  $\alpha$ , and  $\gamma$  by BaBar, respectively.

<sup>5</sup>The European Organization for Nuclear Research (CERN), Geneva, Switzerland

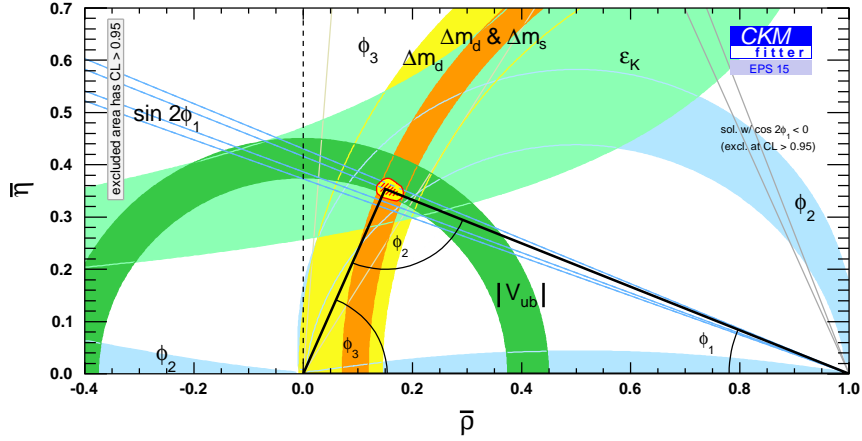


Figure 1.7: The measured unitarity triangle in  $(\bar{\rho}, \bar{\eta})$  plane provided by the CKM fitter group in 2015 [17]. The red hashed region indicates the vertex of the angle  $\phi_1$  by the global fit and corresponds to 68 % CL.

- Fermion consist of quarks and leptons:

$$\text{quark} : \begin{pmatrix} u & c & t \\ d & s & b \end{pmatrix},$$

$$\text{lepton} : \begin{pmatrix} e^- & \mu^- & \tau^- \\ \nu_e & \nu_\mu & \nu_\tau \end{pmatrix}.$$

- Gauge bosons that mediates electromagnetic, weak, and strong interactions based on the gauge theory of  $SU(3)_C \times SU(2)_L \times U(1)_Y$ .
- The KM mechanism that occurs the CP violation in the quark sector.
- A scalar Higgs boson that provides the proper mass for every particle.

However, we have some observational results that can not be explained within the SM framework:

- We have to explain why the  $CP$  violation is caused by the KM mechanism.
- We need a mechanism which can determine the mass value of the SM particle.
- We have discovered neutrinos have the finite masses through the neutrino oscillations, although their masses are zero within the SM framework.
- We have to introduce a mechanism that is exactly canceling the loop correction of the Higgs mass. That is known as the Naturalness problem.
- We have to describe the origin of the dark matter in the universe, but there is no adequate candidate in the SM particles.
- Gravity interaction, in particular, quantum gravity is not included in the SM.

These problems suggest the existence of new physics beyond the standard model (BSM), and the SM is expected to be the effective theory at low energy. In order to search BSM, we can consider two approaches using the collider experiments. One is the direct search using a high center mass energy collider, which has potential of generating new physics particles in the TeV scale. That approach is called the high-energy experiments. ATLAS and CMS are typical examples of the high-energy experiments.

Other approach is using a high-intensity (or high-luminosity) collider. We can measure effects of new physics through loop diagrams existing in decay channels of heavy mesons such as  $B$ ,  $D$ , and heavy charged lepton  $\tau$ . Because the contribution would appear in decay channels highly suppressed by the SM, this approach requires a highly precise measurement and a high statistics. A next generation  $B$ -factory experiment has to have roles as the high-intensity experiment.

Both approaches are independently and complementary to each other in the aim of the new physics search. When new particles observed at the high-energy experiments, the high-intensity experiment would measure their flavor structure precisely. Even if any new particles are not found at a few TeV scale, the high-intensity experiments can provide constrains for NP models by precision measurements of rare decays.

### 1.1.6 Possibility of new physics models

Now, several possible scenarios of BSM are proposed [9]. Here, I will describe about Supersymmetry (SUSY) as the most popular scenario of new physics.

SUSY describes a symmetry between fermions and bosons. By exchanging fermions and bosons by SUSY, new elementary particles would be introduced as partners of the SM particles, and they are called super-partners. In particular, the Minimal Supersymmetric Standard Model (MSSM), which is one of the standard model of SUSY, would introduce super-partners for all the SM particles and extra charged Higgs bosons. Super-partners of the gauge bosons in the SM are described as fermions with 1/2 spin. While super-partners of the SM quarks  $q$  and leptons  $\ell$  are introduced with spin 0, which are called the Squarks  $\tilde{q}$  and the Sleptons  $\tilde{\ell}$ . The neutral super-partner of the SM neutral gauge boson, which is called the Neutralino  $\tilde{\chi}^0$ , is one of the most plausible candidate of dark matter. The MSSM also introduces three neutral and two charged Higgs bosons ( $h, H^0, A^0, H^\pm$ ) and their super-partners ( $\tilde{H}_1^0, \tilde{H}_2^0, \tilde{H}^\pm$ ), which are called the Higgsino. Higgs mass must diverge by the radiative loop correction of itself, heavier fermion such as  $t$ -quark, and massive bosons. By introducing the Higgsino and super-partners, the divergence of the Higgs mass can be canceled through the higher order contribution from the introduced SUSY particles.

The Two Higgs Doublet Model (2HDM) is the simplest extension for the Higgs sector. In particular, the type-II 2HDM introduces two Higgs doublets, and the doublets would couple to down-type or up-type quarks in the SM, respectively. Because the tauonic decay shown in Fig. 1.8 also allows a contribution of a charged Higgs introduced type-II 2HDM as well as a charged gauge boson in the SM, that decay rate would be enhanced compared with the SM expectation.

Other possible scenarios of new physics are listed as follows:

- Minimal Flavor Violation (MFV), Extensions of MFV, and MFV SUSY

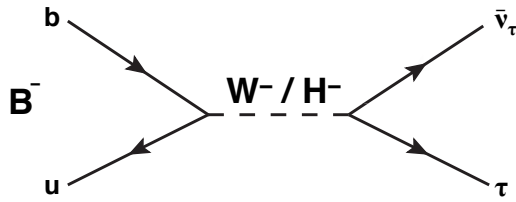


Figure 1.8: The tauonic decay diagram with the Charged Higgs  $H^\pm$  expected from the 2HDM through a tree level contribution.

- nonMFV SUSY
- SUSY alignment models
- Forth generation
- Randall-Sundrum models
- Light Higgs models

### 1.1.7 New physics search in the super KEK $B$ -factory

However, we can not judge which scenario is correct without experimental verification, because they need theoretical assumptions and a lot of input parameters. In order to choose the new physics model, we should verify whether the CKM parameters are deviated from expected values in the SM. The precise measurement of rare decays from  $B$  meson and other heavy particles is important because those decay processes are sensitive to new physics contribution. These decays are prohibited at the tree level in the SM, and a new physics contribution may be comparable to higher order loops in the SM.

In order to measure such rare  $B$  decays, a construction of more high luminosity  $B$ -factory, so called super KEK  $B$ -factory (S-KEKB) at KEK was proposed and started construction in 2011. S-KEKB is designed to have a luminosity more than 40 times of the previous KEK  $B$ -factory by reducing the beam sizes of both electron and positron at the interaction point and also increasing currents of the beams. The experiment using the Belle II detector at S-KEKB is named Belle II. The first commissioning of S-KEKB is scheduled in 2016 JFY and the Belle II detector used for S-KEKB will be installed in 2018.

Here, a few examples of interesting measurements in S-KEKB are described in the following sections.

#### $b \rightarrow s\bar{s}s$ decays

The value of  $\sin 2\phi_1$  as measured in  $B^0 \rightarrow \phi K_S$  and similar  $b \rightarrow s$  transitions differs slightly from the value measured in  $B \rightarrow J/\psi K_S$  decays, the current world average difference being  $\Delta S \equiv \sin 2\phi_1^{\phi K_S} - \sin 2\phi_1^{J/\psi K^0} = 0.22 \pm 0.17$  [18]. The former decays proceed through  $b \rightarrow s\bar{s}s$  underlying quark process, possible only through the loop processes shown in Fig. 1.9 (left), and the latter through the  $b \rightarrow cs\bar{c}$  tree diagram. While the CKM matrix

elements included in the amplitudes of these decays are approximately real, the possibility of  $B^0$ - $\bar{B}^0$  mixing before the decay introduces an additional factor  $(V_{td}^* V_{td})^2 \propto e^{-2i\phi_1}$ . Hence, the decay time distribution of both decays is sensitive to  $\sin 2\phi_1$ , and the difference in the value measured in the two decays is expected to vanish within small corrections,  $\Delta S = 0.03 \pm_{0.04}^{0.01}$  [19]. However, NP particles can contribute in the loop of  $B^0 \rightarrow \phi K_S$ , as illustrated in Fig. 1.9 (right), and change the expectation for  $\Delta S$ .

In  $B \rightarrow K^+ K^- K_S$  decays,  $\phi K_S$  is one of several intermediate resonant contributions to the final state. In order to determine the value of  $\sin 2\phi_1^{\phi K_S}$ , one has to perform a decay time dependent Dalitz plot analysis, where the accuracy of  $K^+ K^- K_S$  vertex determination and the particle identification for the suppression of backgrounds are crucial. These are achieved in Belle II with the vertex detector and the particle identification system. The expected dependence on integrated luminosity of the  $\Delta S$  sensitivity from these and related decays is shown in Fig. 1.10 [20]. With  $\mathcal{L} = 10 \text{ ab}^{-1}$  of data, the experimental and theoretical uncertainties will be comparable.

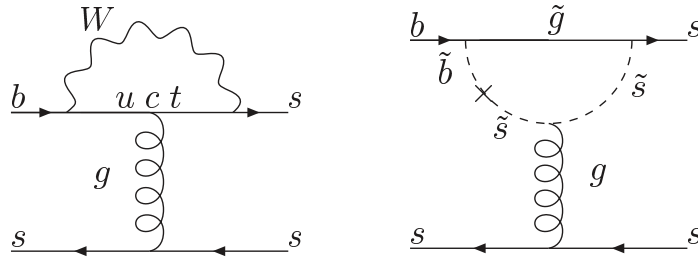


Figure 1.9: The SM contribution (left) and the gluino-down squark contribution (right) to the  $b \rightarrow s \bar{s} s$  transition.

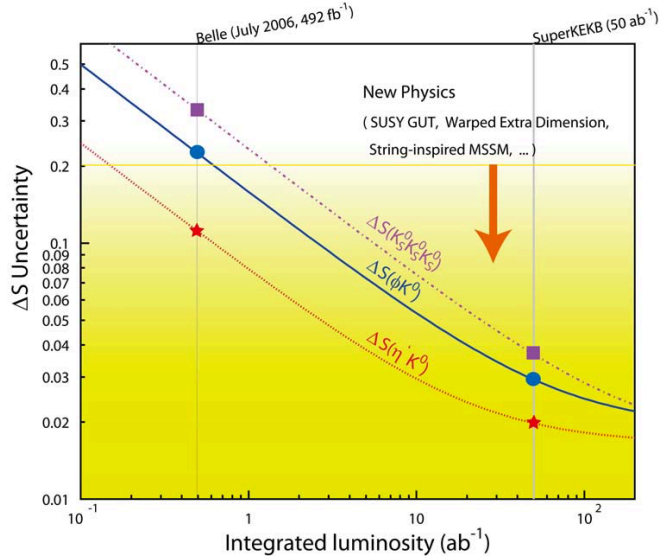


Figure 1.10: Expected precision of  $\Delta S$  measurements as a function of integrated luminosity [20].

## $b \rightarrow s\gamma$ decays

Radiative decays  $b \rightarrow s\gamma$  are sensitive probes of right-handed weak currents, which are absent by fiat in the SM. The helicity structure of the effective Hamiltonian that describes this loop process allows only for  $b_R \rightarrow s_L\gamma_L$  and  $b_L \rightarrow s_R\gamma_R$  decays, where the subscript denotes the handedness of the particle. The amplitude of the former (latter) process depends on the helicity flip and is proportional to  $m_b$  ( $m_s$ ). In mesons the  $b_L \rightarrow s_R\gamma_R$  transition, for example, can proceed directly or via  $\bar{B}^0 \rightarrow B^0$  mixing; the interference leads to a small time dependent  $CP$  asymmetry that is proportional to  $m_s/m_b$ . In various NP models (e.g. Left-right symmetric models) the right-handed currents are not suppressed and can lead to a sizable  $CP$  asymmetry. A prominent example of such radiative quark transitions is the decay  $B^0 \rightarrow K_S\pi^0\gamma$ . Within the SM, the decay time dependent  $CP$  asymmetry in this decay is estimated to be  $S \approx -2(m_s/m_b)\sin 2\phi_1 \approx -0.04$ ; some SM predictions allow for a value of  $|S|$  up to 0.1 [21, 22]. On the other hand, in L-R symmetric models, the asymmetry can be as large as  $S \approx 0.67\cos 2\phi_1 \approx 0.5$ .

The decay-time dependence in  $B^0 \rightarrow K_S\pi^0\gamma$  is measured through reconstruction of the  $B$  meson decay vertex using only pions from  $K_S \rightarrow \pi^+\pi^-$  decay that are constrained to the  $e^+e^-$  interaction region profile. The Belle II vertex detector will improve the vertex position resolution and, more importantly, increase the reconstruction efficiency of  $K_S$  decays with charged pion hits in the silicon detectors. The expected accuracy of the  $S(K_S\pi^0\gamma)$  measurements is shown in Fig. 1.11 [20]. With a data set corresponding to  $50\text{ab}^{-1}$ , the sensitivity of the measurement will reach the SM value and thus cover a range of NP predictions.

The measurement of the  $S(K_S\pi^0\gamma)$  also nicely illustrates the complementarity among the precision frontier experiments, specifically between Belle II and LHCb. The sensitivity of Belle II for the  $S(K_S\pi^0\gamma)$  measurement can not be reached by the LHC experiment. On the other hand (neglecting the possibility of dedicated longer data taking periods at the  $\Upsilon(5S)$  resonance), the LHCb experiment can perform a much more precise measurement of the  $B_s \rightarrow \mu^+\mu^-$  decay rate. When interpreting both measurements within the Minimal Supersymmetric Standard Model in the mass insertion approximation (MIA), the contours of the MIA parameter and  $\tan\beta$  are shown in Fig. 1.12 [20]. While the measurement of the  $\mathcal{B}(B_s \rightarrow \mu^+\mu^-)$  at the level of  $10^{-9}$  yields a rather loose constraint on the MIA parameter, a combination with the measurement of the  $S(K_S\pi^0\gamma)$  with a precision of 0.1 results in a tight constraint in both dimensions.

## $B \rightarrow \tau\nu$

One of the outstanding problems in particle physics is the question of the origin of masses and the related Higgs boson(s). The SM incorporates a single neutral Higgs boson. The Higgs sector of various extensions of the SM is richer, with charged Higgs bosons possible as well. In the Type II Two Higgs Doublet Models (2HDM-II), the charged Higgs boson  $H^\pm$  behaves like the charged weak bosons  $W^\pm$  apart from its couplings to fermions, which are proportional to their masses. The contribution of  $H^\pm$  can thus be expected in all charged weak current processes, especially those involving heavy fermions. A typical example is the purely leptonic decay of charged B mesons,  $B^+ \rightarrow \tau^+\nu_\tau$  where, in the 2HDM-II models, the contribution of  $H^+$  is expected to be largest due to the masses of

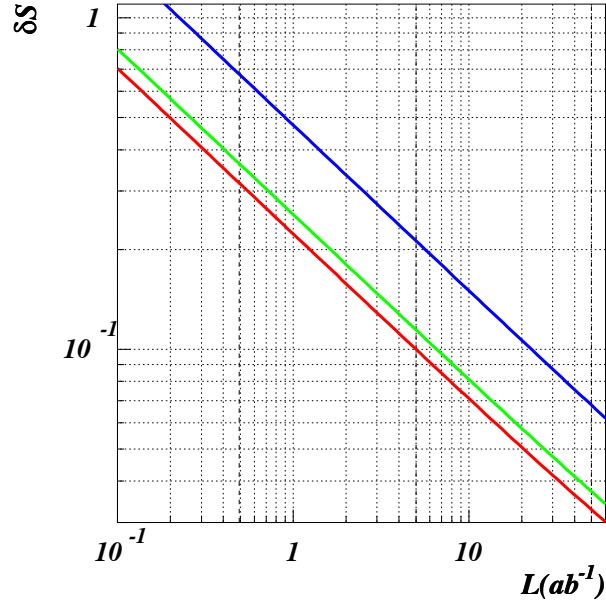


Figure 1.11: Expected precision of the  $TCPV$  asymmetry measurements for  $B \rightarrow K^{*0}(982)\gamma$  (green), other  $K_S\pi^0\gamma$  (blue) and all  $K_S\pi^0\gamma$  final state (red) as a function of integrated luminosity [20].

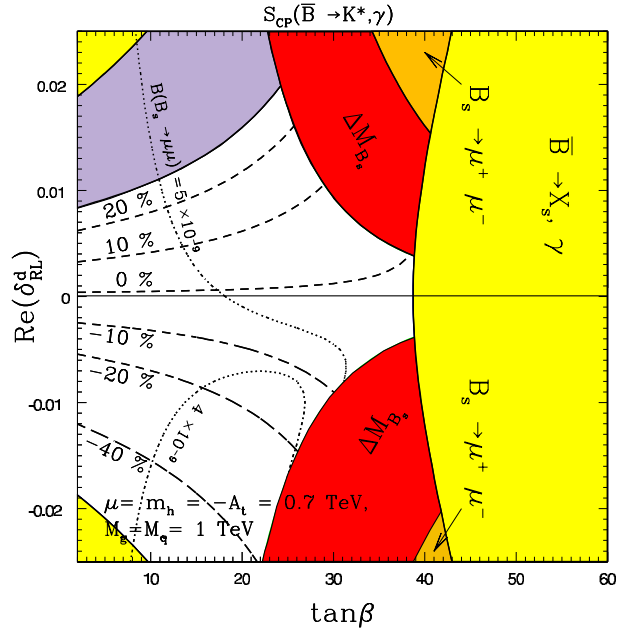


Figure 1.12: Constraints on the MIA parameter  $Re(\delta_{RL}^d)$  and  $\tan\beta$  from the measurement of the  $S(K_S\pi^0\gamma)$  and  $\mathcal{B}(B_s \rightarrow \mu^+\mu^-)$  [20]. Contours of  $S(K_S\pi^0\gamma)$  are shown in the intervals of 0.1.

the  $\tau$  lepton and the  $b$ -quark.

The effect of a possible charged Higgs boson on the partial leptonic decay width of  $B$  mesons is given by

$$\Gamma(B^+ \rightarrow \tau^+ \nu_\tau) = \Gamma^{\text{SM}}(B^+ \rightarrow \tau^+ \nu_\tau) [1 - (m_B^2/m_H^2) \tan^2 \beta]^2, \quad (1.26)$$

where  $\Gamma^{\text{SM}}(B^+ \rightarrow \tau^+ \nu_\tau)$  denotes the SM partial decay width, and  $\tan \beta$  denotes the ratio of the vacuum expectation values of the two Higgs fields and is a free parameter of the models. The leptonic decay width can thus be suppressed or — if the  $H^\pm$  contribution is dominant — enhanced compared to the SM value.

Experimentally, of the leptonic branching fraction measurement [23] consists of (partial) reconstruction of the accompanying  $B$  meson in the event, called the tagging  $B$  meson ( $B_{\text{tag}}$ ).  $B_{\text{tag}}$  can be fully reconstructed in a number of hadronic decays (hadronic tagging) or partially reconstructed in semileptonic decays (semileptonic tagging), where the hadronic system (and the charged lepton) of the final state is detected while the neutrino escapes the detection. The hadronic tagging method has better purity in the  $B_{\text{tag}}$  sample, but suffers from a lower efficiency compared to semileptonic tagging. The remaining particles in the event are assigned to the signal  $B$  meson ( $B_{\text{sig}}$ ); if they are consistent with a possible  $\tau$  decay, the undetected part of the event consists of one or more neutrinos from (semi)leptonic decays. The signature of such event is thus a little or no residual energy detected in the electromagnetic calorimeter, after removing the contributions from the particles used in the reconstruction of  $B_{\text{tag}}$  and the  $\tau$  from  $B_{\text{sig}} \rightarrow \tau \nu_\tau$ . The resulting distribution of the residual calorimeter energy for the measurement based on the semileptonic tagging [24] is shown in Fig. 1.13 (left). The peaking component at low energy is the signal of  $B \rightarrow \tau \nu_\tau$ . The leptonic branching fraction is found to be  $\mathcal{B}(B \rightarrow \tau \nu_\tau) = (1.65 \pm_{0.37}^{0.38} \pm_{0.37}^{0.35}) \times 10^{-4}$ .

Excellent performance of the electromagnetic calorimeter is crucial for the described measurement. The Belle II calorimeter maintains this performance even with the more severe backgrounds expected at S-KEKB.

The statistical and systematic uncertainty of the result are almost equal in magnitude. However, the main sources of the systematic error — statistics of the control samples for the shape of the residual energy distribution and efficiency of the tagging — will decrease with the increased integrated luminosity of the available data sample. Assuming the theoretical uncertainties on the CKM element  $|V_{ub}|$  and  $B$  meson decay constant  $f_B$  will be reduced to 5% in a few years, we obtain the five standard deviations discovery sensitivity region at  $\mathcal{L} = 5 \text{ ab}^{-1}$  in the  $(\tan \beta, m_H)$  plane shown in Fig. 1.13 (right).

### $B \rightarrow K\pi$

Charmless 2-body  $B$  meson decays are another example of rare SM processes in which the possible contribution of NP could be large enough to be observed in the future. The decays  $B \rightarrow K\pi$  proceed through a tree diagram depicted in Fig. 1.14 but are suppressed by the small CKM matrix element  $|V_{ub}|$ . Thus, the contribution of the loop penguin diagram is of similar magnitude. The interference of the two leads to a direct  $CP$  asymmetry of  $A_{CP}^f = [\Gamma(\bar{B} \rightarrow \bar{f}) - \Gamma(B \rightarrow f)]/[\Gamma(\bar{B} \rightarrow \bar{f}) + \Gamma(B \rightarrow f)]$ . As suggested in diagrams of Fig. 1.14, the main processes underlying the  $B \rightarrow K\pi$  decays are the same and equal for

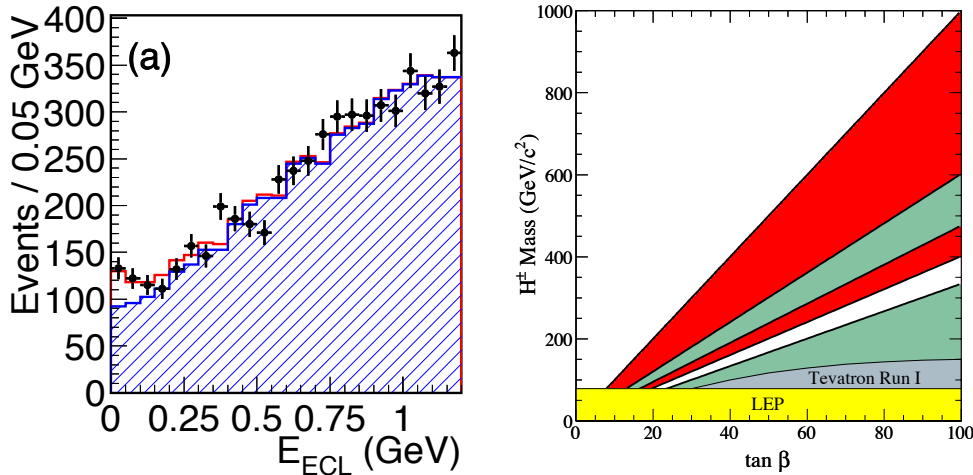


Figure 1.13: Left: Distribution of residual energy in the calorimeter for semileptonic tagged  $B \rightarrow \tau\nu_\tau$  candidate events [24]. The dashed histogram represents the background, and the solid red histogram the result of the fit that includes a signal component peaking at null value. Right:  $5\sigma$  discovery sensitivity region for the charged Higgs boson from  $B \rightarrow \tau\nu_\tau$  branching fraction measurement at an integrated luminosity of  $5 \text{ ab}^{-1}$  (red). Other colored regions denote the presently excluded current exclusion regions.

neutral and charged  $B$  mesons. Neglecting additional diagrams contributing to  $B^+$  decays only (and expected to be much smaller than the shown contributions), the asymmetries  $A_{CP}^{K^+\pi^0}$  in  $B^\pm \rightarrow K^\pm\pi^0$  decays and  $A_{CP}^{K^+\pi^-}$  in  $B^0(\bar{B}^0) \rightarrow K^\pm\pi^m p$  decays are expected to be the same. However, a precise  $CP$  measurement by Belle [25] showed a significant difference between the two,  $\Delta A = A^{K^+\pi^0} - A^{K^+\pi^-} = 0.164 \pm 0.035 \pm 0.013$ . The asymmetry in the number of reconstructed signal decays can be observed visually in Fig. 1.15. The difference could be due to the neglected diagrams contributing to charged  $B$  meson decays, for which the theoretical uncertainty is still rather large, or to some unknown NP effect that violates isospin. In Ref. [26] the author proposes a test of sum rule for NP free of theoretical uncertainties. The sum rule reads

$$\begin{aligned}
 A_{CP}^{K^+\pi^-} &+ A_{CP}^{K^0\pi^+} \frac{\mathcal{B}(B^+ \rightarrow K^0\pi^+) \tau_{B^0}}{\mathcal{B}(B^0 \rightarrow K^+\pi^-) \tau_{B^+}} \\
 &= A_{CP}^{K^+\pi^0} \frac{2\mathcal{B}(B^+ \rightarrow K^+\pi^0) \tau_{B^0}}{\mathcal{B}(B^0 \rightarrow K^+\pi^-) \tau_{B^+}} + A_{CP}^{K^0\pi^0} \frac{2\mathcal{B}(B^0 \rightarrow K^0\pi^0)}{\mathcal{B}(B^0 \rightarrow K^+\pi^-)}, \quad (1.27)
 \end{aligned}$$

where  $\mathcal{B}(B \rightarrow f)$  denotes the corresponding branching fraction and  $\tau_{B^0(B^+)}$  lifetimes of neutral and charged  $B$  mesons.

By measuring all the observables in the above equation, one can test the prediction of the SM. Using the current world average values for the corresponding quantities [18], the isospin sum rule can be presented as a diagonal band in the plane of  $A_{CP}^{K^0\pi^0}$  vs.  $A_{CP}^{K^+\pi^+}$  (see Fig. 1.16 (left)). The slope of this dependence is determined by the precisely known branching fractions and lifetimes, and the uncertainty of the offset is mainly due to  $A_{CP}^{K^+\pi^0}$  and to a much lesser extent to  $A_{CP}^{K^+\pi^-}$ .

Several measurements must be accomplished in order to perform the above test. The

most demanding is the measurement of the all-neutral final state  $K^0\pi^0$ . In the decay-time dependent measurement, the vertex reconstruction is based on charged pions from the neutral kaon decays (as in  $B^0 \rightarrow K_S\pi^0\gamma$ ) and depends crucially on a vertex detector with a large radial acceptance. Reconstruction of the neutral pion ( $\pi^0 \rightarrow \gamma\gamma$ ) requires very good electromagnetic calorimetry. For the final states with charged kaons and pions, an excellent separation between the two particle species must be provided by the particle identification system. The main systematic uncertainty contributions (tag side interference) in the recent measurement of  $B^0 \rightarrow K^0\pi^0$  [27] are expected to be reduced as the data sample increases. The expected sensitivity of the sum rule test with the integrated luminosity of  $50 \text{ ab}^{-1}$  is illustrated in Fig. 1.16 (left). We have conservatively scaled only statistical uncertainties on  $CP$  asymmetries of  $K^0\pi^+$  and  $K^+\pi^0$  final states. If one assumes the current central values of observables and the expected accuracy a discrepancy in the expectation of Eq. 1.2 [26] can be clearly established.

## 1.2 Importance of particle identification device in the super KEK $B$ -factory

As the discussion in the previous section, high efficiency flavor tagging of  $B$  mesons is of importance at S-KEKB. In addition, they have to perform reconstruction of decay processes, which is used for measurements of the CKM matrix elements, time dependent  $CP$  asymmetry, and the  $CP$  asymmetries through  $B$  or  $D$  mixing, and so on. In particular, precise measurements of rare  $B$  decays such as  $b \rightarrow s(\text{or } d)\gamma$  or  $B \rightarrow \tau\nu$  are very important to explore and discover the new physics BSM.

Devices identify charged pions and kaons, which is so called PID devices, will play key role for the flavor tagging and the reconstruction of the  $B$  decays. The PID devices of Belle II should identify pions and kaons at the lower momentum region ( $\lesssim 1.5 \text{ GeV}/c$ ) for flavor tagging and/or the higher region ( $1.5\text{--}3.8 \text{ GeV}/c$ ) for the reconstruction of rare  $B$  decays.

In the Belle experiment, the  $\pi/K$  separation with  $3\sigma$  had been achieved by the combination of the threshold type Aerogel Cherenkov counters (ACCs) [13] for momentum range of  $0.5\text{--}3.5 \text{ GeV}/c$ , the Time-of-Flight (TOF) [28] counters for tracks up to  $1.2 \text{ GeV}/c$ , and measurements of energy-loss  $dE/dx$  in the Central Drift Chamber (CDC) [11] for tracks up to  $0.8 \text{ GeV}/c$ . The location of these counters in the Belle detector is shown in Fig. 1.17. Low momentum tracks, which can not reach ACCs and TOF counters due to curling under a high magnetic field, are identified using only the CDC information.  $\pi/K$  identifications of the Belle II detector are necessary to improve the particle separation efficiencies at the momentum range required by the physics of Belle II.

However, in Belle II, it is difficult to improve the PID efficiency by using the same methods such as the ACC or the TOF. The time-of-flight of pions and kaons are  $4.005 \text{ ns}$  and  $4.033 \text{ ns}$ , respectively, at  $p = 4 \text{ GeV}/c$  for a flight path length of  $L = 1.2 \text{ m}$  which is corresponding to the perpendicular between the interaction point of  $e^+e^-$  and the plastic scintillator of the TOF. Therefore the time difference between pions and kaons is only  $28 \text{ ps}$ . With the time resolution of  $100 \text{ ps}$ , which is the designed value for Belle TOF system, pions and kaons can not be separated. Therefore, the TOF system can not be

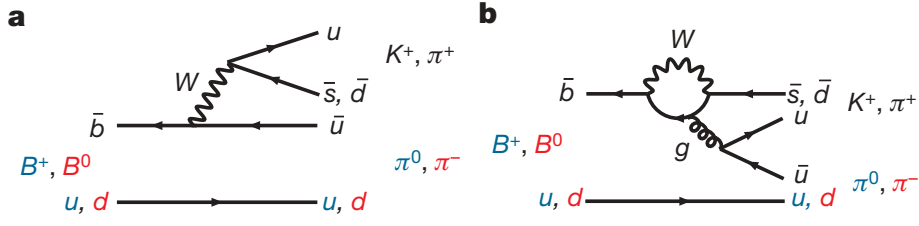


Figure 1.14: Tree and penguin diagrams contributing to  $B \rightarrow K\pi$  decays [25].

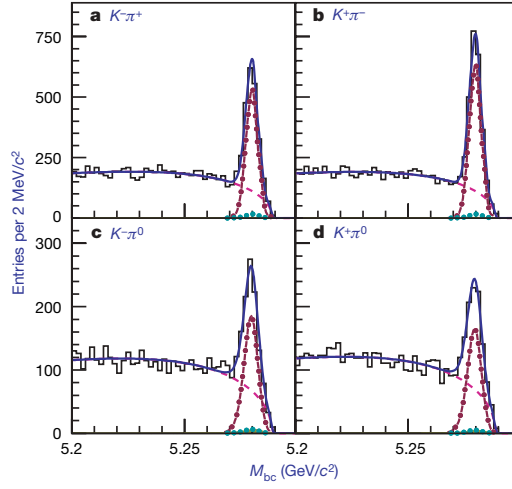


Figure 1.15: The reconstructed signal of  $\bar{B}^0 \rightarrow K^- \pi^+$  (top left),  $B^0 \rightarrow K^+ \pi^-$  (top right),  $B^- \rightarrow K^- \pi^0$  (bottom left),  $B^+ \rightarrow K^+ \pi^0$  (bottom right) [25].

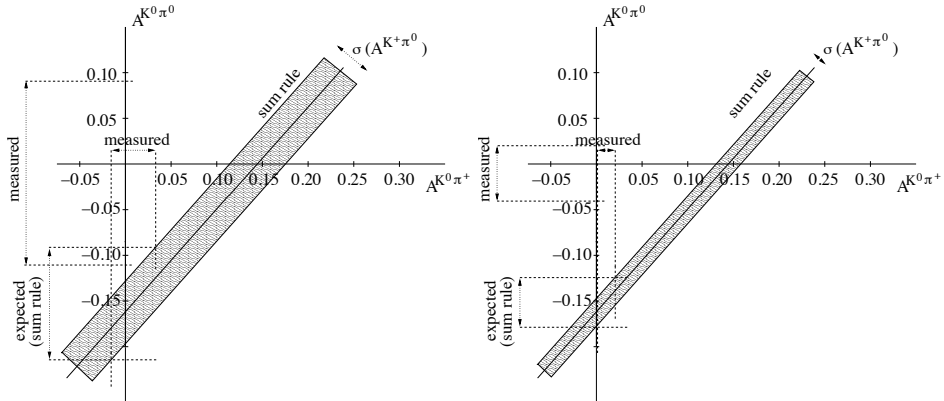


Figure 1.16: Left: Sum rule from Eq. 1.2 [26] shown as  $A_{CP}^{K^0\pi^0}$  dependence on  $A_{CP}^{K^+\pi^+}$ . The experimental values of various observables are taken from Ref. [18] and the hatched region represents the expectation from the sum rule. Right: The same sum rule with the current central values of observables and the accuracies expected with  $\mathcal{L} = 50 \text{ ab}^{-1}$ .

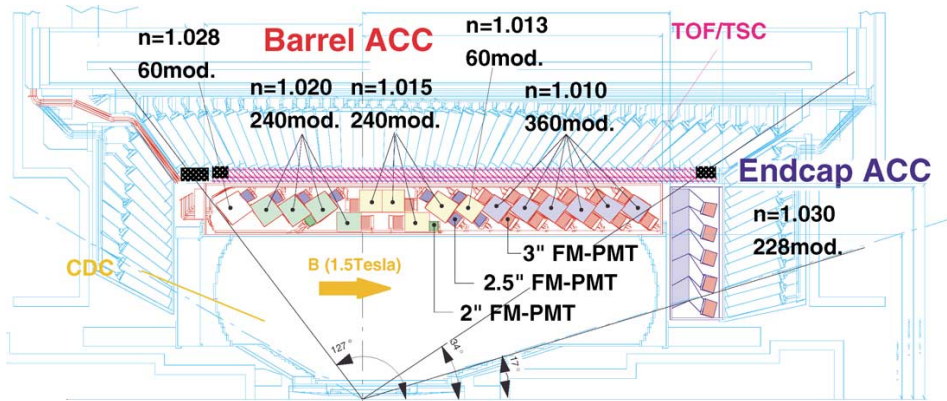


Figure 1.17: The partial cross-sectional view of the Belle detector. This schematic shows the location of Central Drift Chamber, Aerogel Cherenkov counter modules, and the Time-of-Flight counters which were used for a particle identification.

used as a PID device at the high momentum region.

The ACC is also to be used difficult for Belle II. The PID performance of the ACC is determined by the number of detected photoelectrons  $N_{pe}$  produced in aerogel radiators, and  $N_{pe}$  can be increased by using the radiator with a high refractive index  $n$  ( $N_{pe} \sim (1 - (n\beta)^{-2})$ ), however the momentum range, where we can separate pions and kaons, drops in inverse proportion to the refractive index. Since the entire structure of the Belle II detector reuses the Belle detector and then space for the PID device can not be enlarged. Neither the TOF counters nor the ACC modules can be placed in the forward end-cap region that covers the polar angle range of  $13.6^\circ < \theta < 33.4^\circ$ . Fig. 1.18 shows the momentum distribution of final state pions as a function of polar angle in a  $B \rightarrow \pi\pi$  signal Monte-Carlo sample. This decay mode is used for the measurement of the angle  $\phi_2$  of the unitarity triangle. Because this decay process is a two-body decay, the produce tracks tend to have higher momentum. In particular, in the forward end-cap region ( $13.6^\circ < \theta < 33.4^\circ$ ) we can find that they are expected to have the momentum up to  $3.5 \text{ GeV}/c$ . Thus the PID for the wide-range of momenta up to  $3.5 \text{ GeV}/c$  has to be established by using the information from only one detector.

The BaBar detector at the SLAC  $B$ -factory employed the Detector of Internally Reflected Cherenkov light (DIRC) counter [14] for the  $\pi/K$  identification. The particle identification method of this counter is different from the ACC of Belle but a kind of Ring imaging Cherenkov (RICH) counter. Because the RICH method uses information of a Cherenkov emission angle provided by a charged track and the number of detected Cherenkov photons, a Cherenkov detector using the RICH method can provide more efficient particle identification compared with the threshold type Cherenkov counter. The DIRC counter of the BaBar detector achieved better performance (84% kaon efficiency with 1.1% pion mis-identification probability [9]) than the ACC at the Belle detector.

In Belle II,  $\pi/K$  identification devices are replaced with novel type Cherenkov counters using the ring-imaging scheme. A Time of Propagation (TOP) counter for the barrel region and an Aerogel Ring Imaging Cherenkov (ARICH) counter for the end-cap region

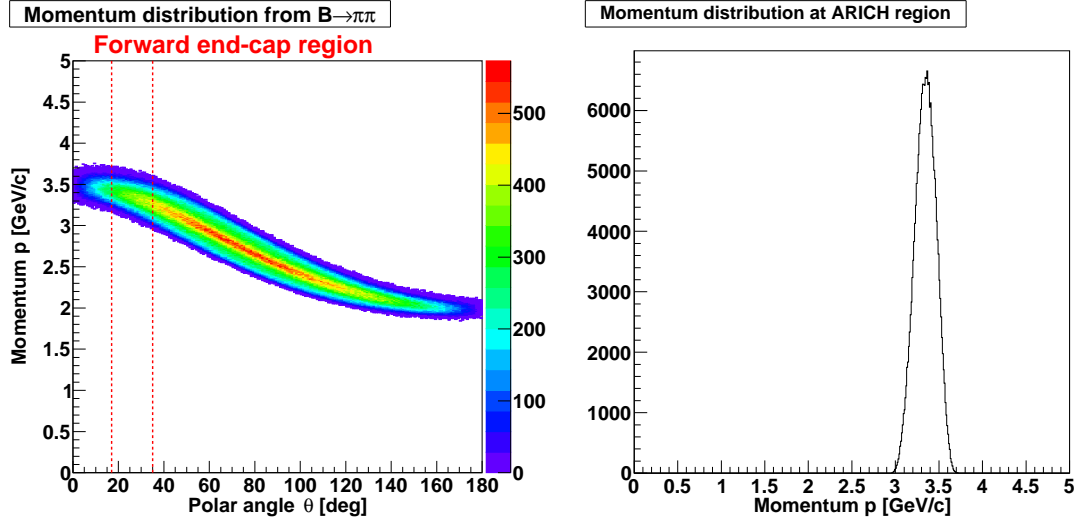


Figure 1.18: Momentum of final state pions from  $B \rightarrow \pi\pi$  decays as a function of polar angle. (Left) Two-dimensional plots of momentum for all polar angle region. The range separated by vertical dashed (red) lines indicates the forward end-cap coverage. (Right) The momentum distribution of pions entering only within the forward end-cap coverage.

are adopted.

The replacement with the new PID devices, especially the ARICH counter, requires spacial conditions as follows:

- Whole structure to be compact.

Only 280 mm is available at the end-cap region along the direction of the beam pipe. Whole structure of the ARICH counter such as a radiators, photon detectors, readout electronics, and cables for the communication and power supply, and so on, has to fit in the space.

- Photon detectors have enough sensitivity for single photon detection and tolerance for a high magnetic field (1.5 T).

In order to measure momentum and sign of charge for every charged track in the high magnetic field, the photon detectors using for the ARICH counter has to keep their performances in the field up to 1.5 T.

- Radiator with long transmission length.

Information of the number of emitted Cherenkov photons is important, then we should avoid loss of them in the radiator medium. In the same time, the scattering of a Cherenkov light in the radiator becomes the source of decreasing the PID performance as decreasing number of detected photons and scattered Cherenkov light entries uncorrelated to the emission angle of the charged track in the radiator.

To satisfy the above requirements, we decided to use the proximity-focusing type Ring Imaging Cherenkov counter with aerogel radiators. In the following sections in this thesis, the detailed design of the ARICH counter will be discussed.

## 1.3 Motivation of this thesis

In this thesis, development of the ARICH counter for a charged particle identification at the super  $B$ -factory experiment is described.

In Chapter 2, the Belle II detector at SuperKEKB is described. In Chapter 3, an overview of the principle of the particle identification using Cherenkov counters and recent RICH counters employed in the high energy physics experiments are depicted. In Chapter 4, the concept and basic performance of the ARICH counter designed for the Belle II experiment are described. In Chapter 5, development of the HAPDs, which are used as photon detectors of the ARICH counter, is described. In particular, the improvements for the radiation hardness of the HAPDs are presented. In Chapter 6, studies for the performance of a prototype ARICH counter using an electron test beam are described. In Chapter 7, estimation of the PID performance based on an event-by-event analysis for the prototype ARICH counter, and performance evaluation of the ARICH counter at the super  $B$ -factory experiment are described. Finally, Chapter 8 concludes this thesis.

# Chapter 2

## The Belle II detector

In this chapter, the Belle II detector used for the super KEK  $B$ -factory (S-KEKB) at KEK is described.

### 2.1 Upgrading to Belle II

The Belle II experiment is proposed as a super  $B$ -factory experiment which is the new generation  $B$ -factory experiment to explore physics beyond the standard model. The accelerator and detector, which are named as SuperKEKB and Belle II, are not built from scratch but are basically upgraded from the previous experiment. In particular, the tunnel for the accelerator and the mechanical structure of the whole detector are reused. On the contrary, the beam-optics design of the main  $e^+$  and  $e^-$  storage rings are completely renewed. The SuperKEKB accelerator is briefly overviewed in the following subsection. Sub-detectors contained in the Belle II detector are described in section 2.2.

#### 2.1.1 SuperKEKB accelerator

##### Definition of luminosity

In the accelerator physics using the collider, the product frequency  $R$  of physics events such as  $e^+e^- (\rightarrow \Upsilon(4S)) \rightarrow B\bar{B}$  is defined as follows:

$$R = \mathcal{L}\sigma, \quad (2.1)$$

where  $\sigma$  is the cross section of an event of interest, and  $\mathcal{L}$  is called **luminosity**, which is usually defined as a unit of  $[\text{cm}^{-2}\text{s}^{-1}]$ . Since the cross section of  $e^+e^- \rightarrow B\bar{B}$  decay event is  $\sigma_{B\bar{B}} \simeq 1 \times 10^{-33} \text{ cm}^2$ , the previous KEKB accelerator [12] that achieved the luminosity of  $2.1 \times 10^{34} \text{ cm}^{-2}\text{s}^{-1}$ , could produce about 20  $B\bar{B}$  meson pairs per a second.

Improvement of the luminosity means that the number of produced  $B\bar{B}$  meson pairs per a second will be increased.

##### Design of the SuperKEKB

The KEKB  $B$ -factory will be upgraded to SuperKEKB using the same tunnel as KEKB. Fig. 2.1 shows the schematic view of the SuperKEKB accelerator.

The upgrade is based on the “Nano-Beam” scheme<sup>1</sup>. The basic idea of this scheme is to squeeze the vertical beta function at the IP ( $\beta_y^*$ ) by minimizing the longitudinal size of the overlap region of the two beams at the IP, which generally limits the effective minimum value of  $\beta_y^*$  through the “hourglass effect”. Fig. 2.2 shows a schematic view of the beam collision, which is a plane figure, in the Nano-Beam scheme. The size of the overlap region  $d$ , which is considered to be the effective bunch length for the Nano-Beam scheme, is much smaller than the bunch length ( $\sigma_z$ ). The length  $d$  is determined by the horizontal half crossing angle ( $\phi$ ) and the horizontal beam size at the IP ( $\sigma_z^*$ ) via the following equation:

$$d \cong \frac{\sigma_z^*}{\phi}. \quad (2.2)$$

The hourglass condition in the Nano-Beam scheme is expressed as

$$\beta_y^* > d, \quad (2.3)$$

instead of that for a usual head-on collision of

$$\beta_y^* > \sigma_z. \quad (2.4)$$

To shorten the length  $d$ , a relatively large horizontal crossing angle and extremely small horizontal emittances and horizontal beta functions at the IP for both beams are required. The luminosity of a collider  $\mathcal{L}$  is expressed by the following formula, assuming flat beams and equal beam sizes horizontal and vertical direction for two beams at the IP:

$$\mathcal{L} \simeq \frac{\gamma_{\pm}}{2er_e} \left( \frac{I_{\pm}\xi_{\pm}}{\beta_{y\pm}^*} \right), \quad (2.5)$$

where  $\gamma$ ,  $e$  and  $r_e$  are the Lorentz factor, the electron charge and the electron classical radius, respectively. The suffix  $\pm$  denotes the positron (+) or the electron (−). Therefore, the luminosity is mainly determined by the three fundamental parameters; i.e. the total beam current ( $I$ ), the vertical beam-beam parameter ( $\xi_y$ ) and the vertical beta function at the IP ( $\beta_y^*$ ). The design values of these three parameters, together with the beam energy and the luminosity and comparison with those parameters at the previous KEKB experiment is shown in Table 2.1. For the vertical beam-beam parameter  $\xi_y$ , we assume the same value of 0.09 as has been achieved at KEKB. The vertical beta functions at the IP for SuperKEKB are smaller by almost by a factor of 20 than those of the previous KEKB owing to the adoption of the Nano-Beam scheme. Assuming these parameters, we need to double the total beam currents compared with those of the previous KEKB to achieve the designed luminosity of SuperKEKB of  $8 \times 10^{35} \text{ cm}^{-2}\text{s}^{-1}$ .

Fig. 2.3 show the current luminosity projection of the SuperKEKB accelerator [30]. The top plot shows the integrated luminosity in unit [ $\text{ab}^{-1}$ ], and the bottom plot shows the achievement of the luminosity in unit [ $\text{cm}^{-2}\text{s}^{-1}$ ]. The goal of the integrated luminosity after 10-year SuperKEKB operation is  $50 \text{ ab}^{-1}$ .

<sup>1</sup>The nano-scheme was first proposed for the Super  $B$ -factory in Italy. However the Italy super  $B$ -factory project had been suspended.

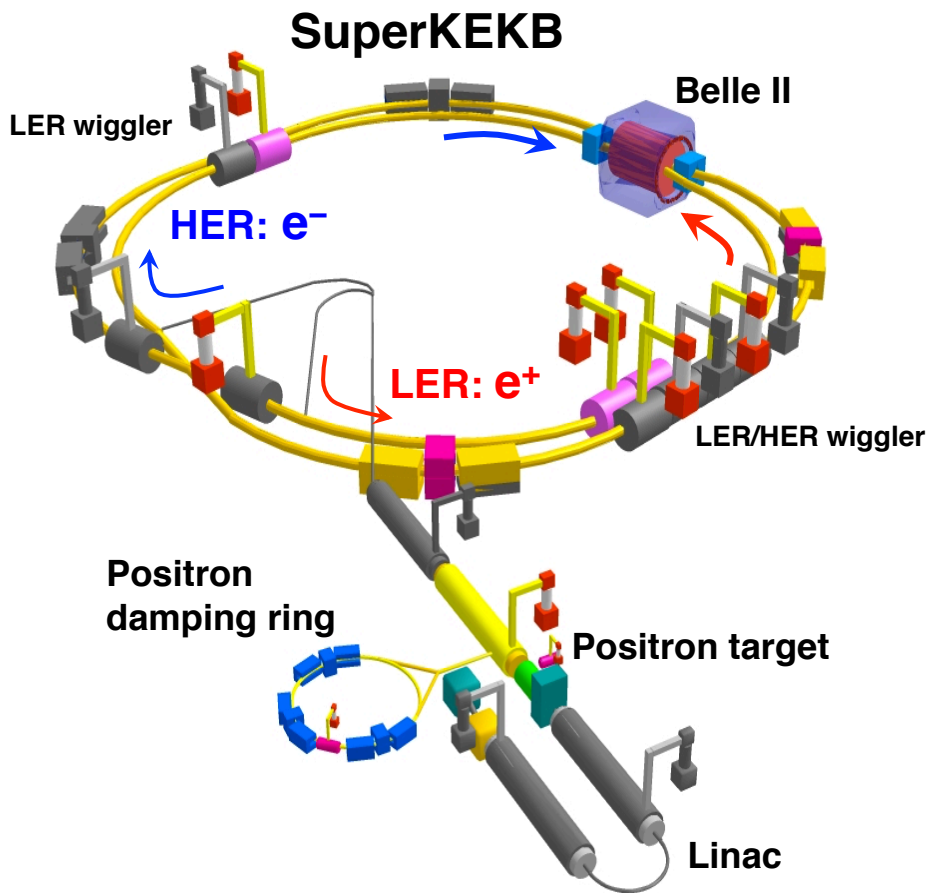


Figure 2.1: The illustration of the SuperKEKB accelerator.

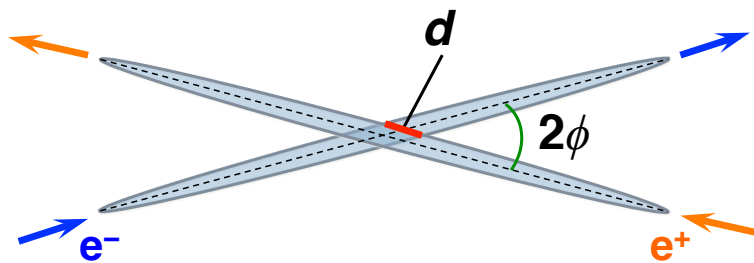


Figure 2.2: Schematic view of beam collision in the Nano-Beam scheme [29].

Table 2.1: Fundamental parameters of SuperKEKB and previous KEKB [29].

	KEKB Achieved	SuperKEKB
Energy (GeV) (LER/HER)	3.5/8.0	4.0/7.0
$\xi_y$ 0.129/0.090	0.090/0.088	
$\beta_y^*$ (mm)	5.9/5.9	0.27/0.41
Beam current $I$ (A)	1.64/1.19	3.60/2.62
Luminosity ( $10^{34} \text{ cm}^{-2}\text{s}^{-1}$ )	2.11	80

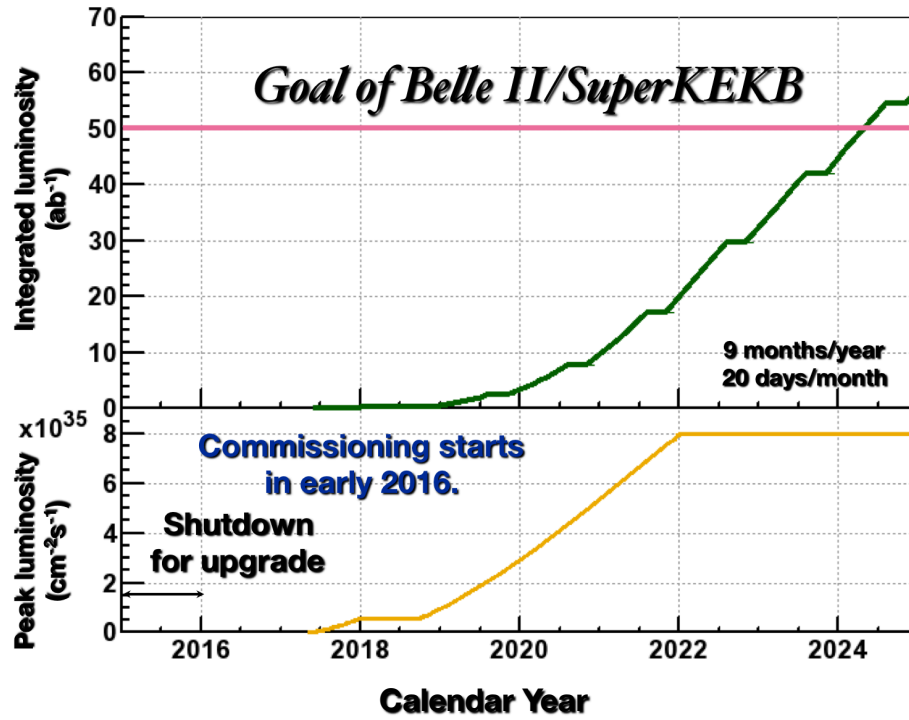


Figure 2.3: Luminosity projection of the SuperKEKB accelerator [30].

## 2.2 Belle II sub-detectors

Fig. 2.4 shows the 3-dimensional view of the schematic of the Belle II detector. Fig. 2.5 shows the schematic drawing of the Belle II detector. Although the outermost structure of this detector remain as the previous one, most of sub-detectors will be upgraded with minor improvements or replaced with brand new devices. The expected performance of Belle II sub-detectors is summarized in Table 2.2 [29].

### 2.2.1 Vertex detector: PXD, SVD

The vertex device that is used to determine the decay vertex of a  $B$  meson, uses the combination of PiXel Detector (PXD) and Silicon Vertex Detector (SVD).

The PXD is located in just outside the beam pipe, and consists of two-layer silicon pixel detector based on the DEPFET technology. The pixel size and the radius correspond to  $50 \times 50 \mu\text{m}^2$  and 14 mm for the inner layer, respectively, and  $50 \times 75 \mu\text{m}^2$  and 22 mm for the outer layer, respectively.

The SVD consists of four layers of the Double-Sided Silicon Strip Detectors (DSSDs). The inner radius of under most layer and outermost layer are 38 mm and 140 mm, respectively. The readout of the SVD is replaced to an ASIC chip called APV25. The APV25 chip have low-noise preamplifier and have a much shorter shaping time.

The impact parameter resolution  $\sigma_{z0}$  is expected to be  $20 \mu\text{m}$  by the combination of the PXD and the SVD.

### 2.2.2 Central Drift Chamber: CDC

The Central Drift Chamber (CDC) plays three important roles. First, it reconstructs trajectory of charged tracks and measures their momenta precisely. Second, it provides particle identification information using measurements of energy loss  $dE/dx$  within its gas volume. Low-momentum tracks that do not reach to the outer particle identification device, can be identified using the CDC alone. Finally, it provides efficient and reliable trigger signals for charged particles.

The He-C<sub>2</sub>H<sub>6</sub> gas, which was also used in Belle CDC, is used. To avoid the high-radiation and high-background region near the interaction point and to provide more space for the SVD, the radius of inner cylinder of the CDC is enlarged from in Belle (77 mm) to be 160 mm. While, since the Belle II barrel particle identification device (TOP) is more compact than that in Belle (TOF + ACC), the outer radius of the CDC is enlarged from that in Belle (880 mm) to be 1130 mm. The number of sense wires is 14,336 that is much more than in Belle (8,400), in particular, the new small cell chamber is introduced in innermost part of the CDC. The pitch size for innermost small cell and other parts consist of 5 mm and 8 mm, which are corresponding to the radial cell size of 10 mm and  $\sim 18.2$  mm, respectively.

The position resolution is expected to be  $100 \mu\text{m}$  for  $r$ - $\phi$  plane and 2 mm for  $z$ -direction. Other expected performances are listed in Table 2.2.

### 2.2.3 Particle Identification devices: TOP, ARICH

Charged particle identification devices will be completely replaced with brand new devices; the Time-of-Propagation (TOP) counter in the barrel-region, and the Aerogel RICH (ARICH) counter in the forward end-cap region. The both devices are to kinds of a Cherenkov counter with ring imaging scheme. The TOP counter is described in chapter 3.4.5. The development of ARICH counter is described in chapter 4, which is one of the main topics in this thesis.

### 2.2.4 Electromagnetic Calorimeter: ECL

To measure energy and detected position of electrons and photons, the Electromagnetic Calorimeter (ECL), that consist of an array of 8,736 crystals of CsI(Tl) scintillators, was used in Belle. The CsI(Tl) scintillation crystal array is reused. To cope with high background environment that is expected at Belle II, the readout electronics are replaced to perform the waveform sampling to separate signal hits from off-timing background hits. The beam background might be serious at forward end-cap region despite of the use of waveform sampling. To prepare for that situation, replacement of the crystals of forward end-cap region to pure CsI crystal that have much shorter time width than that of CsI(Tl), is discussed.

### 2.2.5 $K_L^0$ and Muon detector: KLM

To identify  $K_L^0$  and  $\mu$ , the  $K_L^0$  and Muon (KLM) detector that consists of the sandwich structure of the iron plate and the Resistive Plate Chamber (RPC), was used in Belle. The iron plates of KLM also behave as the return yoke of the magnetic field.

At Belle II, RPC modules in the end-cap part is replaced with scintillators instrumented with silicon photomultipliers such as SiPM, as RPCs can not work under the environment of high background rate.

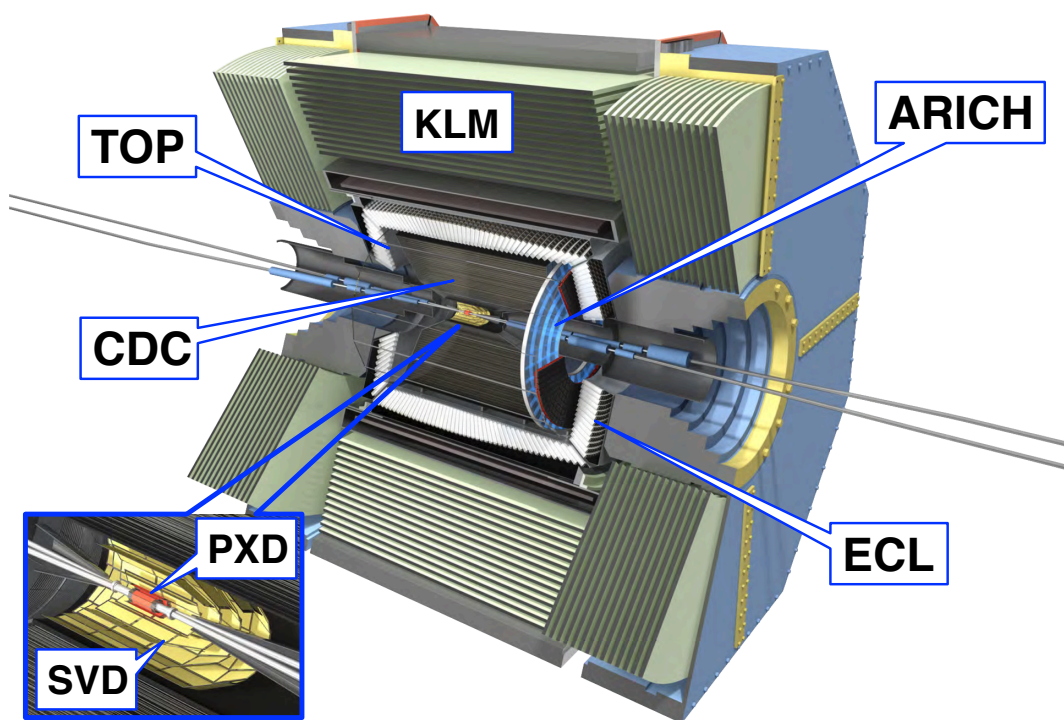


Figure 2.4: The three-dimensional illustration of the Belle II detector.

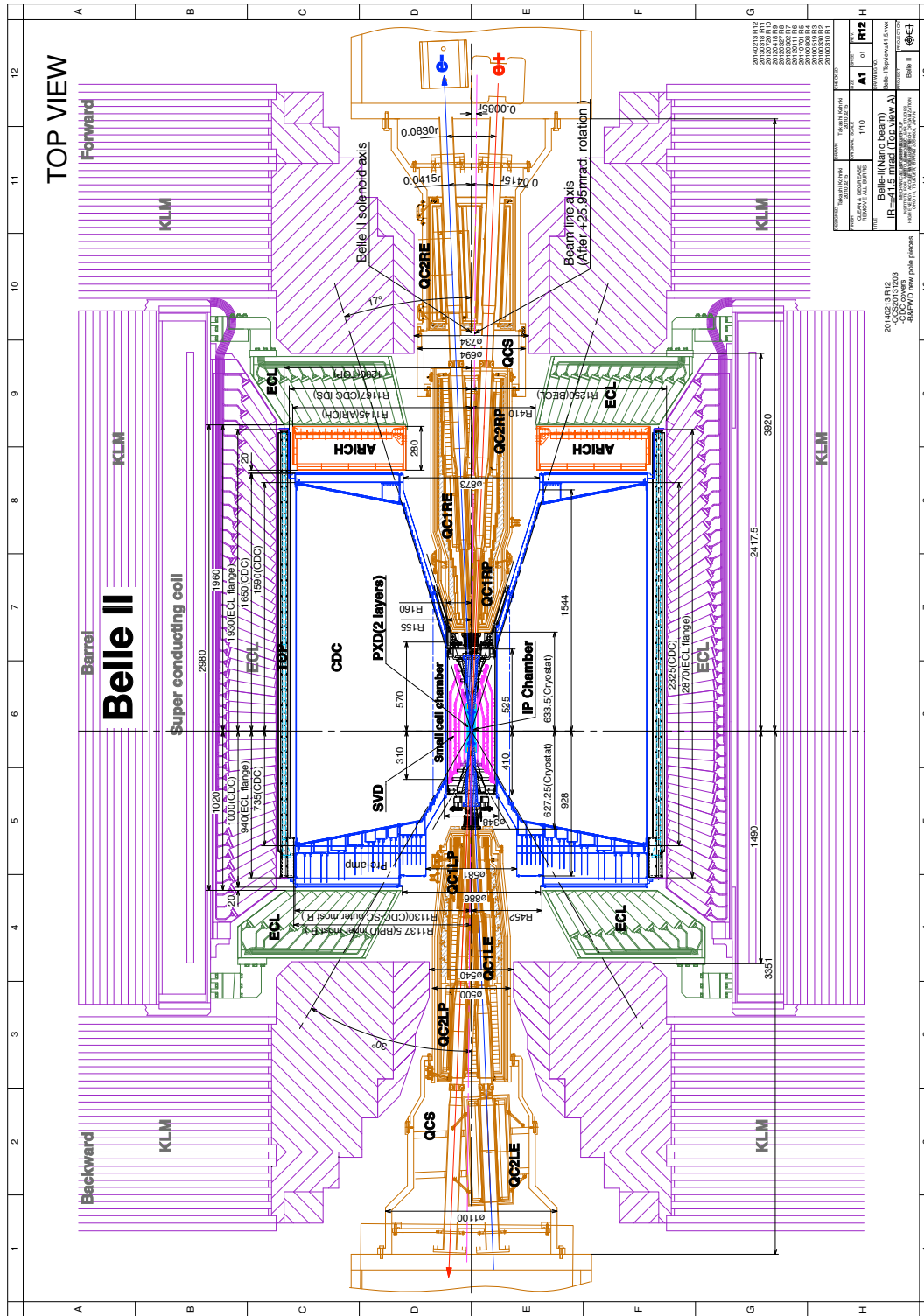


Table 2.2: Expected performance of components of the Belle II spectrometer [29].

Component	Type	Configuration	Readout	Performance
Beam pipe	Beryllium double-wall	Cylindrical, inner radius 10 mm, 10 $\mu\text{m}$ Au, 0.6 mm Be, 1 mm coolant (paraffin), 0.4 mm Be		
PXD	Silicon pixel (DEPFET)	Sensor size: $15 \times 100$ (120) $\text{mm}^2$ pixel size: $50 \times 50$ (75) $\mu\text{m}^2$ 2 layers: 8 (12) sensors	10 M	Impact parameter resolution $\sigma_{z_0} \sim 20 \mu\text{m}$ (PXD and SVD)
SVD	Double sided Silicon strip	Sensors: rectangular and trapezoidal Strip pitch: 50(p)/160(n)-75(p)/240(n) $\mu\text{m}$ 4 layers: 16/30/56/85 sensors	245 k	
CDC	Small cell drift chamber	56 layers, 32 axial, 24 stereo $r = 16\text{--}112 \text{ cm}$ $-83 \leq z \leq 159 \text{ cm}$	14 k	$\sigma_{r,\phi} = 100 \mu\text{m}$ , $\sigma_z = 2 \text{ mm}$ $\sigma_{p_t}/p_t = \sqrt{(0.2\%/p_t)^2 + (0.3\%/ \beta)^2}$ $\sigma_{p_t}/p_t = \sqrt{(0.1\%/p_t)^2 + (0.3\%/ \beta)^2}$ (with SVD) $\sigma_{dE/dx} = 5\%$
TOP	RICH with quartz radiator	16 segments in $\phi$ at $r \sim 20 \text{ cm}$ 275 cm long, 2 cm thick quartz bars	8 k	$N_{pe} \sim 20$ , $\sigma_t = 40 \text{ ps}$ $K/\pi$ separation : efficiency > 99% at < 0.5% pion fake prob. for $B \rightarrow \rho\gamma$ decays
ARICH	RICH with aerogel radiator	4 cm thick focusing radiator and HAPD photodetectors for the forward end-cap	78 k	$N_{pe} \sim 13$ $K/\pi$ separation at 4 GeV/c: efficiency 96% at 1% pion fake prob.
ECL	CsI(Tl) (Towered structure)	Barrel: $r = 125\text{--}162 \text{ cm}$ End-cap: $z = -102 \text{ cm}$ and $+196 \text{ cm}$	6624 1152 (F) 960 (B)	$\frac{\sigma_E}{E} = \frac{0.2\%}{E} \oplus \frac{1.6\%}{\sqrt{E}} \oplus 1.2\%$ $\sigma_{pos} = 0.5 \text{ cm}/\sqrt{E}$ (E in GeV)
KLM	barrel: RPCs end-caps: scintillator strips	14 layers (5 cm Fe + 4 cm gap) 2 RPCs in each gap 14 layers of (7-10) $\times$ 40 $\text{mm}^2$ strips read out with WLS and G-APDs	$\theta$ : 16 k, $\phi$ : 16 k 17 k	$\Delta\phi = \Delta\theta = 20 \text{ mradian}$ for $K_L$ $\sim 1\%$ hadron fake for muon $\Delta\phi = \Delta\theta = 10 \text{ mradian}$ for $K_L$ $\sigma_p/p = 18\%$ for 1 GeV/c $K_L$

# Chapter 3

## Overview of RICH counters

### 3.1 Introduction

In this chapter, overview of Cherenkov counters, which are used as particle identification (PID) devices using Cherenkov radiation, is described. The principle and classification of Cherenkov counters are presented, and finally the applications of the Cherenkov counters in high energy physics experiments, especially  $B$ -factory experiments are outlined.

#### 3.1.1 Cherenkov radiation

When the velocity of a charged particle  $v$  is higher than the velocity of light in a medium, that particle emits light like as the sonic boom from a supersonic body. The velocity of light in a medium is given as  $c/n$ , where  $n$  is the refractive index of the medium and  $c$  is the velocity of light in vacuum. Thus, we obtain the condition of a light emission as follows:

$$v \geq \frac{c}{n}, \quad (3.1)$$

in other words,

$$\beta \geq \frac{1}{n}, \quad (3.2)$$

where  $\beta$  is defined as  $v/c$ . This emission was first discovered by P. A. Cherenkov [31], therefore, the mechanism of light emission is named Cherenkov radiation. Here, if the both side quantities in Eq.(3.2) are equal

$$\beta_{\text{th}} \equiv \frac{1}{n}, \quad (3.3)$$

where  $\beta_{\text{th}}$  represents the threshold velocity of a Cherenkov radiation in a medium with  $n$ . Therefore, a particle, which has velocity below the  $\beta_{\text{th}}$ , does not emit any Cherenkov light in that medium.

Fig. 3.1 shows a schematic of a Cherenkov radiation from a charged particle traveling with a velocity of  $v = \beta c$ . The emission angle  $\theta_C$  shown in Fig. 3.1 is calculated by the

following equation:

$$\cos \theta_C \equiv \frac{\frac{c}{n} \Delta t}{v \Delta t} = \frac{1}{n\beta}. \quad (3.4)$$

Where,  $\Delta t$  is the time span of the charged particle passing in the medium. In general, we experimentally obtain momentum information of charged particles through track information in a magnetic field instead of getting their velocity  $\beta$  directly. The momentum of a charged particle can be calculated from the radius of curvature in a magnetic field. Here, we can use the following equation in order to obtain the momentum:  $p = 0.3\rho B$ , where  $p$  is the particle momentum (GeV/c),  $\rho$  is the radius of curvature (m), and  $B$  is the magnetic field (T), respectively. Thus, we can represent Eq.(3.4) as follows by replacing a  $\beta$  as a momentum  $p$ :

$$p = \frac{m}{\sqrt{n^2 \cos^2 \theta_C - 1}}, \quad (3.5)$$

where, we used the relationship as a  $\beta = |p|/E \equiv |p|/\sqrt{m^2 + p^2}$  and the natural unit ( $c = 1$ ). Accordingly, the following equation gives the threshold momentum  $p_{\text{th}}$ :

$$p_{\text{th}} = \frac{m}{\sqrt{n^2 - 1}}. \quad (3.6)$$

Fig. 3.2 shows the relationship between the threshold momentum  $p_{\text{th}}$  and refractive indices  $n$  for stable charged particles ( $e, \mu, \pi, K$  and proton).

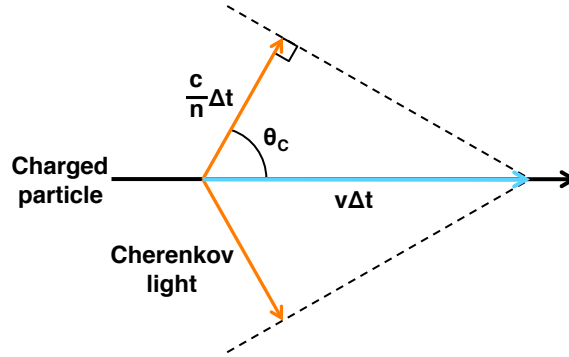


Figure 3.1: The schematic of the principle of a Cherenkov radiation.

### 3.1.2 Number of Cherenkov photons

The equation to estimate the number of emitted Cherenkov photons  $N_{\text{ph}}$  was proposed by I. M Frank and I. Y. Tamm in 1937 [32]. In general,  $N_{\text{ph}}$  depends on the wavelength of a emitted photon. In the case of a particle with charge  $ze$ ,  $N_{\text{ph}}$  for a wavelength  $\lambda$  is given by the Frank-Tamm relation<sup>1</sup> as follows:

$$\frac{d^2 N_{\text{ph}}}{d\lambda dx} = \frac{2\pi\alpha z^2}{\lambda^2} \left( 1 - \frac{1}{\beta^2 (n(\lambda))^2} \right) = \frac{2\pi\alpha z^2}{\lambda^2} \sin^2 \theta_C(\lambda), \quad (3.7)$$

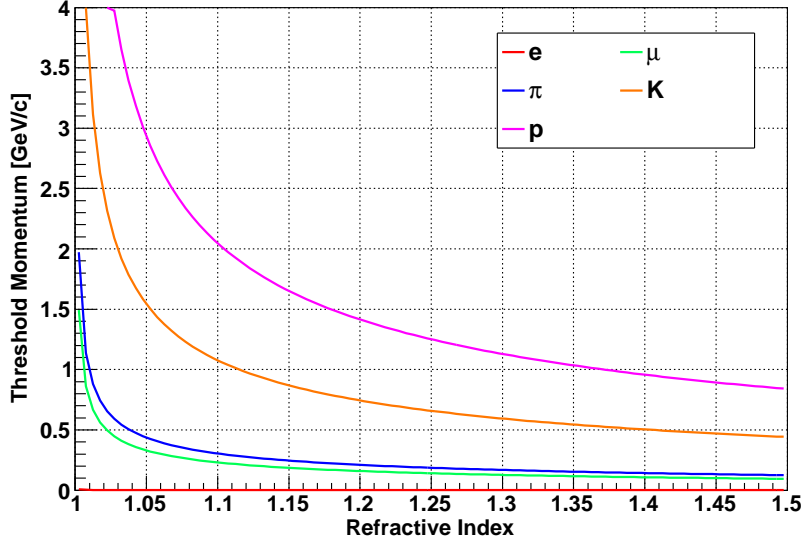


Figure 3.2: The plots of threshold momentum as a function of the refractive index by Eq.(3.6). Plots are calculated for major stable particles.

where,  $\alpha$  is the fine structure constant. Eq.(3.7) is equivalent to the following equation as a function of the photon energy:

$$\frac{d^2 N_{\text{ph}}}{dE dx} = \frac{\alpha^2 z^2}{r_e m_e c^2} \sin^2 \theta_C(E), \quad (3.8)$$

$$\sim 370 (\text{cm}^{-1} \text{eV}^{-1}) z^2 \sin^2 \theta_C(E), \quad (3.9)$$

where,  $r_e$  is the classical radius of an electron, and  $m_e$  is the electron mass, respectively. In practice, we use a photon detector with a certain detection efficiency  $\epsilon(E)$ , which is mainly consisted of the followings:

- Quantum efficiency  $\epsilon_Q(E)$  of the photon detector.
- Transparency  $T(E)$  and reflection  $R(E)$  of materials used for the entrance window of the photon detector.
- Geometrical acceptance  $\epsilon_A$  for the sensitive area of the photon detector.

By integration of Eq.(3.7) or Eq.(3.9) with taking the efficiency  $\epsilon(E)$  into accounts, we obtain the number of detected photoelectrons  $N_{\text{pe}}$  on the detector as follows:

$$N_{\text{pe}} = L N_0 z^2 \sin^2 \theta_C, \quad (3.10)$$

where,  $L$  is a path length of charged tracks in the radiator,  $N_0 \sim 370 (\text{cm}^{-1} \text{eV}^{-1}) \int \epsilon(E) dE$  is so called detector response parameter which indicates the detection performance considering all the efficiencies. When a typical photomultiplier tube (PMT) is used as the photon

<sup>1</sup>The work of the observation and characterized of a Cherenkov radiation by P. A. Cherenkov, I. M Frank and I. Y. Tamm between 1934 and 1944 was awarded the 1958 Nobel Prize in Physics.

detector,  $N_0$  is around  $60 \text{ cm}^{-1}$  [33]. In general,  $N_0$  took a quantity  $30\text{--}180 \text{ cm}^{-1}$  [34] in variation photon.

Fig. 3.3 show the number of detected photoelectrons as a function of track momentum  $p$ . These plots are estimated by Eq.(3.10) with the refractive index of  $n = 1.03$  and assuming the detector parameter with  $N_0 = 60 \text{ cm}^{-1}$ .

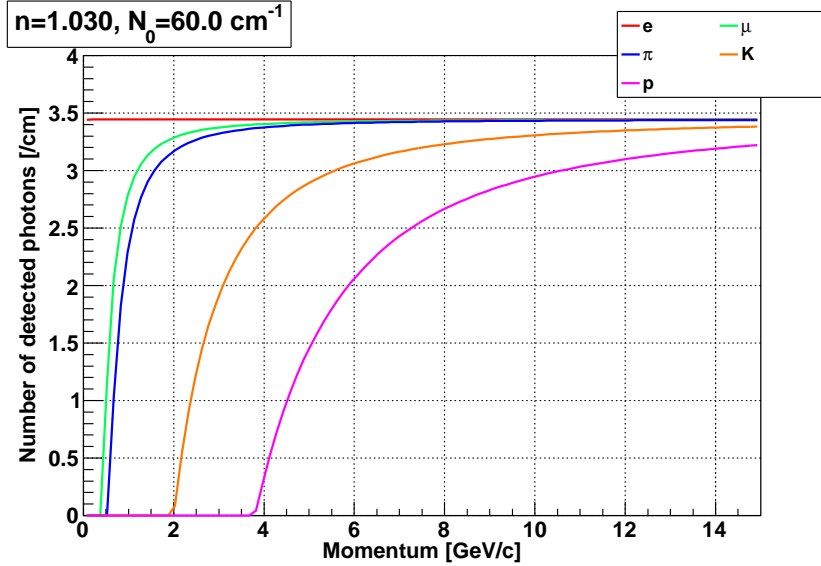


Figure 3.3: The number of photoelectrons as a function of a track momentum for major stable particles estimated by Eq.(3.10). This plots are assumed  $n = 1.03$  and  $N_0 = 60 \text{ cm}^{-1}$ .

### 3.1.3 Radiators

In adoption of a Cherenkov counter for particle identification, choice of a radiator material is quite important. Due to Eq.(3.6), we should choose a radiator having an appropriate refractive index according to the momentum range of interested particles. As the discussion in the above section, the number of emitted Cherenkov photon is a function of a refractive index  $n$  and a path length of charged tracks in the radiator  $L$ . Several commonly used materials as the radiator for Cherenkov counter systems are listed in Table 3.1.

Materials with lower refractive indices ( $< 1.01\text{--}1.03$ ), such as gases, are preferred to be used for particle identification in the high momentum range. Although the lower index radiator can not produce many Cherenkov photons, a gas radiator has an advantage in building large size radiators can easily expand the volume of them. In contrast, materials with larger refractive indices, such as liquids or solids, are used for a particle identification in the low momentum range. With the refractive indices over 1.05, most stable charged particles can emit Cherenkov light with threshold momentum  $p_{\text{th}} > 2 \text{ GeV}/c$  shown in Fig. 3.2.

Table 3.1: Commonly used medium materials and their refractive index [34].

Material	Refractive index
Air (dry, 1 atm)	1.000289
CO <sub>2</sub>	1.000449
CH <sub>4</sub>	1.000444
Silice aerogel	1.004–1.1
Water(H <sub>2</sub> O)	1.33
Fused quartz (SiO <sub>2</sub> )	1.46
Sodium chloride (NaCl)	1.54
Sodium iodide (NaI)	1.77

### Silica aerogel

The radiator material has to be highly transparent to be used for the Cherenkov counter. Silica aerogel is one of transparent solid materials widely used as radiators for Cherenkov counters. In 1990's a new production process, which can produce silica aerogels with lower refractive indices of 1.01–1.03 and hydrophobic, was established by the collaboration of KEK and Matsushita Electronic Works. Silica aerogel tiles thus produced were used for the threshold type Cherenkov Counter of the Belle experiment [35]. The hydrophobic property is important to prevent aged deterioration of transparencies. After the establishment of the new production process, silica aerogel tiles with lower refractive indices have been commercially available for various scientific experiments.

A silica aerogel tile consists of three-dimensional network of SiO<sub>2</sub> colloidal clusters. Fig. 3.4 shows an illustration of the three-dimensional structure of silica aerogel. The silica aerogel tile is generally obtained by drying solvent such as alcohol from alcoholic silica gel (alcogel). Then, silica (SiO<sub>2</sub>) clusters grow up to form three-dimensional networks, and then a silica aerogel tile is obtained by a special solvent drying process which is called **supercritical drying**. The refractive index of silica aerogel is mainly determined by its density. By adjusting-quantity of alcohol as the solvent in the alcogel synthesis, the density of the SiO<sub>2</sub> network connection can be controlled, thus the aerogel with any refractive index in the range 1.004 to 1.10 can be obtained in principle. In addition, by a special treatment in the alcogel synthesis and a drying the tiles with substitution of alcohol with CO<sub>2</sub>, hydrophobic silica aerogel tiles can be obtained [36].

## 3.2 Classification of Cherenkov counters

Following two informations from the Cherenkov radiation are available in order to identify charged particles:

1. The light emission yield that depends on the velocity of a charged particle. This information is useful where the velocity of a particle  $\beta$  is around the Cherenkov threshold ( $\beta \sim \beta_{\text{th}}$ ).
2. The Cherenkov emission angle  $\theta_C$  given by the particle mass  $m$  and momentum  $p$ . This information is usable where the velocity of a particle  $\beta$  is above the Cherenkov

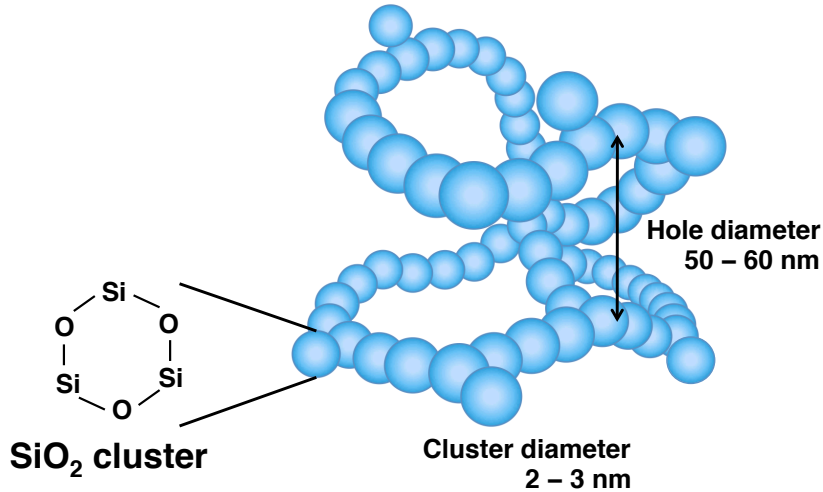


Figure 3.4: The illustration of three-dimensional networks of silica particles.  $\text{SiO}_2$  clusters become a primary particle with a diameter of 2–3 nm. They will connect each other three-dimensionally with hole-gap of 50–60 nm.

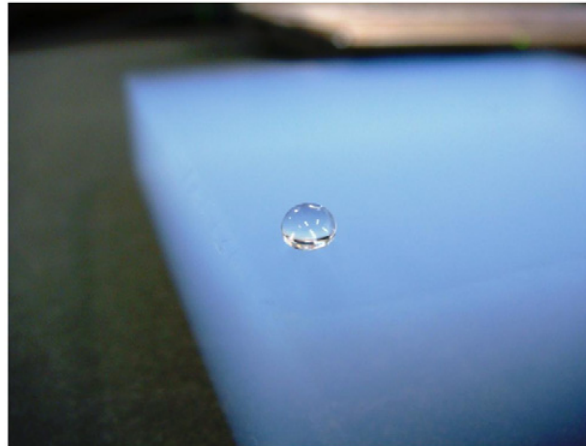


Figure 3.5: Picture of an aerogel tile with a low refractive index ( $n = 1.009$ ) and hydrophobic [36]. This aerogel was produced using the recently invented production method.

threshold ( $\beta > \beta_{\text{th}}$ ).

A threshold type Cherenkov counter uses only the former information. A Ring Imaging Cherenkov (RICH) counter uses both of them. Both type of Cherenkov counters are outlined in the following section.

### 3.2.1 Threshold type Cherenkov counter

If two particles having same momentum belong to different particle species, they should have different threshold momentum. For example, if we use a radiator with  $n = 1.05$ , pions can emit Cherenkov light at the momentum of 1 GeV/ $c$ , but kaons can't emit at

the same momentum as shown in the Fig. 3.2. Thus, we can perform  $\pi/K$  identification by observing a Cherenkov light emission.

A threshold type counter with a water radiator was first built by J. V. Jelley in 1951 in order to detect muons in cosmic-ray [37]. In 1958, a threshold type counter with a  $\text{CO}_2$  gas radiator was used by J. H. Atkinson and V. Perez-Mendez in order to select pions with a momentum requirement [38].

In high energy physics, radiators with refractive indices of more than 1.1 are disfavored for the threshold type counter, as most of stable charged particles can always emit Cherenkov lights at the momentum above  $1 \text{ GeV}/c$ . In order to make radiators have low refractive indices, gaseous radiators are commonly used as threshold type counters. As described in the previous section, silica aerogel tiles with a low refractive index of 1.03 or less is commercially available. Silica aerogel tiles are commonly employed as radiators of a threshold type Cherenkov counter such as the one used for  $\pi/K$  separation at the Belle experiment. The Aerogel Cherenkov Counter (ACC) system [13] employed by the Belle experiment is described as an example of threshold type counter.

### ACC system of Belle

The ACC system consist of 1,188 counter modules in total. The layout of ACCs in the Belle detector is shown as in Fig. 1.17. Fig. 3.6 show schematics of a typical ACC module employed at (a) barrel region and (b) end-cap region, respectively. ACC modules contain five silica aerogel tiles which are stacked in an aluminum box ( $12 \times 12 \times 12 \text{ cm}^3$ ). Due to the operation under high magnetic field of 1.5 T, a ACC module adopted one or two fine mesh-type photomultiplier tubes (FM-PMTs) as the photon detector [39].

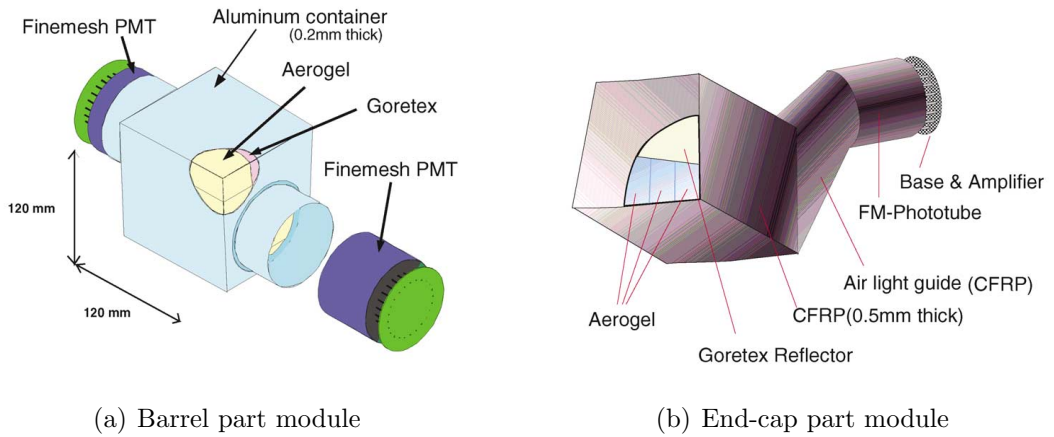


Figure 3.6: Illustrations of ACC modules for (a) barrel part, (b) end-cap part, respectively [13].

Both low refractive indices and high hydrophobic property are required for silica aerogels of ACC modules. On the contrary, such aerogels were not commercially available. Thus the ACC development group had to establish the new production method. They succeeded to provide the silica aerogel that satisfy their requirements [35]. Several different refractive indices were chosen for ACC modules to optimize the performance of  $\pi/K$

identification. As shown in Fig. 1.17, aerogel tiles with  $n = 1.010, 1.013, 1.015, 1.020,$  and  $1.028$  were used for barrel part modules, and end-cap part modules used only aerogel tiles with  $n = 1.030$ . Those refractive indices of the ACC system are chosen by taking account of the polar angle dependence of the Lorentz boost and of the availability of the other particle identification devices. Fig. 3.7 is a refractive index range used by ACC modules quoted from Fig. 3.2. For barrel region ACC is designed to perform  $\pi/K$  separation up to the maximum momentum of  $B$  meson decays, which corresponds to  $3.5 \text{ GeV}/c$  at the forward barrel region. The  $\pi/K$  identification at lower momentum region that is necessary to perform flavor tagging of  $B$  mesons, is covered by TOF system in the barrel region. However the TOF system is not placed in the end-cap region, thus the end-cap part ACC modules are designed to have only a refractive index of  $n = 1.030$  to cover  $\pi/K$  separation in the low momentum region, while losing the separation of high momentum pions and kaons coming from rare  $B$  meson decays.

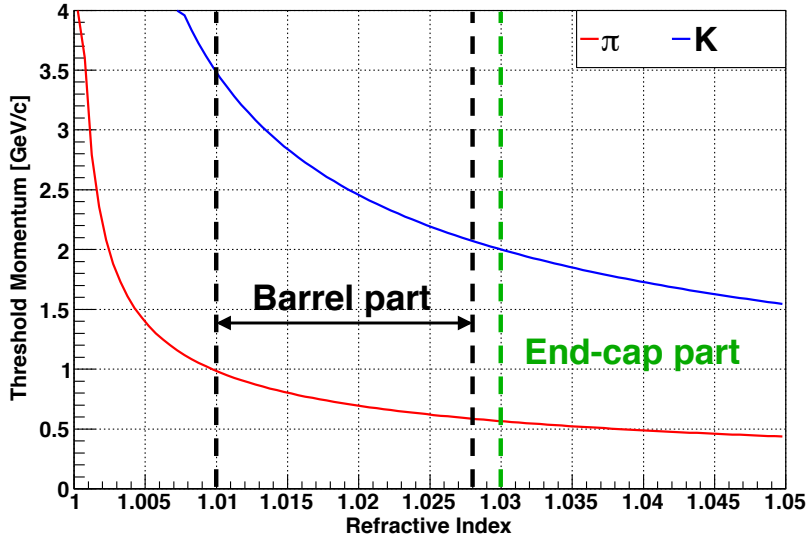


Figure 3.7: Threshold momentum  $p_{\text{th}}$  as a function of the refractive index  $n$  used for ACC modules. Solid lines correspond to pions (red) and kaons (blue), respectively. This plots are focused on a index range 1.00–1.05 from Fig. 3.2. Refractive index ranges used for barrel part and end-cap part are indicated as vertical dashed lines.

### 3.2.2 Ring imaging type Cherenkov counter

A Ring Imaging Cherenkov (RICH) counter performs particle identification by using the Cherenkov angle  $\theta_C$  that is obtained from the measurement of a radius  $r$  of the imaged Cherenkov ring. Since particle identification devices employ the RICH system work at above the Cherenkov threshold velocity  $\beta_{\text{th}}$ , they can cover wider momentum range compared with threshold type Cherenkov counters. The Cherenkov angle  $\theta_C$  is calculated for pions and kaons with various momenta by using Eq.(3.5) and shown in Fig. 3.8.

Original form of the RICH counter was proposed by A. Robert in 1966 [40]. It employed a two-dimensional image intensifier and a focusing lens to focus Cherenkov ring

images on the surface of the intensifier. This counter however was not practically in use because the intensifier had low quantum efficiency and have limited sensitive area. The practical RICH counter had first been proposed by J. Seguinot and T. Ypsilantis in 1977. They demonstrated that a Multi-Wire Proportional Chamber (MWPC), which consisted of the gas admixed with the photosensitive gas such as Benzene, was feasible to be uses as a photon detector of the RICH counter [41]. Cherenkov ring images had first been observed by G. Charpak *et al.* in 1979. They used a Multi-Step Avalanche Chamber (MSAC) with Tri-Ethyl-Amine (TEA) as the photosensitive gas [42]. Recently, multi-anode PMTs with high two-dimensional position sensitivity are available. Moreover silica aerogels with suitable refractive index and with high transparency are commercially available. Therefore, RICH counters utilize silica aerogel radiator and multi-anode PMTs have been widely used in recent high energy physics experiments.

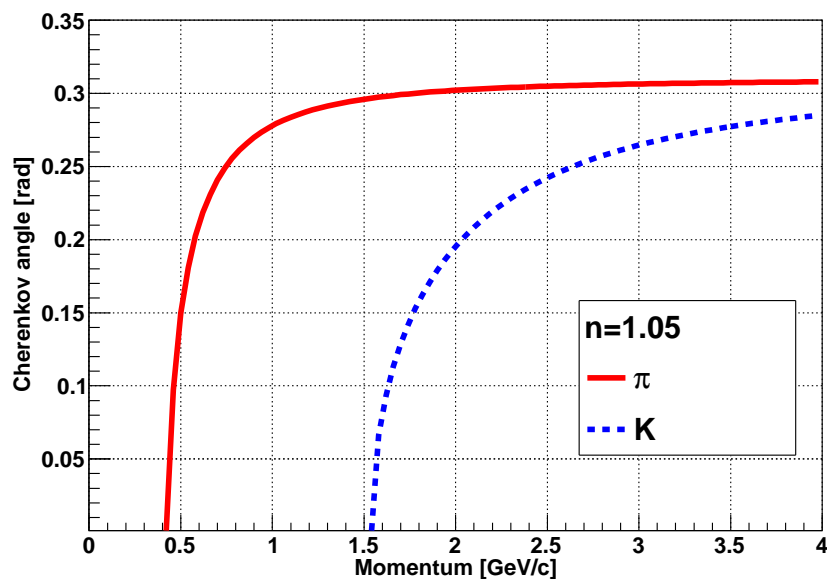


Figure 3.8: Cherenkov angle  $\theta_C$  as a function of the momentum of a pion (red solid line) and a kaon (blue dashed line).  $\theta_C$  was calculated in the radiator with the refractive index of 1.05.

### Focusing scheme

There're two types of RICH counters having different focusing scheme as shown in Fig. 3.9. Fig. 3.9 (a) is called as **Mirror focusing type** RICH counter, and was developed as original form of a RICH counter. This type of detector consists of a radiator, a focusing mirror, and a photon detector array, and focuses Cherenkov photons on the photon detector surface by a spherical mirror. Optical properties of focusing mirrors are required to be designed precisely, as the accuracy of the measurement of Cherenkov ring radius is determined by them.

Fig. 3.9 (b) shows the other RICH system which is called a **Proximity focusing type** RICH counter. This type counter measures a Cherenkov ring radius without any photon

focusing using mirrors. Therefore the optical design of this counter can be easy than a mirror focusing type. In order to prevent degradation accuracy of a Cherenkov ring radius measurement and to suppress loss of the number of detected photoelectrons by absorption or inner-scattering, the radiator have to be thin thickness should be used for this counter.

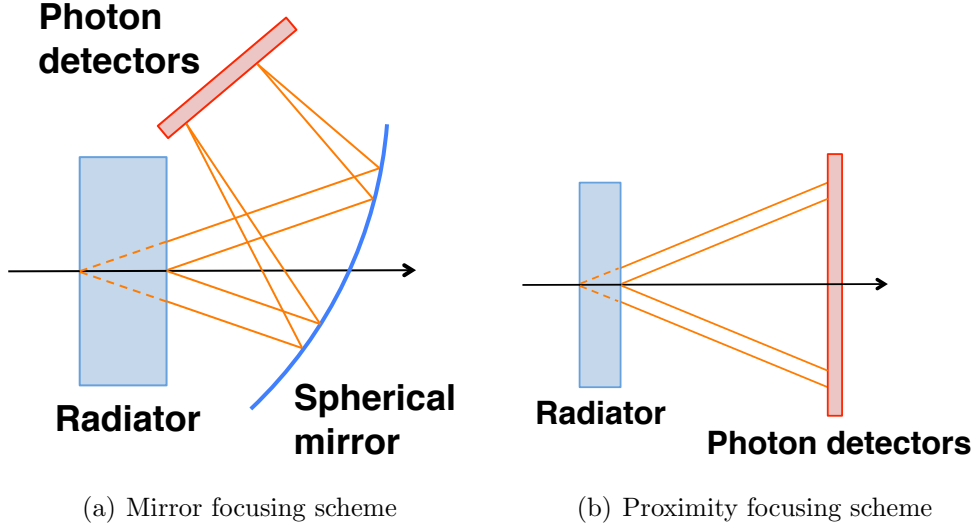


Figure 3.9: The two conceptual schematics of a RICH system.

### 3.3 Particle identification using a RICH counter

#### 3.3.1 Definition of separation power of PID

The number of standard deviation  $n_S$  to distinguish a particle  $A$  with mass  $m_A$  against a particle  $B$  with mass  $m_B$  ( $m_A < m_B$ ) at the same momentum  $p$ , is evaluated as follows:

$$n_S = \frac{|\theta_C(A) - \theta_C(B)|}{\sigma_\theta} \sqrt{N_{pe}}, \quad (3.11)$$

where  $\theta_C(A)$  and  $\theta_C(B)$  are the Cherenkov angle for the particle  $A$  and  $B$ , respectively,  $\sigma_\theta$  is the resolution in the Cherenkov angle measurement, and  $N_{pe}$  is the number of detected photoelectrons which are used for reconstruction of a Cherenkov ring.

$\theta_C(A)$  and  $\theta_C(B)$  are estimated by the Eq.(3.4).  $\sigma_\theta$  and  $N_{pe}$  are measured parameters and can be essentially estimated by the detector performance that is determined by the optical properties of a radiator, an accuracy of photon detection points, and geometries of detector components.

#### 3.3.2 Maximum momentum for particle identification

Momentum limits for particle identification to sustain the required separation power  $n_S$ , is described in this subsection. When a RICH counter, which is expected to have the

separation power  $n_S$  that is defined in the Eq.(3.11), discriminates a particle  $A$  with mass  $m_A$  from a particle  $B$  with  $m_B(> m_A)$ , the upper limit of the momentum  $p_{\max}$  is evaluated by the designed detector performance parameter  $k_c$  as follows [43, 44]:

$$p_{\max} = \sqrt{\frac{\Delta m^2}{2k_c n_S}}, \quad (3.12)$$

where  $\Delta m^2 = m_B^2 - m_A^2$ , and  $k_c$  is defined as following equation:

$$k_c = \tan \theta_C \frac{\sigma_\theta}{\sqrt{N_{\text{pe}}}}. \quad (3.13)$$

$k_c$  directly depends on the Cherenkov angle resolution  $\sigma_\theta$  and the number of photoelectrons  $N_{\text{pe}}$ . In the momentum range between  $p_{\text{th}}(A)$  and  $p_{\text{th}}(B)$ , a RICH counter operates as a threshold type effectively.

For example, if the separation power of  $n_S = 4$  were to be required at the maximum momentum of  $p_{\max} = 4 \text{ GeV}/c$ , the  $k_c$  of the RICH counter for  $\pi/K$  identification is required to be  $k_c = 1.8 \times 10^{-3}$ . In order to satisfy this detector performance parameter, refractive index of a radiator can be  $n = 1.03$  a radiator, then Cherenkov angle  $\theta_C$  for kaons is estimated to be 209 mrad at  $p_{\max}$ . If this RICH counter can detect  $N_{\text{pe}}$  to be 10,  $\sigma_\theta$  is required to be less than 26 mrad.

In order to achieve the required PID performance with a RICH counter, the optical properties of the radiator and the specification of the photon detector are necessary to be designed carefully.

## 3.4 RICH counters in high energy physics

RICH counters are realized as a performance particle identification device in high energy physics research. In this section, several RICH systems employed at  $B$ -factory experiments are overviewed.

### 3.4.1 HERMES RICH at HERA

The HERMES (HERA MEasurement of Spin) experiment [45] is a polarized deep inelastic scattering experiment at the HERA electron storage ring at DESY. In order to study spin structure of the nucleon, the HERMES experiment is a fixed target experiment with 27.5 GeV electron (or positron) beam and internal gas targets of polarized and unpolarized hydrogen, deuterium etc. Fig. 3.11 (a) shows the cross-sectional view of the HERMES detector design.

The spectrometer of HERMES adopted RICH system for hadron ( $\pi$ ,  $K$ , proton) identification [44, 46]. The HERMES RICH counter is located about 5 m downstream of the target and is sandwiched by tracking devices. The HERMES RICH counter was designed to separate pions and kaons up to 15 GeV/ $c$ . In order to achieve the above performance, the HERMES RICH counter adopted a dual-radiator RICH scheme which employed silica aerogels and  $\text{C}_4\text{F}_{10}$  gas as radiators. This is the first case that a silica aerogel was adopted

as radiator of a RICH system in a high energy physics experiment with accelerators. Refractive indices of radiators were corresponding to 1.00137 and 1.03 for  $C_4F_{10}$  and a silica aerogel, respectively. The momentum range of  $\pi/K$  identification were overlapped for these radiators.  $\pi/K$  identification in the low momentum region up to  $6.7 \text{ GeV}/c$  was covered by an aerogel radiator, and the high momentum region of  $2.7\text{--}15 \text{ GeV}/c$  was covered by the  $C_4F_{10}$  radiator, respectively.

Fig. 3.10 (b) shows the illustration of the HERMES RICH counter. 425 aerogel tiles with size of  $114 \times 114 \times 11.3 \text{ mm}^3$  were employed, and 5 tiles were stacked in five layers, with 5 horizontal rows and 17 vertical columns. The radius of curvature of the mirror array was 2.20 m. Produced Cherenkov photons by silica aerogel tiles or  $C_4F_{10}$  were reflected by the spherical mirror array and were focused on the photon detector matrix. Two Cherenkov rings with differential radii were designed to be observed. PMTs with a diameter of 18.6 mm were adopted as a photon detector, and these PMTs were arranged to  $23.3 \text{ mm} \times 23.3 \text{ mm}$  pitch.

By analyzing experimental pion track data [44], RICH parameters of the HERMES RICH system were obtained the single Cherenkov angle resolution of  $\sigma = 7.6 \text{ mrad}$  and  $7.5 \text{ mrad}$  for an aerogel and  $C_4F_{10}$ , respectively.

### 3.4.2 HERA-B RICH at HERA

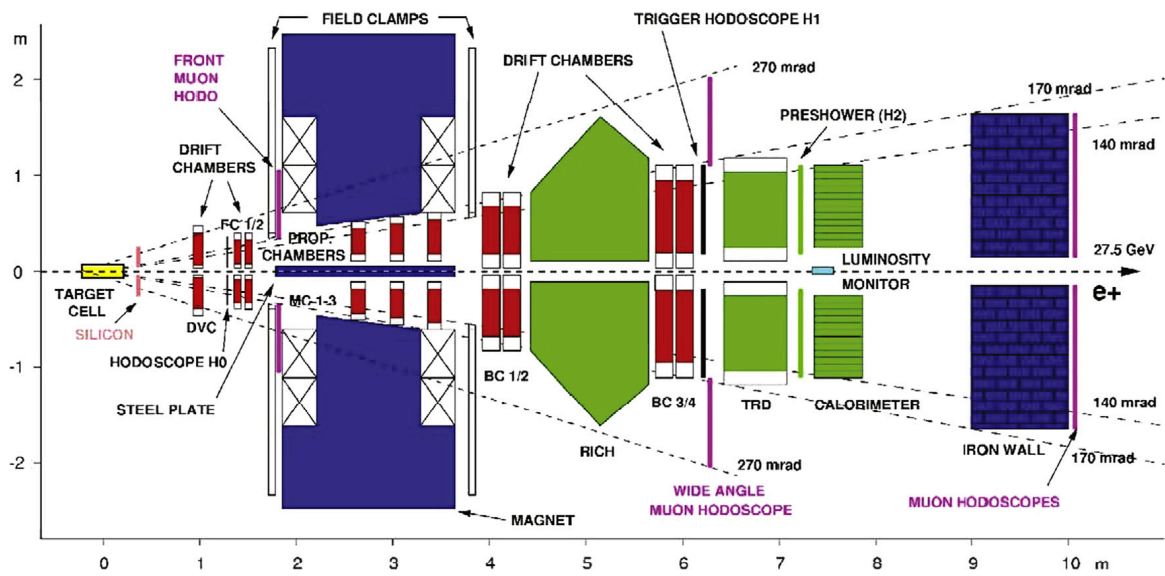
The HERA-B experiment is a fixed target experiment at the HERA proton storage ring at DESY and is designed to measure rare  $B$  meson decay processes [47]. In order to produce  $B$  mesons, protons with  $920 \text{ GeV}$  are injected to a fixed wire target. Fig. 3.11 (a) shows the cross-sectional view of the HERA-B detector design.

In the HERA-B experiment, a gaseous RICH system was adopted to distinguish kaons from pions [48]. Fig. 3.11 (b) shows the cross-sectional view of schematic design of the HERA-B RICH counter. The HERA-B RICH counter was designed to separate kaons and pions up to  $50 \text{ GeV}/c$  at the interaction rate up to  $40 \text{ Hz}$ . The gas radiator vessel in the HERA-B RICH counter was placed about  $10 \text{ m}$  downstream along the beam direction from the fixed target. The HERA-B RICH counter employed Perfluorobutane gas  $C_4F_{10}$  as a radiator, which have refractive index of  $n = 1.00137$ . The threshold momentum for kaons corresponds to  $9.6 \text{ GeV}/c$  in this radiator gas, therefore this counter was also used as the threshold type counter up to  $9.6 \text{ GeV}/c$ .

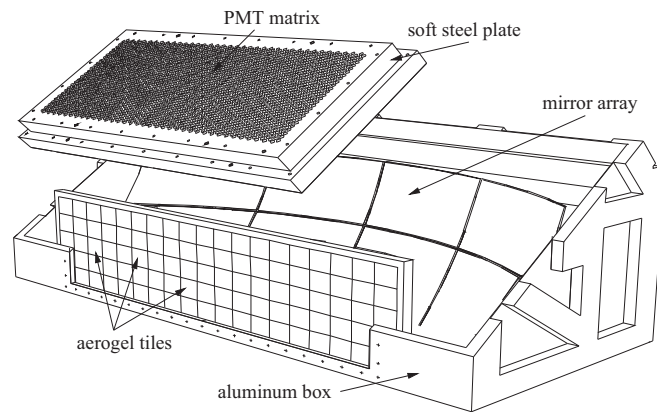
This counter used a dual mirror focusing scheme. Cherenkov photons produced by the entering charged track in the gas vessel were collected on the primary mirror array. The primary mirror, which have spherical shape of a curvature of  $11.4 \text{ m}$ , was used for focusing the Cherenkov photons onto the second mirror surface. The secondary mirror of planar shape imaged a Cherenkov ring on the photon detector surface. Both mirrors were placed inside of gas radiator vessel.

This was the first experiment that a multi-anode PMT was used as the imaging photon detector in a RICH system [48]. Two types of multi-anode PMTs, which consisted with Hamamatsu multi-anode R5900-00-M16 and R5900-03-M4 for 16 and 4 square shaped channels, respectively, were adopted. One type of PMT consisted with 16 squared shaped pads of  $4.5 \times 4.5 \text{ mm}^2$ , the other consisted with 4 squared pads of  $9 \times 9 \text{ mm}^2$ .

By analyzing the collision data of the HERA-B experiment [48], RICH parameters of



(a) The cross-sectional view of the HERMES detector



(b) The HERMES RICH counter

Figure 3.10: The schematics of the HERMES detector (a) and the RICH counter (b) [45, 44, 46].

the HERA-B RICH system were evaluated the single Cherenkov angle resolution to be  $\sigma = 0.7 \text{ mrad}$  and the number of photoelectrons to be  $N_{\text{pe}} = 33$  for  $\beta = 1$  particles.

### 3.4.3 BaBar DIRC at PEP-II

The BaBar detector [10] at the PEP-II accelerator at the SLAC adopted the unique RICH counter, which is called as Detector of Internally Reflected Cherenkov light (DIRC) [14], as the  $\pi/K$  identification device. The principle of a DIRC counter is described in below. Cherenkov photons from a charged track of  $\beta \sim 1$  in a quartz bar have the emission angle that is depending on the track incident angle and is below the total internal reflection angle, therefore they propagate to ends of a quartz bar. When propagated photons exit from quartz bar end, they have a large angle with respect to the quartz bar axis. Then these photons are detected by the position sensitive photon detectors at the outside of a quartz bar and are reconstructed as a ring image.

Fig. 3.12 show the cross-sectional view of the BaBar detector (a) and the BaBar DIRC counter (b). The BaBar DIRC counter was designed to separate pions and kaons coming from  $B$  meson decays over a momentum range of  $0.7\text{--}4.2 \text{ GeV}/c$ . A radiator of the DIRC counter was silica fused quartz with the refractive index of 1.473. Twelve quartz bars of  $4.9 \text{ m} \times 6 \text{ cm}^2$  were used, and they were installed at outside of the Drift Chamber (DCH) which provided the incident position and momentum of a track entered to the DIRC counter. The forward quartz bar end was instrumented with a mirror to reflect photons that is emitted to forward direction to backward direction. Propagated photons were detected by a PMT array located about  $1.2 \text{ m}$  away from the bar end, they were traveling through a expansion region filled with the ultra-pure water of about  $6,000 \ell$ . 10,752 PMTs having had a diameter of  $2.82 \text{ cm}$  formed a PMT array.

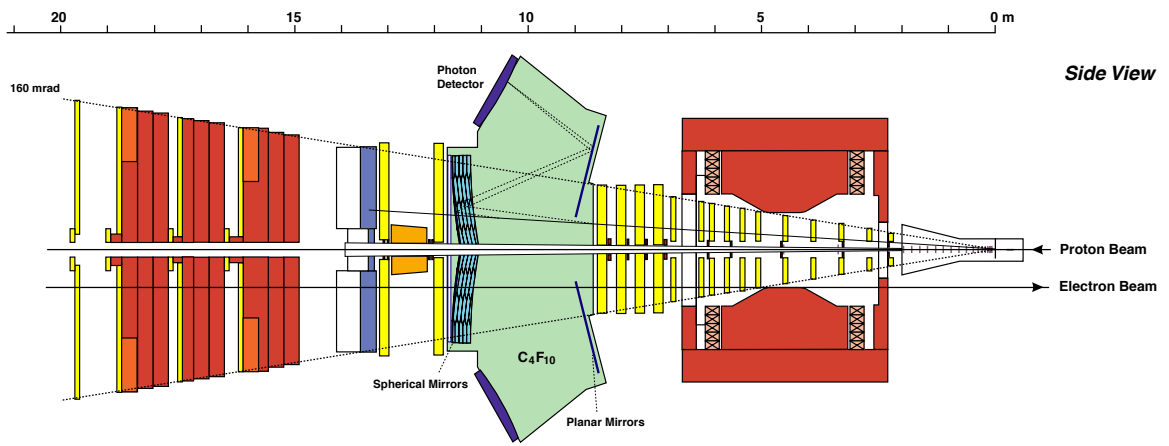
The DIRC counter is a three-dimensional imaging device, which uses both the two-dimensional position and timing information. Therefore the DIRC counter could reject random background hits that have inconsistent timing compared to the TOF timing. The PMTs of the DIRC counter had averaged time resolution of  $1.5 \text{ ns}$ .

By analyzing  $e^+e^- \rightarrow \mu^+\mu^-$  events [14], RICH parameters of the DIRC counter were evaluated. The Cherenkov angle resolution was evaluated to be  $\sigma = 2.5 \text{ mrad}$  per track and the averaged number of photoelectrons  $N_{\text{pe}}$  were evaluated to be about 17 for perpendicular incidence to nearly 60 for polar angles towards the forward and backward regions.

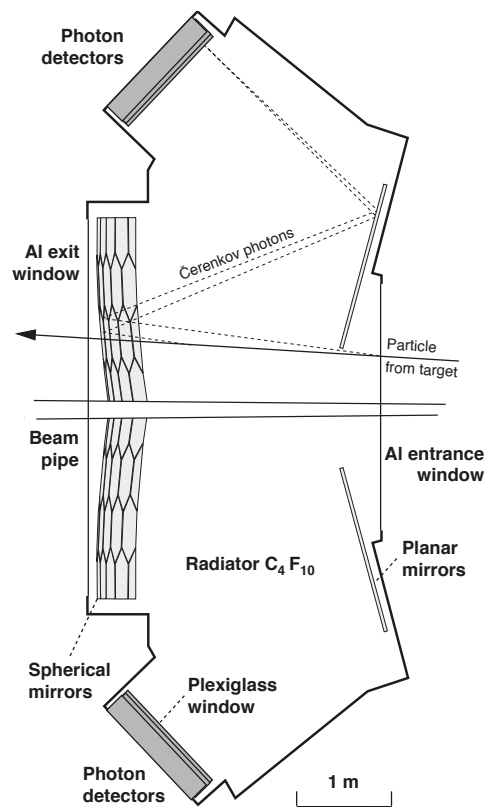
### 3.4.4 LHCb RICH at LHC

LHCb is one of the experiments at LHC collider at CERN, and is currently the sole running (super)  $B$ -factory experiment in the world. The LHCb experiment aims the high precision measurement of the  $CP$  violation in  $B$  meson system and rare decays of  $B$  mesons. Fig. 3.13 (a) shows the cross-sectional view of the LHCb detector [49]. In order to perform  $\pi/K$  identification in a momentum range of  $1\text{--}100 \text{ GeV}/c$ , the LHCb detector [49] uses two RICH counters, RICH1 and RICH2.

Fig. 3.13 (b) and (c) show cross-sectional view of the two RICH counters of LHCb [50]. The RICH1 counter, which can provide information of  $\pi/K$  separation in low momentum

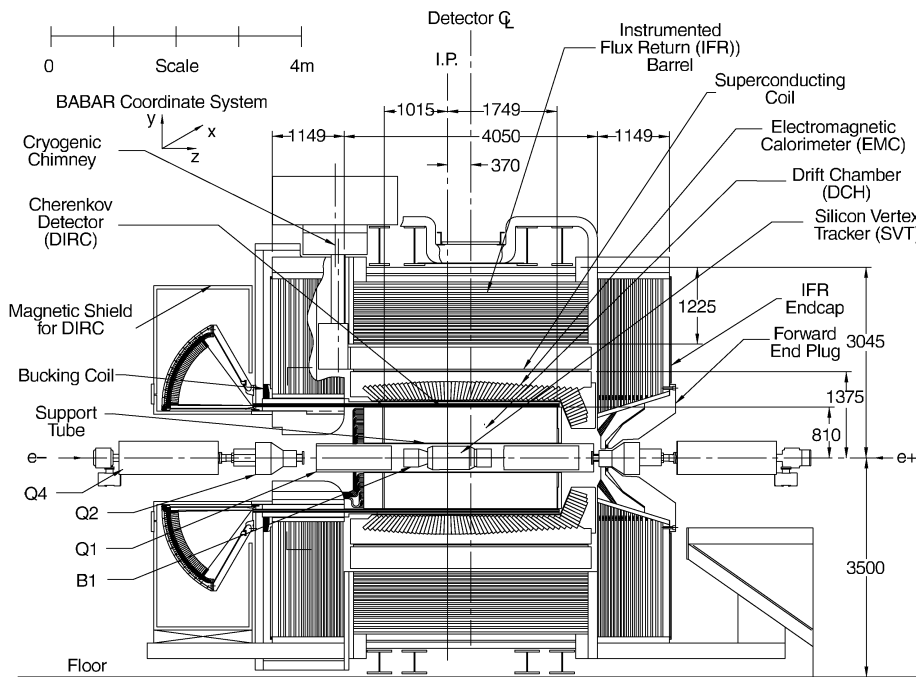


(a) The cross-sectional view of the HERA-B detector

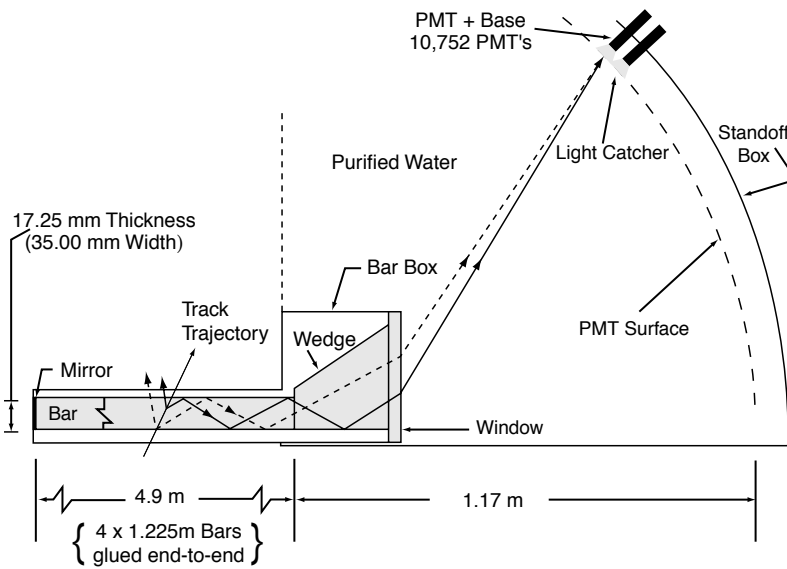


(b) The HERA-B RICH counter

Figure 3.11: The schematics of the HERA-B detector (a) and the RICH counter (b) [48].



(a) The cross-sectional view of the BaBar detector



(b) The HERA-B RICH counter

Figure 3.12: The schematics of the BaBar detector (a) and the DIRC counter (b) [10, 14].

region of 1–60 GeV/ $c$ , is located directly behind the vertex detector. The RICH1 covers the horizontal angular acceptance of 300 mrad. This counter has two radiators of different refractive indices. A silica aerogel have a refractive index with  $n = 1.03$  and  $C_4F_{10}$  gas have a refractive index of  $n = 1.0014$ . The thickness of an aerogel tile is 5 cm. The RICH1 system adopts almost the same mechanism of the HERMES RICH counter's: Cherenkov photons, which are produced in aerogel as an entering wall and  $C_4F_{10}$ , are focused on the photon detector surface by the spherical mirror array as shown in Fig. 3.13 (b). Then the RICH1 obtains two rings of different radii from aerogels and  $C_4F_{10}$ .

The RICH2 counter, which can provide information of  $\pi/K$  separation in high momentum region of 15–100 GeV/ $c$ , uses a single radiator made of  $CF_4$  gas with  $n = 1.0005$ . This counter is located behind the magnet and the tracking system. The RICH2 covers the horizontal angular acceptance of 120 mrad as shown in Fig. 3.13 (c). The RICH2 have almost the same mechanism of the HERA-B RICH counter's: produced Cherenkov photons are focused by the primary spherical mirrors and the secondary planar mirrors.

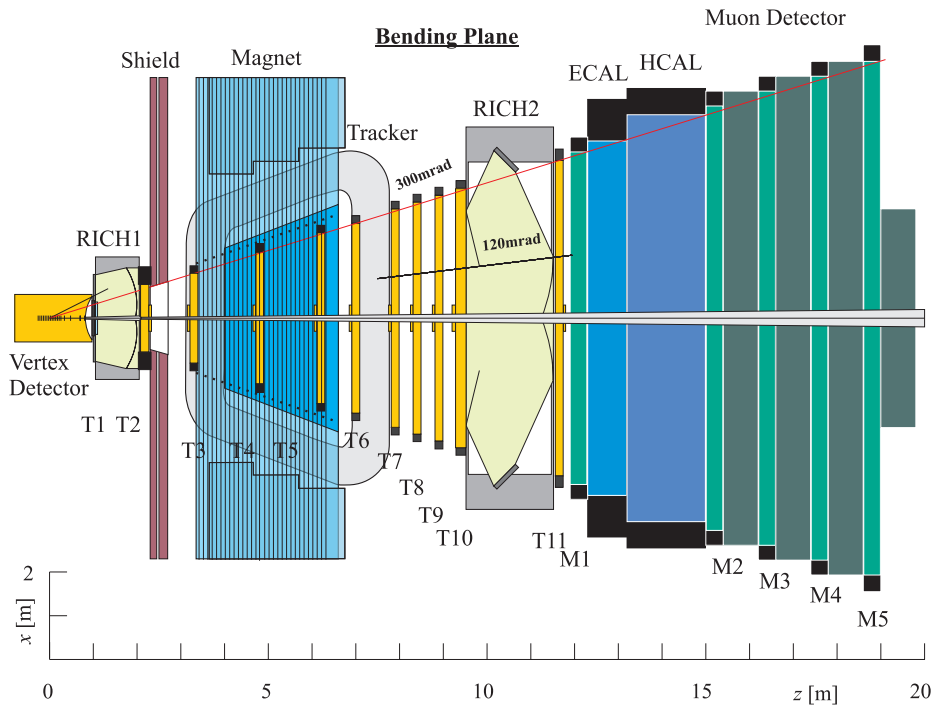
In order to satisfy the requirements for LHCb RICH systems, the LHCb collaborators developed a new photon detector, which is a pixellated Hybrid PhotonDiodes (HPD) tube. The HPD tube contains the pixelated silicon sensor chip, that is divided by  $32 \times 32 = 1024$  pixels with  $500 \times 500 \mu\text{m}^2$  as a pixel size. 168 and 262 HPD tubes are used in RICH1 and RICH2, respectively.

From analyzing proton collision data [51], performance of the LHCb RICH system were evaluated. The single Cherenkov angle resolution was evaluated to be  $\sigma = 1.618$  mrad, 0.68 mrad, and 5.0 mrad for  $C_4F_{10}$ ,  $CF_4$ , and aerogels, respectively. From analyzing tagged  $D^0 \rightarrow K^-\pi^+$  decay events [51], the number of photoelectrons were obtained to be  $N_{pe} = 20.4$ , 15.8, and 5.0 for  $C_4F_{10}$ ,  $CF_4$ , and aerogels, respectively.

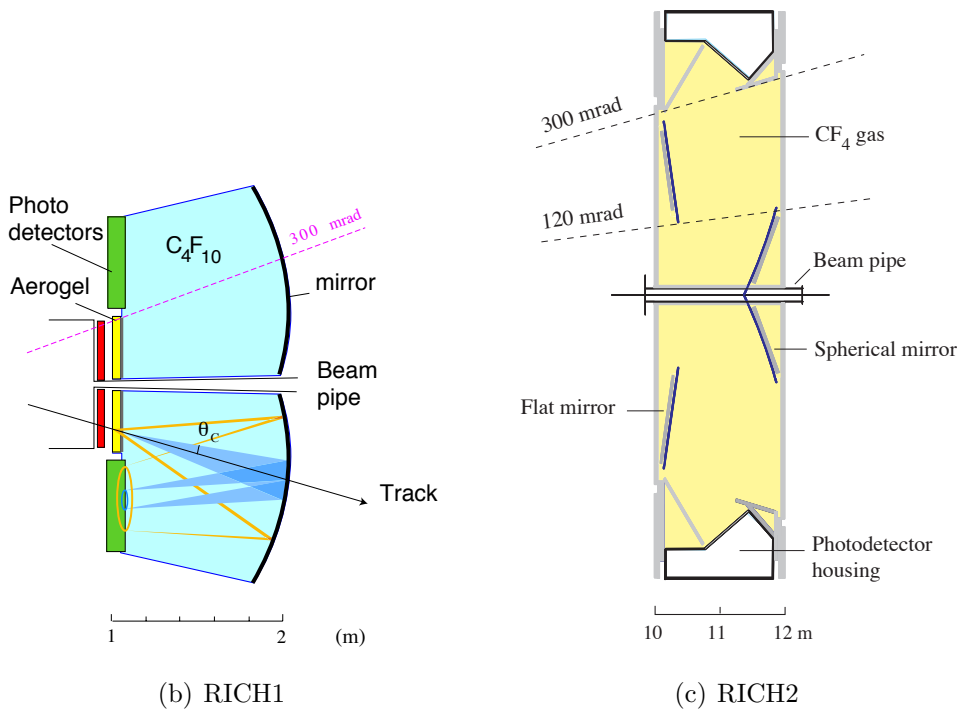
### 3.4.5 Belle II TOP at Super KEKB

The TOP counter [52] is located in the barrel region the Belle II detector as shown in Fig. 2.4, and is one of the Cherenkov counter based on the totally internally reflecting RICH scheme that is similar to that of the Babar DIRC counter as shown in Fig. 3.12 (b). Fig. 3.14 shows the overview of the TOP counter [53]. This counter is designed to perform  $\pi/K$  separation with high precision in momentum range up to 4 GeV/ $c$ . The TOP counter have the combined quartz optics, which consists of two fused silica quartz bars, spherical focusing mirror, and of a prism-shape expansion block. In order to propagate Cherenkov photons inside the radiator with preserving the Cherenkov ring image, the sides of radiators are required to be flat and parallel to a very tight tolerance. The designed flatness is less than  $10\lambda$  ( $\lambda$  is wavelength of a Cherenkov photon) over the entire bar length ( $\sim 1.2$  m). The roughness of the quartz surface required to be less than  $5 \text{ \AA}$  r.m.s. to minimize photon loss.

The Cherenkov ring image is reconstructed using the three-dimensional information provided by the position of two-dimensional coordinates  $(x, y)$  and precise timing by a fine time resolution photon detector. The 4-ch micro-channel plate Photo Multiplier tube (MCP-PMT) is adopted as the photon detector. The MCP-PMT for the TOP counter has a single photon timing resolution of about 30 ps under a magnetic field of 1.5 T. The TOP counter contains 16 quartz bar module, which has 32 MCP-PMTs.



(a) LHCb detector



(b) RICH1

(c) RICH2

Figure 3.13: (a) The cross sectional view of the LHCb detector [49]. The LHCb detector has two RICH counters, RICH1 (b) and RICH2 (c) [50]. The RICH1 counter employs the combination of silica aerogels and  $C_4F_{10}$  gas radiators. The RICH2 counter employs  $CF_4$  gas radiator.

The prototype TOP counter was tested with  $8\text{ GeV}/c$  electron beam [53]. From the beam test, we find then the time resolution to be about  $100\text{ ps}$ , including the intrinsic resolution, PMT jitter, beam timing fluctuation. This time resolution and the distribution of the number of photon hits show good agreement with the expectation of Monte Carlo simulation.

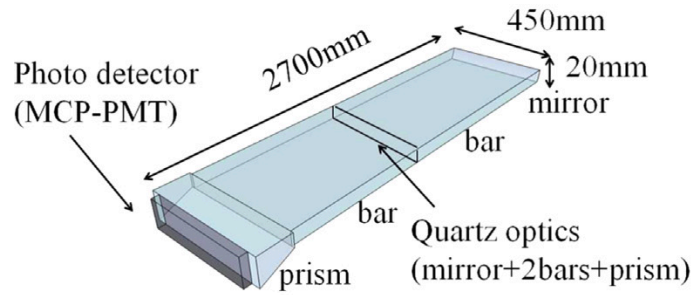


Figure 3.14: Conceptual overview of TOP counter [53].

# Chapter 4

## The ARICH counter

In this chapter, the conceptual design of the Aerogel Cherenkov counter of the Belle II detector is described.

### 4.1 Design concepts

As discussed in chapter 1, in order to perform the charged particle identification (PID) in the end-cap region of the Belle II detector at the wide momentum range up to  $4 \text{ GeV}/c$ , the Aerogel Ring Imaging Cherenkov (ARICH) counter was adopted. In this section, the design of the ARICH counter and elements used for this counter which satisfy the required performances are described.

As shown in the chapter 1, the ARICH counter used for the Belle detector is required to have the following conditions:

1. A whole structure has to be installed within the available space of 280 mm in the direction of the beam axis as shown in Fig. 4.1.
2. A position sensitive photon detector has to have to be the enough sensitivity for single photon detection and tolerance for a high magnetic field (1.5 T).
3. A radiator has to have a sufficiently long transmission length.

In order to satisfy the first condition, the proximity focusing type RICH system is adopted because focusing mirror system requires additional volume for focusing of reflected photons. Performance of a RICH counter is mainly determined by the Cherenkov angle resolution  $\sigma_\theta$  and the number of detected photoelectrons  $N_{\text{pe}}$ . The Cherenkov angle resolution  $\sigma_\theta$  is contributed by the ambiguity of the emission point inside of the radiator, the measurement error originated from a spacial resolution of the photon detector, and the chromatic error of the radiator material. To avoid deterioration of performance caused by these contributions, the choice of the suitable photon detector and the radiator material is very important.

After the careful study, the dual silica aerogel layer and the 144-ch Hybrid Avalanche Photo Detectors (HAPDs) were finally adopted as the radiator and the photon detector, respectively. The conceptual design of ARICH counter as shown in Fig. 4.2. The reasons

why the silica aerogel radiator and the HAPD are the suitable element of the ARICH counter are described in the following sections.

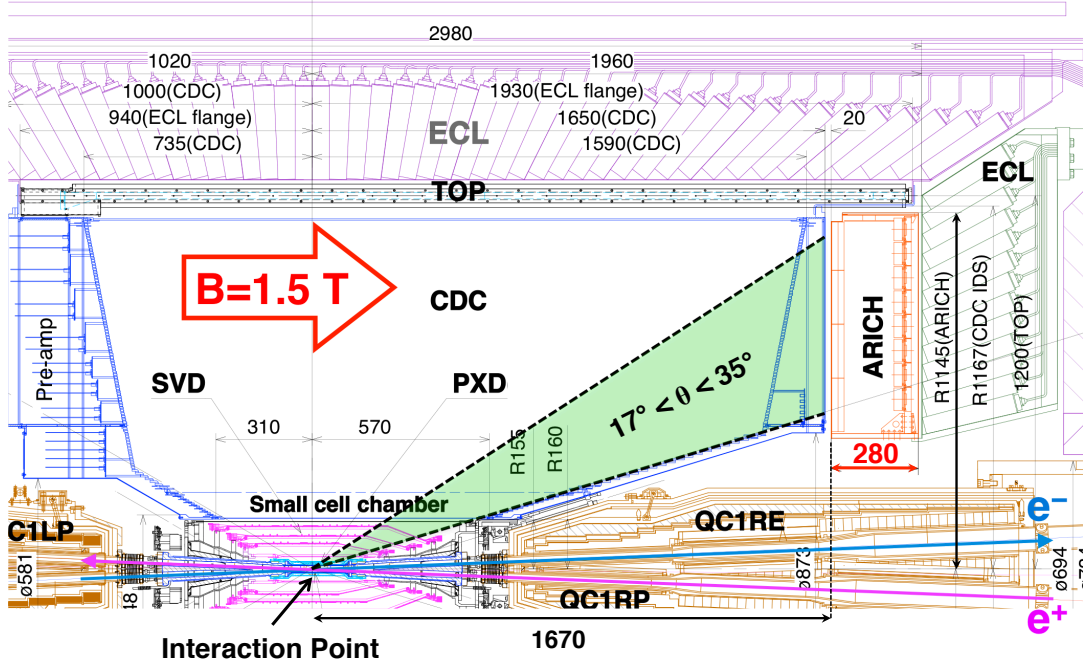


Figure 4.1: Horizontal cross-section of the Belle II detector. The ARICH counter will be installed in the forward end-cap region corresponding to the polar angle range  $17^\circ < \theta < 35^\circ$  from the interaction point (IP). Only 280 mm along the beam pipe direction is available for the ARICH counter, and a high magnetic field of 1.5 T exists in this region.

## 4.2 Photon detector

The photon detector used for the Belle II ARICH counter is required to have the following criteria:

- The ARICH counter is placed in the magnetic field  $B = 1.5 \text{ T}$  along the beam direction (see Fig. 4.1). Thus apparatuses used in the ARICH counter should be immune in this high magnetic field.
- At the maximum value of the target momentum range ( $p = 4 \text{ GeV}/c$ ), the Cherenkov angle difference between a pion and a kaon is  $\Delta\theta_C(K/\pi) = 23 \text{ mrad}$  with a radiator refractive index of 1.05. It corresponds to the difference of ring image radius of  $\Delta r \sim 5 \text{ mm}$ . Thus the pixel size of the photon detector is required to be less than 5 mm which is equivalent to a spacial resolution of  $5/\sqrt{12} \text{ mm}$ .
- Radiation damages is one of big concerns in the end-cap region of the Belle II detector. Main radiation sources are neutrons and  $\gamma$ -rays. The radiation hardness for these particles is required throughout the 10-year Belle II operation.

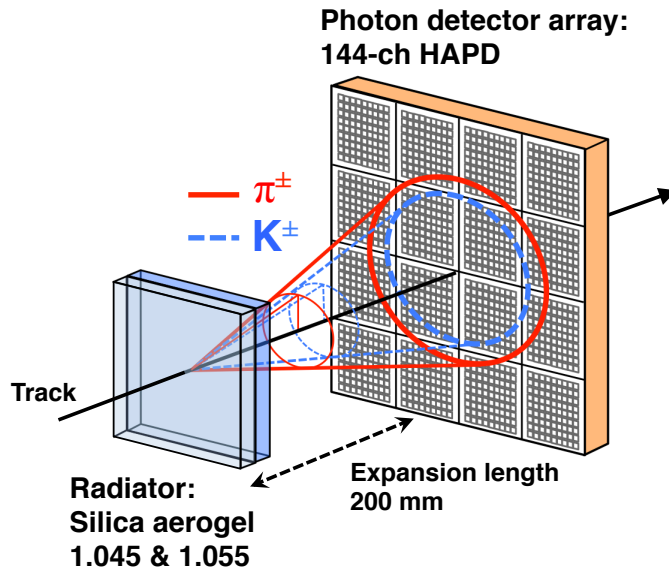


Figure 4.2: The conceptual design of the ARICH counter. The dual silica aerogel layer as the radiator and the 144-ch Hybrid Avalanche Photo Detectors as the photon detector will be used for this counter.

Although several candidates, which were used for in high energy physics experiments, are available as the photon detector of the ARICH counter, the 144-ch multi-anode Hybrid Avalanche Photo-detector (HAPD) was adopted. Several candidates of the photon detector for the ARICH counter are introduced and the reason why we adopt the HAPD are described in the following subsections.

#### 4.2.1 Photo multiplier tube (PMT)

The conventional PMT is one of the useful photon detectors for high energy physics, nuclear physics, and astro-physics experiments. The typical PMT has about 20 dynodes. By applying high electric potential about 2 kV in total, finally  $10^{6-7}$  electrons can be obtained for single photon from a PMT. Due to a dynode structure and an internal electric field, a PMT generally can not be used in a magnetic field, because amplified electrons in dynodes are affected by the Lorentz force  $\vec{F} \sim \vec{E} + \vec{v} \times \vec{B}$ , where  $\vec{v}$  is a photoelectron velocity and  $\vec{E}$  and  $\vec{B}$  are electric and magnetic fields, respectively.

As the photon detector of Aerogel Cherenkov counter (ACC) at the Belle experiment, fine-mesh photo-multiplier tubes (FM-PMTs), which can be used operative under a magnetic field of 1.5 T, was developed [39]. Because the FM-PMT consists with fine-mesh type dynodes placed perpendicular to the phototube axis, so that the electric field is almost parallel to the phototube axis. Thus the FM-PMT can be operated in the magnetic field that is parallel to the electric field direction in the FM-PMT.

Three different entrance window sizes of 2", 2.5", and 3" depending on a installed place for the Belle ACC, were used. But the same FM-PMTs are not suitable as the ARICH photon detector because sensitive area of the FM-PMT is too large to get position

resolution of less than 5 mm.

A gain of the FM-PMT has a large fluctuation in the amplification process, hence it is very difficult to clearly separate a single photo electron from noise. This means FM-PMTs are not suitable for single photon counting, which is vital for RICH photon detectors.

#### 4.2.2 Micro Channel Plate PMT (MCP-PMT)

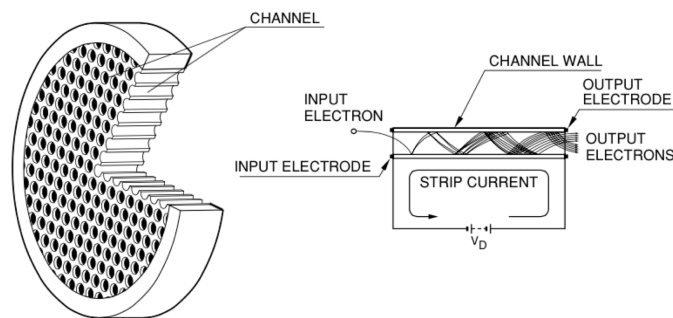
A Micro Channel Plate (MCP) is the resistive disk that contain a lot of capillaries with an inner diameter of  $\leq 20 \mu\text{m}$ . Fig. 4.3 [54] shows the structure and the schematic of amplification principle of an MCP. One capillary corresponds to a channel. Applying high voltage between both ends of the MCP, injected electrons are accelerated and bombarded on to a inner wall of a channel. Then secondary electrons are emitted, and this process is repeated a few times inside of a capillary channel. Finally about  $10^4$  electrons are obtained from a channel.

The MCP-PMT is a phototube, which contains with (usually) two MCPs. An MCP-PMT have a multi anode array to collect electrons, which can perform as a two-dimensional photon detector.

Due to the smaller diameter capillary, the drift length of an electron in a channel should be reduce hence the spread of drift time can be suppressed. Therefore MCP-PMT has a good time resolution, typical MCP-PMT achieves the time resolution of  $\sim 30$  ps.

Because each channel is separated by the resistive wall, electrons are amplified and are collected by an anode without any losses in a magnetic field. Therefore an MCP-PMT is a good candidate for photon detector used in a magnetic field.

But due to the small entrance of a capillary, the electron collection efficiency of the MCP-PMT is not so high ( $\sim 60\%$ ). Since photon loss should be made as little as possible for a RICH counter, it become a disadvantage for using MCP-PMT as the photon detector of a RICH counter.



THBV3\_1001EA

Figure 4.3: The schematics of the structure of a micro channel plate (MCP) [54]. Left: overview of the MCP. Right: the principle of the electron amplification in an MCP channel hole.

### 4.2.3 Multi Pixel Photon Counter (MPPC)

The MPPC is one of the silicon semi-conductor detector, and it consists of the pixelated avalanche photo-diodes operating in a Geiger mode. This device is also so called as SiPM (Silicon Photo-Multiplier). The typical MPPC pixel pitch is about  $50\ \mu\text{m}$  and the sensitive area is about  $1 \times 1\ \text{mm}^2$ . The MPPC contains with about  $10^{4-5}$  pixels. Recently the MPPC with the larger sensitive area ( $\lesssim 5 \times 5\ \text{mm}$ ) is commercially available.

Due to a Geiger mode operation in each pixel, it is regarded that the number of injection photons is equal to the number of photon detected pixels, when the number of injection photons are very few. Therefore the MPPC is a good photon counting device.

Although the MPPC is easy to operate because the applying voltage is typically around  $50\ \text{V}$ , the applying bias voltage to MPPC pixels depends on a temperature, and the dark count rate of the MPPC is very high (about  $> 100\ \text{kHz}$  for a typical MPPC). The dark count is also depending on a temperature. In order to operate the MPPC stably, the temperature controlling and the the correction to the bias voltage are necessary.

The size of a sensitive area is small then its cost is inexpensive, however MPPCs have to be used about  $10^{4-5}$  modules to cover the ARICH acceptance ( $\sim 3.5\ \text{m}^2$ ).

### 4.2.4 Hybrid Photo Detector (HPD)

The photon counting device, which is called as Hybrid Photo Detector (HPD), uses the combination of two amplification step. Fig. 4.4 [54] shows the schematic view of an HPD structure. This detector contains a semi-conductor photo-sensor in a vacuum tube. As the photo sensor, an avalanche photo-diode (APD) is used.

In the first step, the photoelectrons are accelerated using a high electric field by applying HV of about  $7\ \text{kV}$  between the photo-cathode and the APD chip in vacuum. Accelerated photoelectrons are bombarded onto the inner APD and electron-hole ( $e^-h^+$ ) pairs are generated. This process produces about  $1,100\ e^-h^+$  pairs in the APD dependent on the incident energy of a photoelectron. This amplification gain is called as **electron bombardment gain**. The bombardment gain is approximately proportional to the applying electric potential difference.

In the second step, the **avalanche amplification** occurs in the APD. An electron produced at the bombardment creates around  $50\ e^-h^+$  pairs in the high field region of the APD with an inverse bias voltage of around  $300\ \text{V}$ . As the result, the total gain will be approximately  $55,000$ .

The comparisons of main difference between an HPD and typical PMT are listed as follows [54]:

- The pulse height resolution of an HPD is extremely good compared to that of a PMT. Since the amplification process of HPD has little fluctuation, it has excellent pulse height resolution. One can separate a pulse height distribution by 1 to around 5 photoelectrons.
- Time response is faster than a PMT. An HPD has no dynodes, then photoelectrons are directly bombarded onto the APD.
- The total gain of a HPD ( $\sim \mathcal{O}(10^5)$ ) is lower than a PMT ( $\sim \mathcal{O}(10^{6-7})$ ). Thus the HPD should be used together with a high-gain and a low-noise amplifier.

- In an HPD, most photoelectrons from the photo-cathode strike the internal APD by high bombardment voltage.

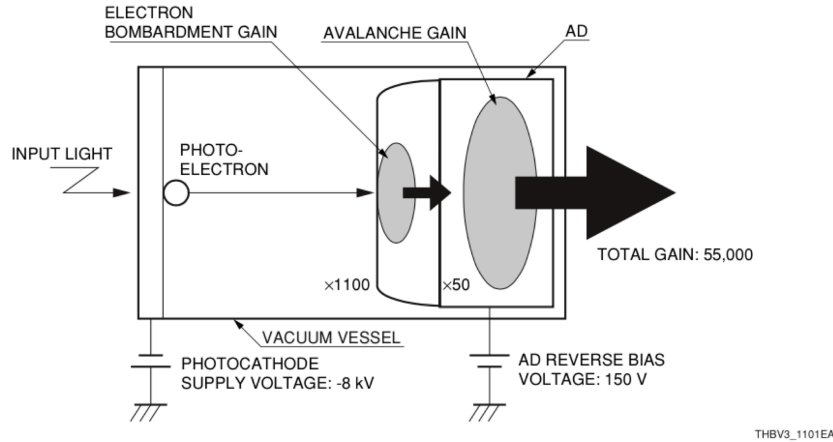


Figure 4.4: The schematics of the structure of a Hybrid Photo detector (HPD) [54].

To satisfy conditions to be installed for the Belle II end-cap region and achieve performances of a photon detector for a RICH counter, 144-ch multi-anode type Hybrid Avalanche Photo Detector (HAPD) had been chosen. This modules were developed and studied by the ARICH development group cooperating with Hamamatsu Photonics K.K. since 2002. The 420 HAPDs will be installed in the ARICH counter. MCP-PMT (Photons BURLE model 85112, two MCPs with  $10\ \mu\text{m}$ ,  $8 \times 8 = 64$  anode pads at 6.5 mm) was studied as the back-up option of the ARICH counter.

Details about the studies of the HAPD, in particular improvement of the radiation hardness, will be described in the chapter 5.

### 4.3 Radiator

Due to spacial limitation for the ARICH counter volume, the radius of a Cherenkov ring produced by the particle with  $\beta = 1$  is expected to be around  $\leq 60\ \text{mm}$ . As shown in Fig.4.1, the expansion length is available only about 200 mm, which is the remaining space after the subtraction of the space reserved for radiator layer, photon detectors, and related equipments. Since gaseous radiator with too low refractive index close to air ( $n \sim 1.00$ ) requires the long expansion volume of about 2 m, and the number of produced Cherenkov photons should be few. Therefore the gaseous radiator is not suitable for the proximity focusing type RICH system.

Since the liquid and quartz radiator have the higher refractive index  $n > 1.3$ , it is expected that the particle with  $\beta \sim 1$  has large emission angle. In the proximity focusing RICH system, a Cherenkov photon with large emission angle can not go outside of the radiator due to the total internal reflection in the radiator: When a charged particle enters the radiator with right angle and produces Cherenkov photons with a emission angle  $\theta_C$ , the produced Cherenkov photons should be totally reflected on the inner radiator surface.

The refracting angle is obtained by using the Snell's law:

$$n_2 \sin \theta_2 = n_1 \sin \theta_1, \quad (4.1)$$

where indices 1 or 2 indicate the material with different refractive index  $n_1$  or  $n_2$ , and  $\theta_1$  and  $\theta_2$  are the refracting angle in each materials. By the Eq.(4.1), the critical angle  $\theta_c$  between the radiator with the refractive index  $n$  and air ( $n_{\text{air}} \approx 1.0$ ) is estimated to be  $n \sin \theta_c = n_{\text{air}} \sin \pi/2 \sim 1$ . When a Cherenkov light, which has the emission angle  $\theta_C$  given by the Eq.(3.4), is totally reflected in the radiator ( $\theta_C = \theta_c$ ), the following relation is obtained:

$$\sin^2 \theta_c + \cos^2 \theta_c \sim \left(\frac{1}{n}\right)^2 + \left(\frac{1}{n\beta}\right)^2 = 1.$$

Here, it is assumed that incident charged particle have  $\beta = 1$ , then the critical refractive index  $n_c$  is estimated by  $1/n_c^2 + 1/n_c^2 = 2/n_c^2 = 1$ , to be  $n_c = \sqrt{2} \sim 1.41$ . As the result, the solid radiator with higher refractive index ( $n > 1.4$ ) such as a silica quartz ( $n = 1.46$ ) can not be used for the proximity focusing type RICH system.

Liquid radiators, which have refractive index around 1.33 or more, do not totally reflect Cherenkov light. The emission angle from the radiator to the expansion space however is too large to measure the radius of a Cherenkov ring. Therefore liquid radiators are not suitable for the proximity focusing type RICH system either.

As the result, a silica aerogel radiator was remained as a unique material for the ARICH counter.

### 4.3.1 Choice of the refractive index

Refractive index of silica aerogel can be adjusted in the range of 1.004 to 1.10. To avoid the loss of the number of Cherenkov photoelectrons  $N_{\text{pe}}$ , high transmission length is necessary. Fig.4.5 [36] shows dependence of the transmission length on the refractive indices. Three kinds of marker are indicated according to the solvent material used for the alcogel synthesis; triangles (green) and circles (red) are ethanol and methanol, which are traditional solvents, respectively. Open squares (blue) are DMF<sup>1</sup> which was introduced to obtain silica aerogels with higher transparency [36]. In general, the transmission length decreases in proportion to the refractive index, and the highest transmission length is obtained at around 1.03 to 1.05. In addition, since the number of Cherenkov photons, which were produced in the radiator with the refractive index  $n$ , is proportional to  $\sin^2 \theta_C = 1 - 1/(n\beta)^2$ , the radiator having the high refractive index can produce more Cherenkov photons. Therefore the ARICH counter was designed to use the silica aerogel with refractive index of 1.05 to have high transmission length and obtain the sufficient quantity of photoelectrons.

Furthermore, the method to produce a large size ( $180 \times 180 \times 20 \text{ mm}^3$ ) hydrophobic aerogel with high transparency was established [36, 55].

---

<sup>1</sup>*N,N*-dimethylformamide [ $\text{HCON}(\text{CH}_3)_2$ ]

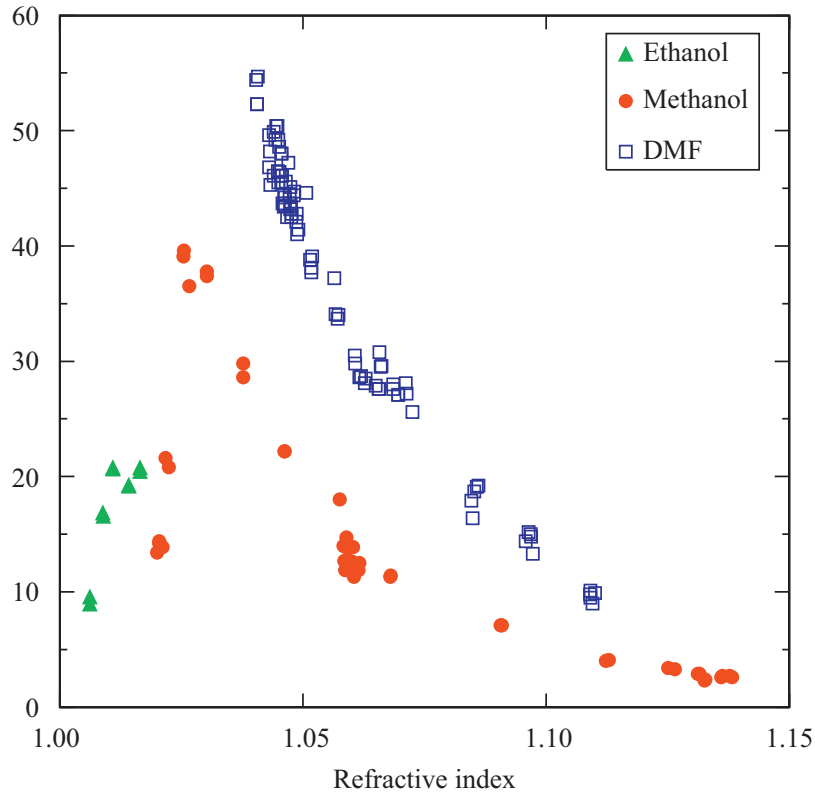


Figure 4.5: Transmission length as a function of the refractive indices at 400 nm of injected photons [36]. Markers are corresponding to kinds of a solvent used for synthesizing of alcogel with an ethanol (triangles), a methanol (circles), and DMF (squares), respectively.

### 4.3.2 Thickness of a radiator

The Cherenkov angle resolution of a track  $\sigma_{\theta}^{\text{trk}} \equiv \sigma_{\theta} / \sqrt{N_{\text{pe}}}$  is the crucial parameter to determine the ARICH performance. Fig. 4.7 (a) shows the Cherenkov photon trajectories in the typical proximity focusing type RICH system. The contribution of the radiator thickness  $d$  to  $\sigma_{\theta}^{\text{trk}}$  is proportional to  $d / \sqrt{N_{\text{pe}}}$ . If the absorption length is large enough compared with  $d$ , the number of detected photons increases linearly with the thickness and  $\sigma_{\theta}^{\text{trk}}$  becomes proportional to  $\sqrt{d}$ . The thinner aerogel can reduce  $\sigma_{\theta}$  due to the decreased ambiguity of the emission point of a Cherenkov photon, although the detected photons will be decreased. It was verified that an optimal thickness of the aerogel for the ARICH counter should be around 20 mm [56, 57].

### 4.3.3 Dual radiator focusing

In order to increase the number of detected photons without degrading the resolution, the dual layer focusing scheme was introduced [57]. Fig. 4.7 (b)) shows the proximity focusing RICH system with the dual radiators. The dual layer focusing RICH counter consists of two aerogel tiles with different refractive indices attached each other.

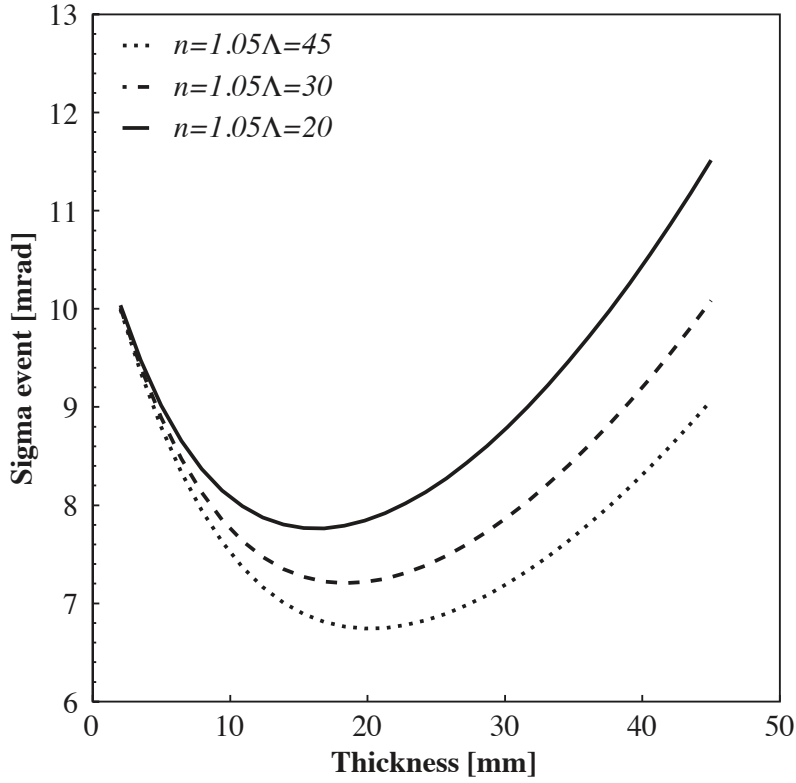


Figure 4.6: The estimated Cherenkov angle resolution a track  $\sigma_\theta/\sqrt{N_{pe}}$  as a function of the aerogel tile thickness [57]. These plots are corresponded to three different transmission length  $\Lambda$  at 400 nm,  $\Lambda = 20$  mm is a solid line, 30 mm is a dashed line, and 45 mm is a dotted line, respectively.

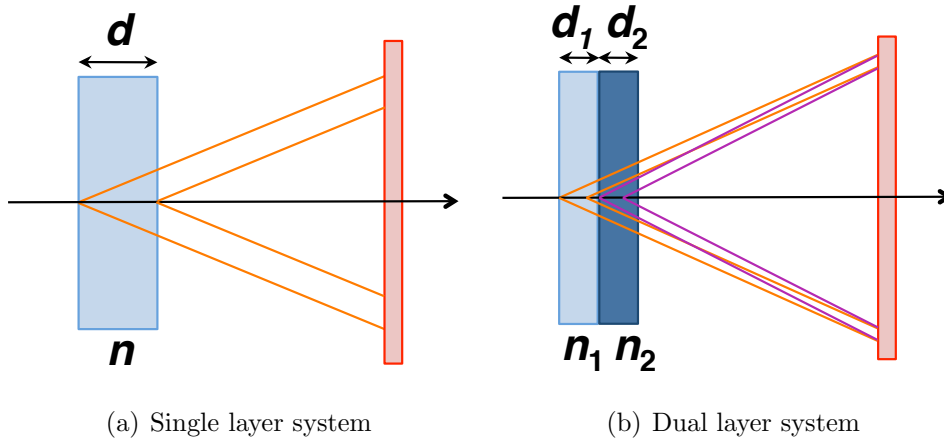


Figure 4.7: Schematics of proximity focusing schemes; (a) Normal type proximity focusing system with a single-layer radiator, (b) Proximity focusing system with dual layer focusing, which consists with different refractive indices of  $n_1$  and  $n_2$  ( $n_1 < n_2$ ) are used. The total thickness of aerogels  $d$  in both systems are the same.

By adjusting the refractive index of the downstream aerogel  $n_2$  to be slightly higher than that of the upstream aerogel  $n_1$ , the Cherenkov angle in the downstream aerogel becomes slightly larger than that of the upstream aerogel. As the result, the Cherenkov photons from the two aerogel tiles are focused on the surface of the photon detector array.

When the total thickness of two radiators is equal to that of single layer system ( $d = d_1 + d_2$ ), it is expected that the  $N_{pe}$  by the dual layer focusing RICH counter is approximately equal to the  $N_{pe}$  by the single layer focusing RICH counter. But due to the focusing of the Cherenkov ring by the downstream aerogel on the photon detector surface, the Cherenkov angle resolution  $\sigma_\theta$  using the dual layer focusing can be improved comparing with the single layer focusing system.

As the discussion in the previous subsection, the ARICH counter requires the aerogel radiator with the refractive index of around 1.05. For dual radiator focusing scheme, combination of the refractive indices of  $n_1 = 1.045$  and  $n_2 = 1.055$  was adopted [57].

## 4.4 Structure design

In light of the above discussion, the ARICH counter for the Belle II detector was design as follows:

- The dual layered silica aerogels, with refractive indices of  $n_1 = 1.045$  and  $n_2 = 1.055$  for the upstream and downstream aerogel, respectively.
- The thickness of both aerogel tiles is 20 mm, and the expansion region between the upstream end of the first aerogel and the surface of the photon detector is 200 mm.
- The 420 HAPDs are used as the photon detector.

The ARICH container consists of two cylinders inner and outer radii of 420 mm and 1140 mm, respectively. Fig. 4.8 shows designed drawing of the ARICH counter. The left figure corresponds to the X–Y plane, which is perpendicular to the beam pipe direction, and it is divided by four parts; the front view of the HAPD arrangement (top left), the backward of the HAPD fixed plate (top right), the aerogel tiling (bottom left), and the end-plate of the ARICH counter (bottom right), respectively. To collect Cherenkov photons emitted to the out of polar angle acceptance ( $> 35^\circ$ ) of the ARICH, the 18 planar mirrors are installed on the outer wall.

The main parameters of the ARICH structure are summarized in Table 4.1.

Table 4.1: The summary of the ARICH mechanical structure

Dimensions	Inner radius	420 mm
	Outer radius	1140 mm
	Depth	280 mm
Material	Aluminum	
Estimated wight	Support structure	122 kg
	Aerogel tiles with container	25 kg
	HAPD modules and cables	203 kg
	Outer reflection mirrors	7 kg
	Total weight	357 kg



## 4.5 Readout electronics

Due to the space limitation, the readout electronics and other related equipments are required to be installed within 50 mm along the beam axis direction.

### Readout ASIC

The readout electronics of the HAPD used for the ARICH counter are required to have high-gain and a low-noise amplifier so that it can discriminate the single photon signal from noise. Note that the charge information is used only for discrimination between single photons and noise; most of the Cherenkov photon hits are from single photons, and only the hit information (yes or no) is important.

In order to satisfy the spacial condition and the required performance, a custom ASIC chip, which is named SA03, was developed. The SA03 chip has 36 channels. Each channels have a charge-sensitive amplifier, waveform shaper, and discriminator. The SA03 chip is packaged with the LTCC package<sup>2</sup>, and the package size is  $1.3 \times 1.3$  cm.

Fig. 4.10 shows the SA03 main circuit diagram of a channel. The shaper has a variable shaping time that allows the readout electronics to cope with the increase of the noise level due to damage of an HAPD by the neutron radiation. The detail discussion of the radiation damage of a n HAPD will be described in the next section. The specifications of the SA03 chip are summarized in Table 4.2.

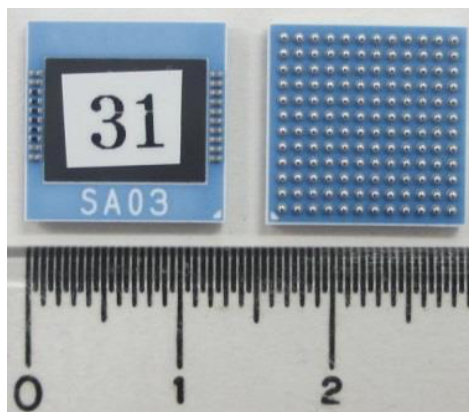


Figure 4.9: The picture of the ARICH readout ASIC (SA03): the front-side view (left) and the rear-side view (right).

### Front-end board

The front-end board, which is directly attached to the backplane of an HAPD, has four readout ASIC chips (Fig. 4.11 (a)) and an FPGA chip (Xilinx Spartan6) for readout control and communication to the higher levels of the readout system (Fig. 4.11 (b)). The other components on the front-end board are a bias voltage connector for the attached

<sup>2</sup>Low Temperature Co-fired Ceramics package

Table 4.2: SA03 specification

Production process	TSMC CMOS 0.35 $\mu\text{m}$
Baer chip size	$3.0 \times 6.5 \text{ mm}^2$
# of channels	36
Noise level (Design)	2,000 electrons at 80 pF
Operation voltage	$\pm 1.65 \text{ V}$

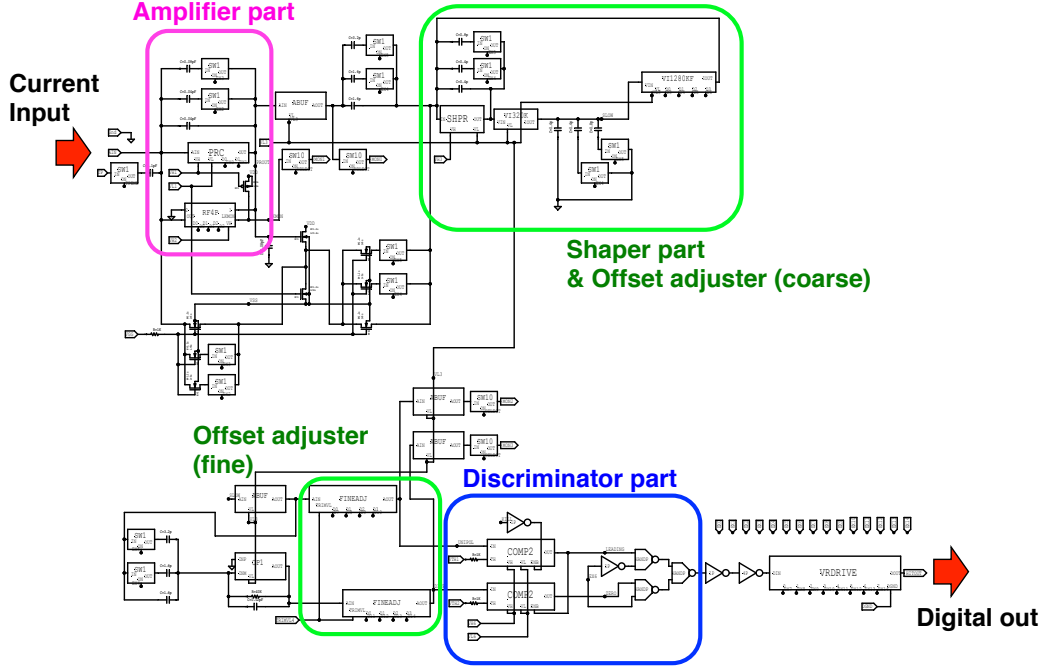


Figure 4.10: The block diagram of the SA03 main circuit of a channel.

HAPD and temperature sensor chips [58]. The size of the front-end board is designed to fit the HAPD.

In the ASIC the signal from the HAPD is amplified, shaped and discriminated to create hit information. The hit information from the ASIC is buffered in the FPGA and is sent to the merger system.

## Merger system

To merge the hit information from several front-end boards and to suppress the data size, the relaying system, which is named as merger board, is installed at the backplane of the ARICH container. Fig. 4.12 (a) shows the overview of the ARICH readout system through the front-end board and the merger board. A merger board collects data from five or six front-end boards, and unites them as single data series, with zero data suppressed. Finally, the merged data are sent to the Belle II central data acquisition (DAQ) system through an optical cable, named Belle2-link.

Fig. 4.12(b) shows the photograph of the merger board. An ARICH merger board consists of the following components:

- A programable FPGA chip (Xilinx Virtex5)
- Six front-end board connectors
- An optical interface for the Belle2-link
- Two LAN cable interface for receiving the trigger clock from the Belle II detector and the FPGA configuration signals
- Power supply connector

Since the 420 front-end board are used, the 72 merger board will be installed in the ARICH counter.

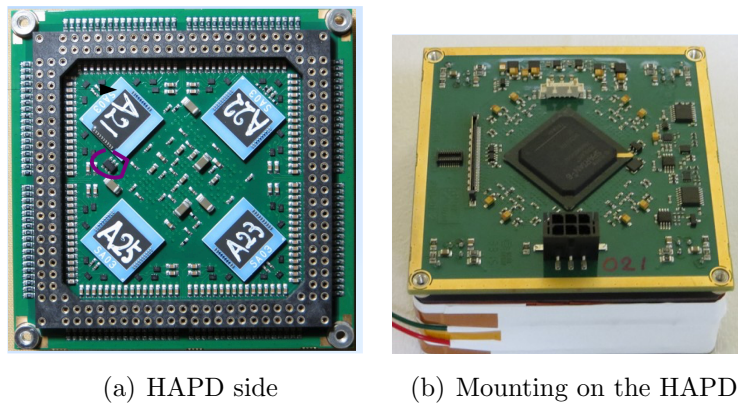


Figure 4.11: Pictures of the front-end board mounted on an HAPD.

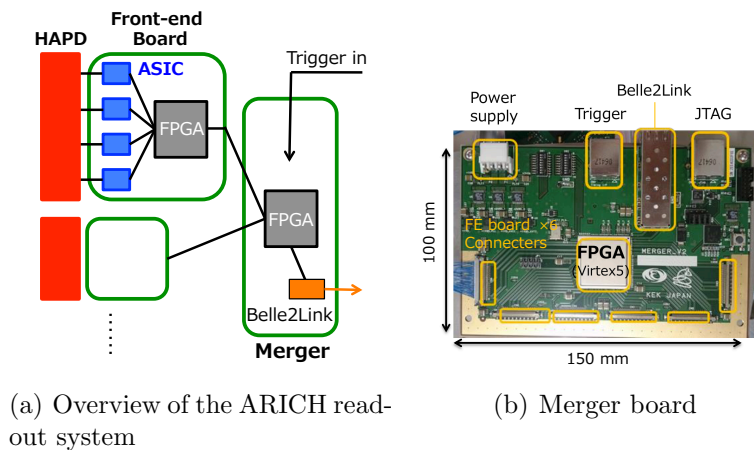


Figure 4.12: The schematic of the ARICH readout system (a) and the merger board (b).

# Chapter 5

## Development of the HAPD

In this chapter, the development of the 144-ch Hybrid Avalanche Photo Detector (HAPD) used for the ARICH counter is described. In particular, detail studies for the radiation hardness of HAPD modules is described.

### 5.1 Specifications

In the discussion in chapter 4, 144-ch HAPDs were decided to be used as the position sensitive photon detectors of the ARICH counter.

An HAPD is composed of a Bialkali photo-cathode, a vacuum tube, and four avalanche photo-diode (APD) chips. Each of the APD is divided into  $6 \times 6$  pixels, resulting in 144 channels. The schematics of the HAPD are shown in Fig. 5.1. Specifications of the HAPD module for dimensions, materials, and gains are summarized in Table 5.1.

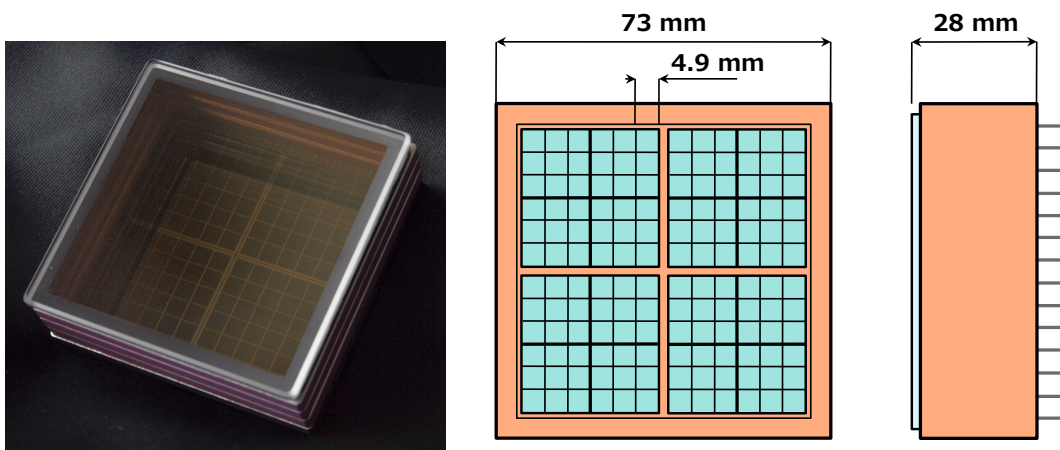


Figure 5.1: Picture of the exterior (left) and the design of the 144-ch HAPD (right).

Table 5.1: HAPD specification

# of pixels	$12 \times 12 = 144$ ch
Package size	$73 \times 73 \times 28$ mm <sup>3</sup>
Pixel size	$4.9 \times 4.9$ mm <sup>2</sup>
Effective area	65%
Capacitance	80 pF
-----	
Window material	Synthetic quartz
Window thickness	3 mm
photo-cathode material	Bialkali
Quantum efficiency	$\sim 28\%$ (average, at 400 nm)
-----	
Avalanche gain	$\sim 40$
Bombardment gain	$\sim 1650$ , at 7 kV
$S/N$	$\sim 15$

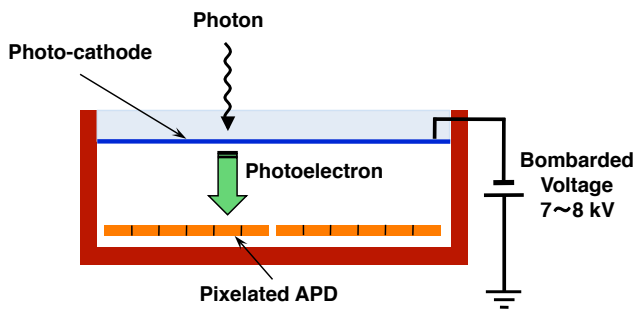
## 5.2 Basic performances

### 5.2.1 Detection of single photon

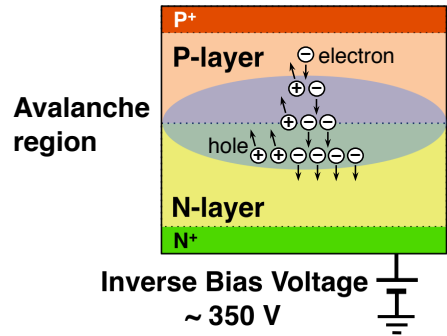
In an HAPD module, photoelectrons are amplified in two steps (Fig. 5.2). In the first step, photoelectrons are accelerated by a high electric field; after passing a potential difference of 7–8 kV in vacuum they hit APDs, and produce 1,600–1,800 electron–hole pairs (Fig. 5.2 (a)). This gain is known as an electron bombarded gain. In the second step, an avalanche amplification occurs in APDs. Thus generated electron produces around 40 electron–hole pairs in a high-field region of an APD with an inverse bias voltage of around 350 V (Fig. 5.2 (b)). This gain is known as an avalanche gain. As a result, a total gain becomes around  $7 \times 10^4$ .

Fig. 5.3 show the avalanche gain and the electron bombarded gain for a APD chip in the typical HAPD. In this sample, if the inverse bias voltage and the cathode voltage are applied to be 330 V and  $-7$  kV, which correspond to typical operational voltages, the avalanche gain  $G_{\text{Ava}}$  and the bombardment gain  $G_{\text{Bom}}$  are obtained to be 40 and 1,500, respectively. As the result, the total gain  $G$  is obtained as  $G = G_{\text{Ava}} \times G_{\text{Bom}} = 60,000$ .

Because the bombardment gain ( $\sim \mathcal{O}(10^3)$ ) is larger than the avalanche gain, the statistical fluctuation in the output signal can be suppressed; this effect is further enhanced using the Fano factor in silicon. Therefore, HAPDs have excellent performance in single photoelectron separation. Fig. 5.4 shows a pulse height distribution obtained by an HAPD sample with multiple photons produced using a blue LED. We fit this distribution with a sum of three Gaussians for the three peaks, corresponding to the noise, single photoelectrons (1 p.e.), and two photoelectrons (2 p.e.), and a second-order polynomial function. From the difference of the mean values between 1 p.e. and 2 p.e., the signal gain of 1 p.e. was calculated to be about 46,000. The noise equivalent to number of electrons was calculated as about 2,000 from the width ( $1\sigma$ ) of the leftmost Gaussian. We have



(a) A cross-sectional view of the HAPD



(b) A illustration of the structure of an APD

Figure 5.2: Illustrations of the HAPD and the structure of an APD. There are two mechanisms of electron amplification. These include bombarded gain due to the electric field (a), and avalanche gain in the APD (b).

therefore obtained a signal-to-noise ratio  $S/N$  of about 23, which is sufficient for reliable single photon detection in the ARICH counter.

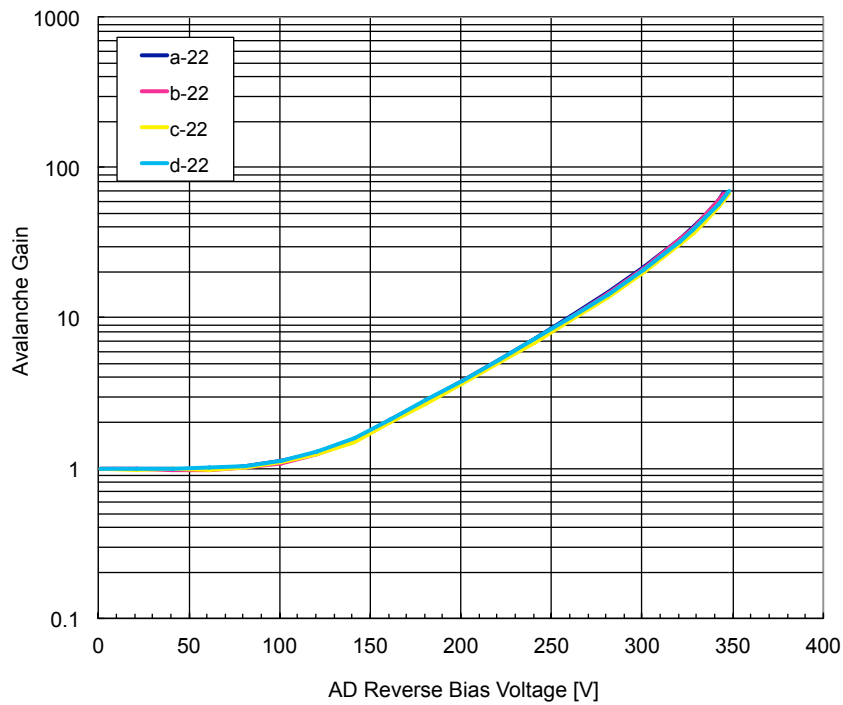
## 5.2.2 Detection efficiencies

The HAPD used for the ARICH counter has the bi-alkali photo-cathode [54]. Fig. 5.5 shows the quantum efficiency (QE) of the bi-alkali photo-cathode as a function of wavelength of the injected light. In this sample, we found that the value of QE is over 30% at around 400 nm which corresponds to the wavelength of the typical Cherenkov light.

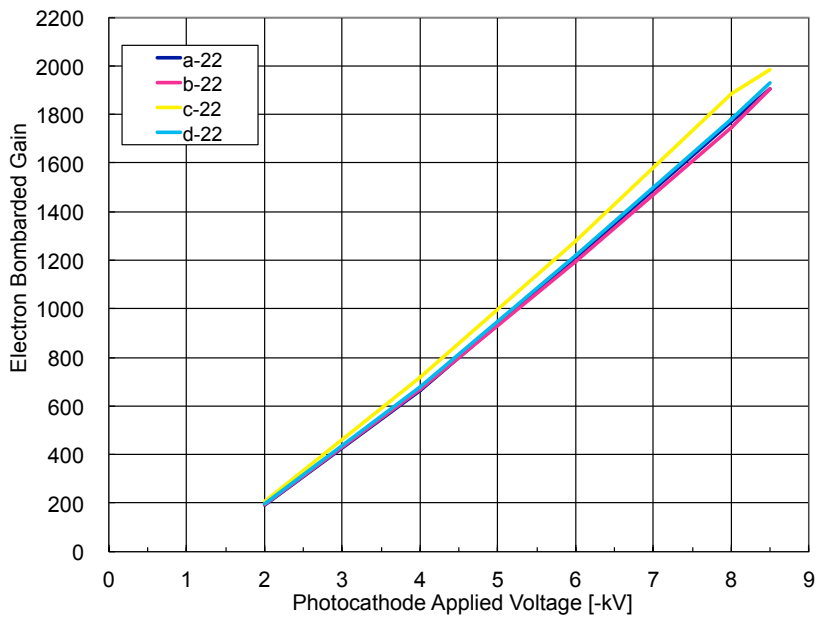
Fig. 5.6 shows the two-dimensional hit map, where the horizontal and vertical axis corresponds to injection position of the pulse laser. Colors of each point indicate the detection efficiency of pulse laser light. As the result, we found that the detection efficiency of the HAPD is sufficiently uniform over the sensitive area. A blue box at  $x = 22$  mm and  $y = 60$  mm of this figure corresponds to a dead channel of the readout electronics. The shape distortion of outermost channels of the HAPD can be explained as distortion of the electric field in the vacuum tube of the HAPD. The effect is expected to be improved during operation of the HAPD under a high magnetic field, and is described in the next subsection.

## 5.2.3 Operation in a magnetic field

In the Belle II detector, high magnetic field of 1.5 T is applied at the central part of the detector along the beam direction to measure momenta of charged particles. An electric field in an HAPD is applied to be parallel to the vacuum tube of an HAPD and thus perpendicular to contained APD chips. But the electric field at the inner edge near the wall and photo-cathode of the HAPD, is distorted as shown in Fig. 5.7. Due to this deformation of the electric field in edge part of an HAPD, photoelectrons produced near the edge of the HAPD, can not travel along the direction of the tube, and the hit position onto an APD chip is displaced. If an HAPD is placed in the magnetic field that is parallel



(a) Avalanche gain



(b) Bombardment gain

Figure 5.3: The avalanche gain and the bombardment gain of a recent HAPD sample. (a) Avalanche gain as a function of the applying inverse bias voltage. (b) Electron bombarded gain as a function of the bombardment voltage applying in photo-cathode.

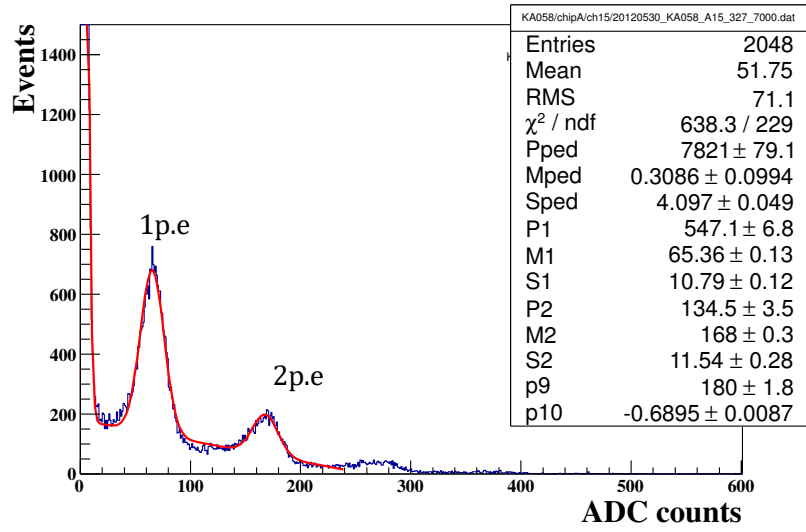


Figure 5.4: The pulse height distribution for low intensity pulsed LED illumination.

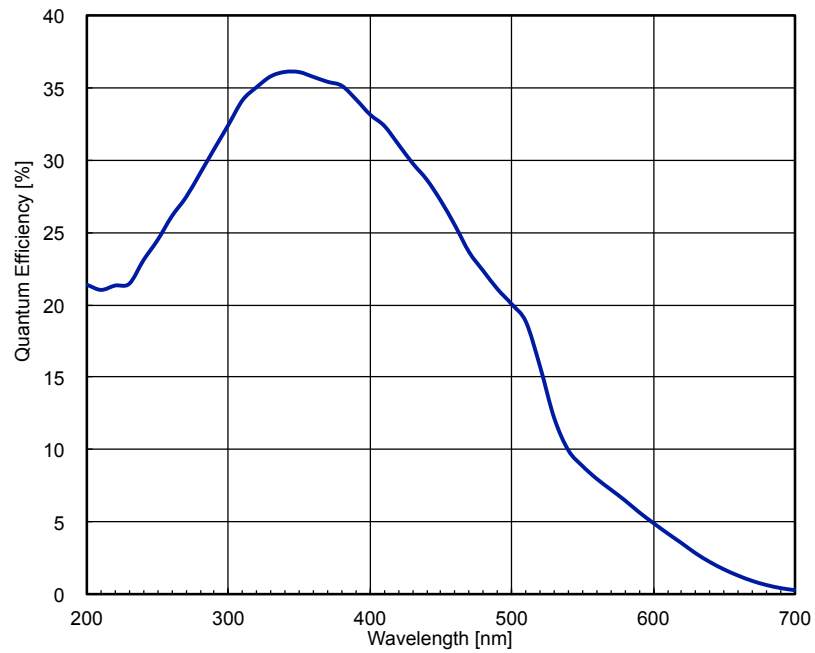


Figure 5.5: The quantum efficiency of the photo-cathode as a function of the wavelength of injected light.

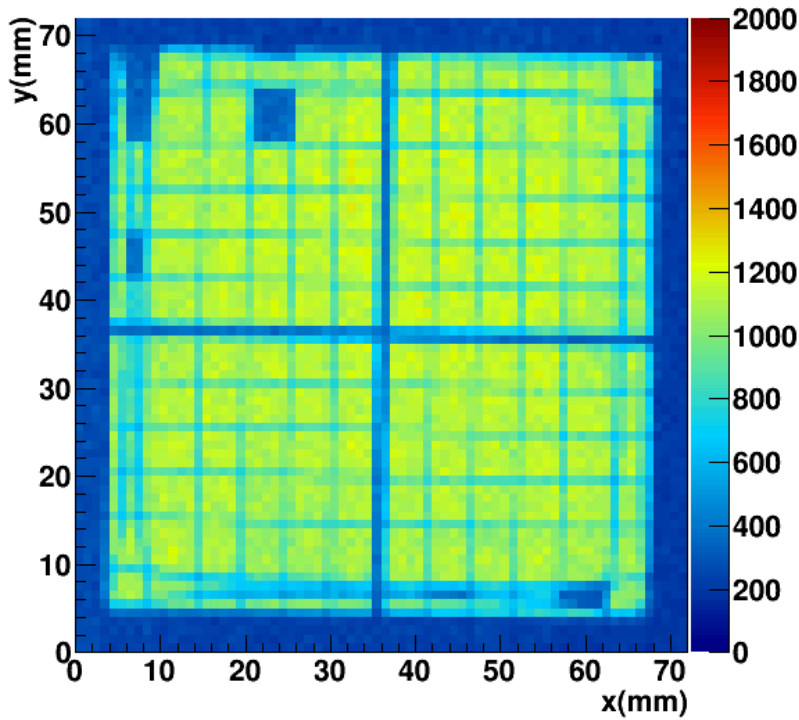


Figure 5.6: The two-dimensional hit map by injecting laser positions. Colors of each point indicate the detection frequency of pulse laser light.

to the tube, photoelectrons travel along the exterior magnetic field line and can hit onto the correct position of the APD. Photoelectron trajectory becomes helix orbit with a Larmor radius  $r_L$  along a magnetic field line, but the  $r_L$  in a high magnetic field of 1.5 T should be about  $1\ \mu\text{m}$  or less, then this effect is almost negligible. Therefore, the full effective area of the HAPD in a magnetic field can be available.

The other issue is the back-scattering on the APD surface. Some photoelectrons are reflected on the APD surface and are occasionally collected by neighboring APD pixels. Fig. 5.8(a) shows the photoelectron hit map for a APD pixel without a magnetic field, where the horizontal and vertical axis corresponds to the LED light injection position. This data is taken by two-dimensionally moving the LED to scan whole AHPD region and taking data from only one APD pixel. The small squared-like area seen in the bottom-left corresponds to the measured APD pixel, other hit signals are mainly made by back-scattering photoelectrons. At this condition without magnetic field, the back-scattering hits are measured up to 35 mm from the LED light position. On the other hand, if an HAPD is placed in parallel to a magnetic field, this spread of back-scattering hits can be suppressed. When the HAPD was operated in a magnetic field of 1.5 T, the two-dimensional hit map was obtained as shown in Fig. 5.8(b). the back-scattering radius is clearly decreased and is measured to be 15 mm.

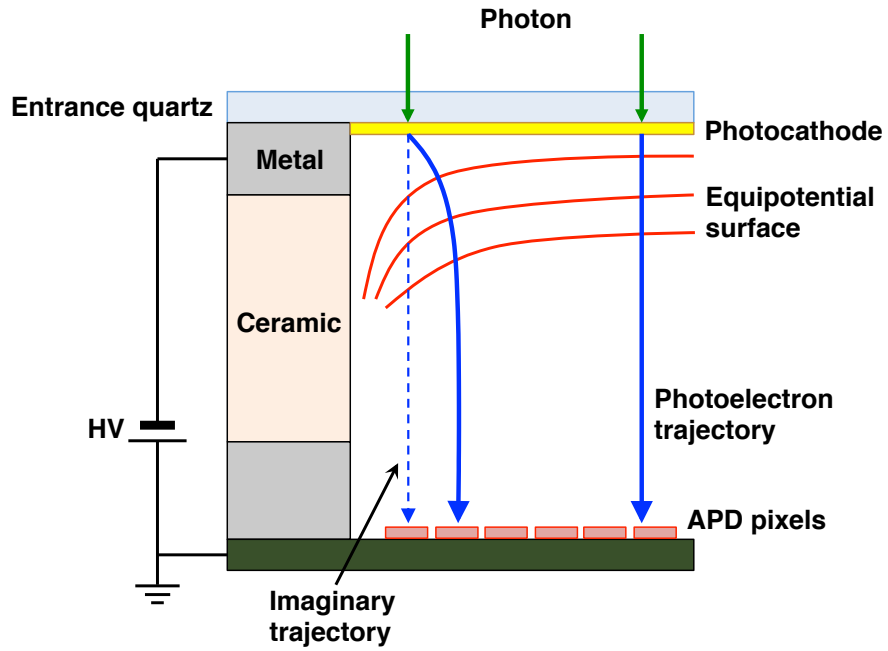


Figure 5.7: The schematic of the electric field formation near the top edge of an HAPD vacuum tube .

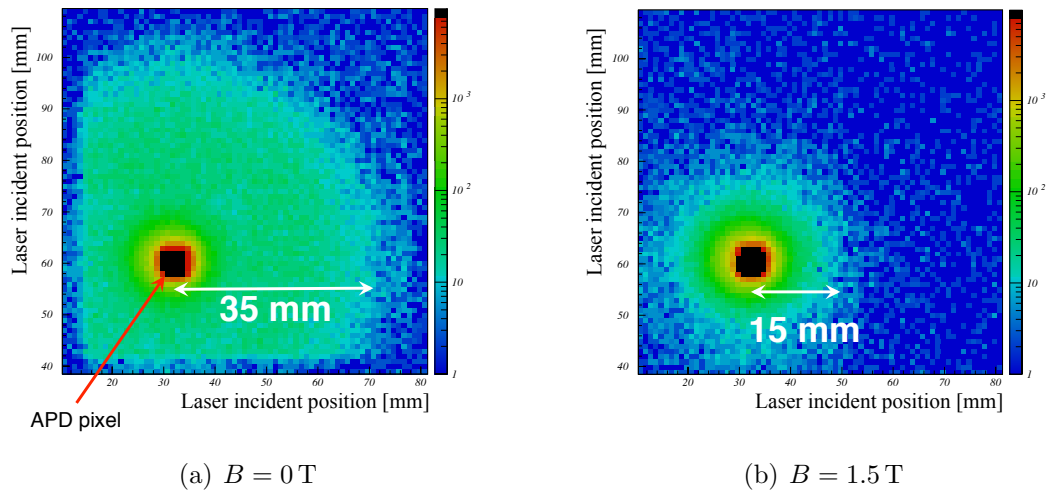


Figure 5.8: Two-dimensional the light injection positions by photoelectron signals in a corresponding to APD pixel in the no magnetic field (a), and  $B = 1.5$  T (b), respectively [59].

## 5.3 Radiation hardness of HAPD and its improvement

Besides the various mechanical and electrical constraints, the HAPD is also required to have sufficient radiation tolerance for 10-year Belle II operation. In the front of the end-cap region of Belle II, a one MeV-equivalent neutron fluence of  $1 \times 10^{12} \text{ cm}^{-2}$  and a  $\gamma$ -ray dose of up to approximately 100 Gy are expected in total for 10-year operation.

### 5.3.1 Neutrons

Neutrons induce lattice defects in the bulk region of an APD. This results in an increase of the leakage current through this region. We found that a shot noise from the HAPD also increases and causes a degradation of  $S/N$  in the single photon detection. We had performed several irradiation tests to investigate the source of shot noise. As the result, we confirmed that the leakage current from the P-layer is larger than that from the N-layer because the electrons from the P-layer get amplified in the avalanche region, while the amplification for holes from the N-layer is negligible (Fig. 5.2 (b)). The leakage current can, therefore, be efficiently reduced with making a P-layer thinner, and this solution to suppress the noise increase due to bulk damage, was implemented in the final design of the APD.

The noise can also be suppressed by having a shorter shaping time in the front-end electronics. The main components of the noise for each channel of the HAPD are the shot noise and amplification noise. We assume that the shot noise and amplification noise are proportional to  $\sqrt{I_{\text{leak}}G\tau} \sim \sqrt{\tau}$  and  $1/\sqrt{\tau}$ , respectively. Here,  $I_{\text{leak}}$  is the leakage current from one channel,  $G$  is the avalanche gain, and  $\tau$  is the shaping time of a readout system.

Because the shot noise is proportional to  $\sqrt{\tau}$ , it can be suppressed by using a shorter shaping time. However, the total noise increases for very short shaping times, as the amplification noise is inversely proportional to  $\sqrt{\tau}$ . We have calculated the optimal shaping time to be 100 ns with  $G = 40$ . To cope with noise increase by neutrons, we developed a readout ASIC (SA03, see chapter 4.5) such that the shaping time can be varied between 100 ns and 200 ns.

### 5.3.2 $\gamma$ -rays

The  $\gamma$ -ray radiation causes charge up around the structure on the APD surface. In particular, we found that  $\gamma$ -rays easily charge up a protection film, which covers the APD in order to protect it from alkali materials that are evaporated during photo-cathode deposition. We then found that the breakdown voltage between the film and the structure around it was reduced as the  $\gamma$ -ray dose was increased. As a result, we found that the breakdown voltage got below the normal operational voltage, and the APD had to be operated at lower avalanche gain. Therefore, the surface part of the APD had to be redesigned to prevent the charge increase, while keeping sufficient protection from alkali materials.

### 5.3.3 Verification of improvements

In 2012, we performed a series of irradiation tests to confirm that the HAPD with an improved APD has a sufficient tolerance to both neutron and  $\gamma$ -ray irradiations expected at Belle II [60]. We performed the neutron irradiation test at the neutron beam line at J-PARC MLF (Ibaraki, Japan). The HAPDs having a thinner P-layer were irradiated with a fluence of up to  $0.86 \times 10^{12}$  neutrons/cm<sup>2</sup> (one MeV-equivalent).

Fig. 5.9 shows the result of the neutron irradiation test for the HAPD irradiated with  $0.86 \times 10^{12}$  neutrons/cm<sup>2</sup>. This plot compares the noise levels for shaping times of 100 ns and 250 ns. We confirmed that shaping time of 100 ns suppresses the noise induced by the neutron irradiation, and the noise levels for 100 ns is lower than that for 250 ns. The noise after neutron irradiation is expected to be around  $5,000 e^-$  with an avalanche gain of 40. Since the single photoelectron signal is estimated as  $1700 \times 40 = 68,000(e^-)$  with nominal operational bombarded voltage and inverse bias voltage, we estimate the  $S/N$  to be greater than 10. We found that the noise increase by neutron fluence the is acceptable for the ARICH counter. As a result, we conclude that the developed HAPD sensor that has a thinner P-layer, can separate single photoelectrons from noise even above the expected level of neutron irradiation for 10-year operation.

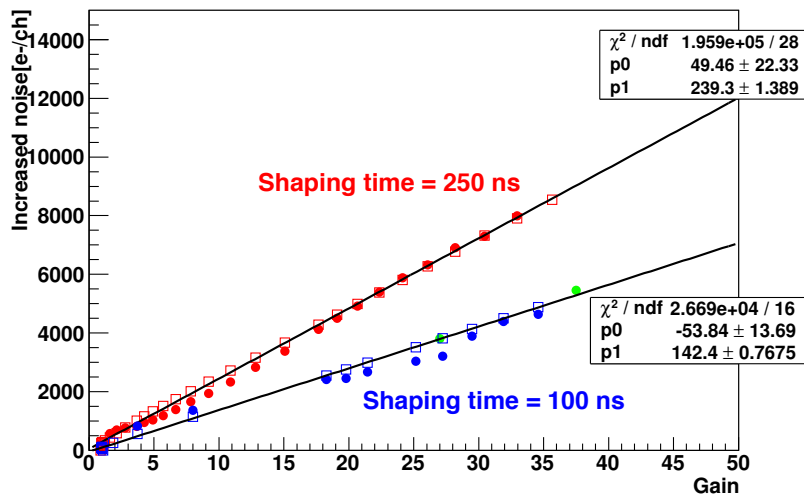


Figure 5.9: Results of the neutron irradiation test in 2012. The measured noise is plotted with filled symbols as a function of the effective avalanche gain corresponding to a reduced bias voltage due to the increased leakage current; the filled symbols correspond to measurements with 250 ns (red) and 100 ns (blue) after irradiation with neutrons corresponding to a fluence of  $0.86 \times 10^{12}$  cm<sup>-2</sup>. The open symbols correspond to estimated noise levels assuming the shot noise for 250 ns and 100 ns, and the noise expectations are fitted with the solid line.

After cooling the HAPDs for around three months from the neutron irradiation, a  $\gamma$ -ray irradiation test was performed at a <sup>60</sup>Co facility of Nagoya University in 2012 [60]. We irradiated the HAPDs up to 1,000 Gy and performed in-situ measurement of the leakage current during and after the irradiation. A comparison of the leakage current before and after the  $\gamma$ -ray irradiation is shown in Fig. 5.10.

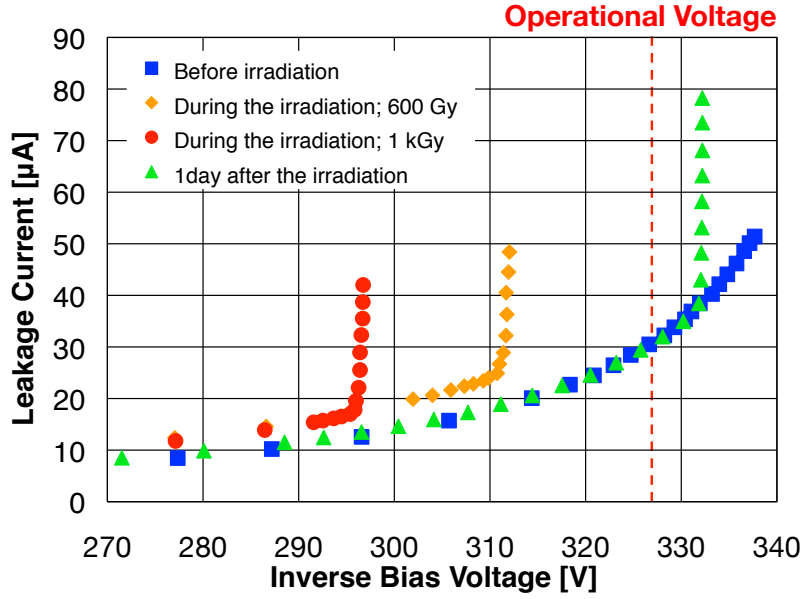


Figure 5.10: Comparison of leakage current before and after the irradiation: before the irradiation (blue square), after 600 Gy (orange rhombus), and 1,000 Gy (red circle), and on day after irradiation (green triangle). The operational voltage is indicated as vertical dash line corresponding to 327 V.

Right after the irradiation, the breakdown voltages for the APDs with  $\gamma$ -ray doses of 600 Gy and 1,000 Gy are found to be below the operational voltage of the APD (327 V, corresponding to an avalanche gain of 40). However, after a day of annealing at room temperature, the breakdown voltage was recovered to exceed the operational voltage. This indicates that the effect ascribed to the charge-up of the surface only happens if radiation dose exceed by several orders of magnitude larger than that expected in Belle II. In summary, we have confirmed that the HAPDs will be reliably operated up to the maximal expected neutron fluences and  $\gamma$ -ray doses and Belle II, and even beyond.

# Chapter 6

## Beam test using the prototype ARICH counter

In this chapter, studies of the prototype ARICH counter using electron beam are described. In order to confirm the basic performance of the ARICH counter using the developed components including a neutron and  $\gamma$ -ray irradiated HAPD, we constructed a prototype detector and have carried out a test at the electron beam line T24, at DESY.

### 6.1 Prototype ARICH counter

The prototype ARICH counter consists of six HAPD modules, two aerogel tiles, and six front-end boards. The configuration of aerogels and HAPDs that is used for this study, are listed in Table 6.1, and the HAPD layout is shown in Fig. 6.1 (a).

HAPD No.4 is used for the radiation hardness tests, irradiated with a neutron fluence of  $0.86 \times 10^{12} \text{ cm}^{-2}$  and with a  $\gamma$ -ray dose of 1,000 Gy (see chapter 5.3).

A set of two aerogels with  $n_1 = 1.0467$  and  $n_2 = 1.0592$ , which were chosen to focus Cherenkov photons at the HAPD surface, were mounted in front of the HAPD array. We mounted the aerogel layers with a distance of 200 mm from the upstream surface of the aerogel  $n_1$  to the surface of the entrance window of HAPDs as shown in Fig. 6.3. The aerogel for upstream with  $n_1 = 1.0467$  was produced by the conventional method, and the downstream aerogel  $n_2 = 1.0592$  was produced by the pin-drying method. Both aerogel tiles were trimmed with the squared shape, and a size of them were 182 mm and 168 mm, respectively.

The cross-sectional photograph of the constructed prototype ARICH counter is shown as Fig. 6.2. Electron beam comes from the right hand side in this photograph. In the beam test, to investigate the basic performance of the prototype ARICH counter, we arranged to locate the prototype counter such that the surface of the aerogel in the prototype counter was perpendicular to the beam direction.

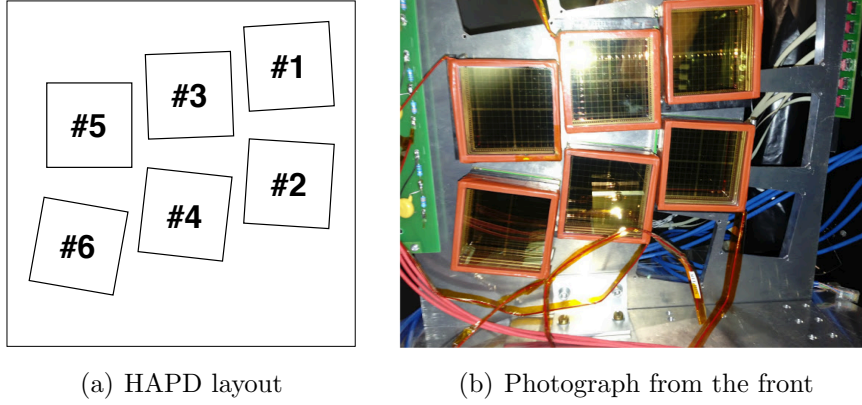


Figure 6.1: The HAPD layout of the prototype ARICH counter (a) and the photograph (b).

Table 6.1: Specification of the prototype ARICH used for this study.  $n$  is the refractive index,  $\Lambda_T$  is the transmission length and  $d$  is the thickness for an individual aerogel tile.

Aerogels	Position	$n$	$\Lambda_T$	$d$	dimensions
	Upstream	1.0467	47 mm	20.3 mm	$182 \times 182 \text{ mm}^2$
	Downstream	1.0592	59 mm	20.3 mm	$168 \times 168 \text{ mm}^2$
HAPDs	ID	QE(peak)	Remarks		
	No.1	27.4%			
	No.2	25.2%			
	No.3	28.9%			
	No.4	31.1%	neutrons and $\gamma$ -ray irradiated		
	No.5	26.8%			
	No.6	22.3%			

## 6.2 Overview of the beam test at DESY

In order to perform the beam test using the prototype ARICH counter, we used the DESY test beam line, T24 [61]. In the DESY test beam facility, a bremsstrahlung is generated by colliding a beam of the DESY II electron/positron synchrotron onto the fixed target. The radiation photons are converted to  $e^+e^-$  pairs with a metal plate. Then the electrons are spread out into a horizontal fan with a dipole magnet located in the downstream of the conversion target, and the electron test beam is generated by cut out the electrons spreader out of this fan with a collimator. By changing the magnetic field of the dipole magnet, beam energy can be selected up to 6 GeV.

The beam parameters used for our beam test and general informations are summarized in the Table 6.2. We basically took the data using 5 GeV electron beam, and the beam direction was selected such that it was perpendicular to the photodetector and aerogel planes. All the tests were carried out in the absence of a magnetic field at the ARICH

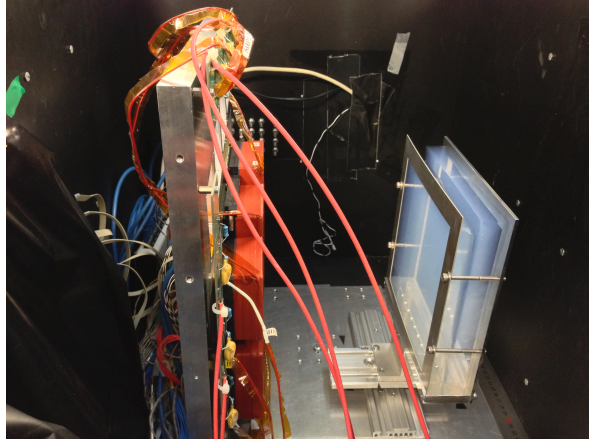


Figure 6.2: The photograph of the prototype ARICH counter in the light-tight box.

area.

Table 6.2: Summary of the beam test using the prototype ARICH counter at DESY. Informations for the DESY test beam facility are found in Ref.[61].

Location	DESY test beam T24
Period	20 – 27 May, 2013
Beam particle	electron
Beam energy	5 GeV
Injection rate	$\sim 500$ Hz at 5 GeV
DAQ rate (average)	250 Hz

## Trigger and tracking system

A pair of plastic scintillation counters and four multi-wire projection chamber (MWPC) modules were used for the trigger generator and beam tracking detector, respectively. They were located in front side and rear side of the light-tight box accommodating the prototype counter. The beam direction and location each equipments are indicated in Fig. 6.3.

Fig. 6.4 shows the schematic of the top view of the setup in the light-tight box and MWPCs located just in front and rear of the light-tight box. We located the prototype counter that consists of two aerogel tiles and the array of six HAPDs such that an electron beam pass through on the center of the whole system.

A pair of plastic scintillation counters is used for trigger. By taking the coincidence of signals from two scintillators, trigger signal was created.

We used multi-wire proportional chamber (MWPC) modules as the two-dimensional tracking device. The sensitive area of the MWPC module corresponds to  $5 \times 5$  cm<sup>2</sup> with



wire pitch of 2 mm for each module, then one-dimensional tracking resolution corresponds to  $2/\sqrt{12}$  mm, respectively.

Fig. 6.6 is the beam profile on the X–Y plane of the HAPD array. The beam size was found to be about  $4 \times 4$  cm<sup>2</sup>.

Table 6.3: The specification of a MWPC module.

Anode (Wire)	# of wires	Diameter [ $\mu$ m]	
	26	15	
Cathode (X & Y) (Strip line)	# of strips	Width [mm]	Pitch [mm]
	30	1.6	2.0
Entering window	$55 \times 55$ mm <sup>2</sup>		
Gas	Ar:CO <sub>2</sub> (70:30)		



Figure 6.5: The schematic of the cross-sectional view of cathode and anode plane in a MWPC module.

## Readout electronics

HAPD signals were read out by the front-end boards attached to the back planes of the HAPD modules. The neutron-irradiated HAPD (that corresponds to HAPD No.4) have large shot noise coming from the neutron dose. For that HAPD, we require short shaping time to suppress the noise. The shaping time of the ASICs in the front-end boards are set to be 100 ns for HAPD Nos. 2, 4, and 6, and 250 ns for Nos. 1, 3, and 5.

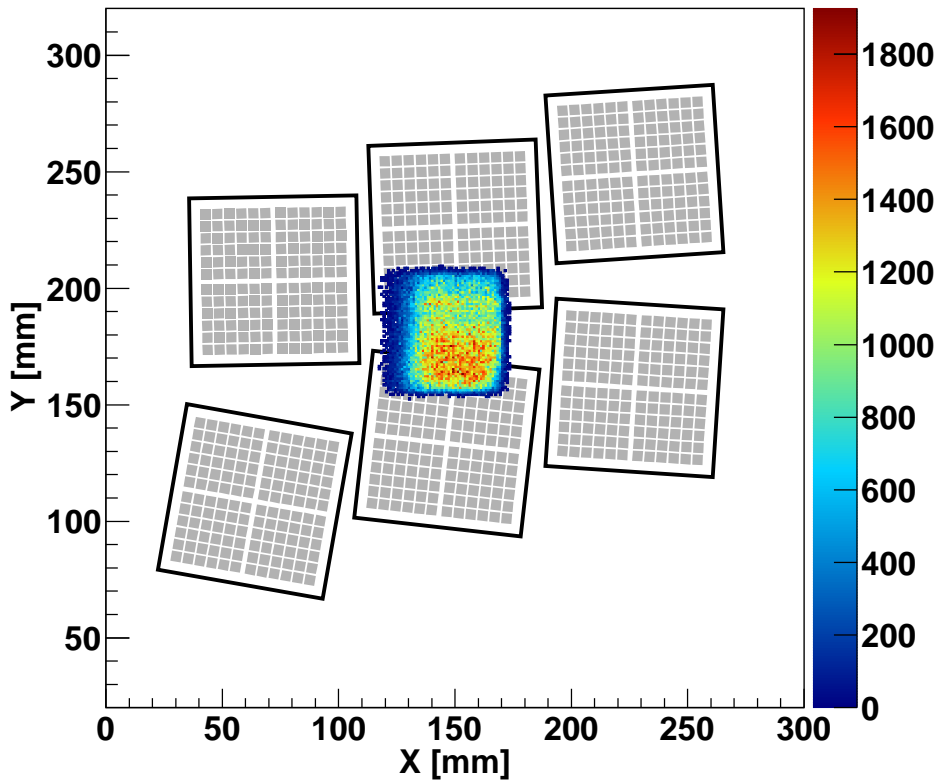


Figure 6.6: The beam profile on the surface of HAPD array.

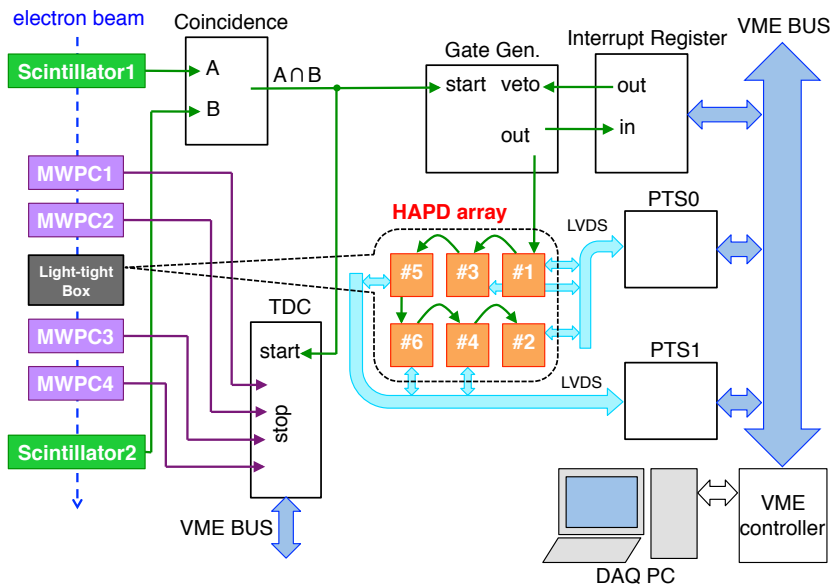


Figure 6.7: The block diagram of data acquisition system for the prototype ARICH beam test.

## 6.3 Measuring Cherenkov angle $\theta_C$ and number of photoelectrons $N_{pe}$

In this section, I describe how we perform  $\pi/K$  identification from the quantities, i.e. Cherenkov angle  $\theta_C$  and/or the number of photoelectrons  $N_{pe}$  that are measured for each event by the prototype RICH counter. I also discuss the possible errors of the particle identification using the prototype RICH counter.

### 6.3.1 Reconstruction of the Cherenkov angle $\theta_C$

In this subsection, the way how to determine emission angle  $\theta_C$  of Cherenkov photons in the ARICH counter is given. Fig. 6.8 define parameters used for the determination of a Cherenkov angle. In the following explanations I use the coordinate that  $z$ -axis is defined as the direction of charged track trajectory and  $X$ - $Y$  plane is defined to be perpendicular to  $z$ -axis.

In order to determine the Cherenkov angle of every Cherenkov photon, the radius of a Cherenkov ring is reconstructed as the following steps:

1. The incident point of the charged track on the HAPD array surface  $(x_0, y_0)$  is calculated by interpolating by two MWPCs located in front and rear of the light-tight box.
2. A charged track is passing through a radiator with a refractive index  $n$  and a thickness  $d$ .
3. The hit point  $(x, y)$  of a Cherenkov photon is determined by the position of the APD pixel where the photoelectron injected.
4. The radius  $r$  of a Cherenkov ring is calculated as the distance between the track incident point and the photon detected point.
5. For each Cherenkov photon,  $\theta_C$  is reconstructed by  $\tan \theta_C = r/L$ . Here, the emission point  $z_e$  is assumed as the middle of the upstream aerogel, then the path length  $L$  is defined as  $L = 200(\text{mm}) - \frac{d_1}{2}$ . In this beam test,  $L$  is to be 189.85 mm.

Since the ARICH counter is the dual-radiator focusing type, we have to correct the reconstructed Cherenkov angle for the refraction effect at every boundary of materials. The schematic of the correction of the refraction shows in Fig. 6.9, and the corrected ring radius  $r$  is given as follows:

$$\sin \theta_i = \frac{n_1}{n_i} \sin \theta_1, \quad (6.1)$$

$$r = \sum_{i=1}^{N=4} r_i \equiv \sum_{i=1}^{N=4} d_i \tan \theta_i, \quad (6.2)$$

where  $n_i$ ,  $d_i$  ( $i=1-4$ ) are refractive indices and thicknesses of each material.  $\theta_i$  is the refractive angle of the  $i$ th material, and it is given by the Snell's law Eq.(4.1). indices  $i$  mean the  $i$ -th material from the upstream aerogel  $n_1$  to the entrance window (quartz)  $n_4$ .

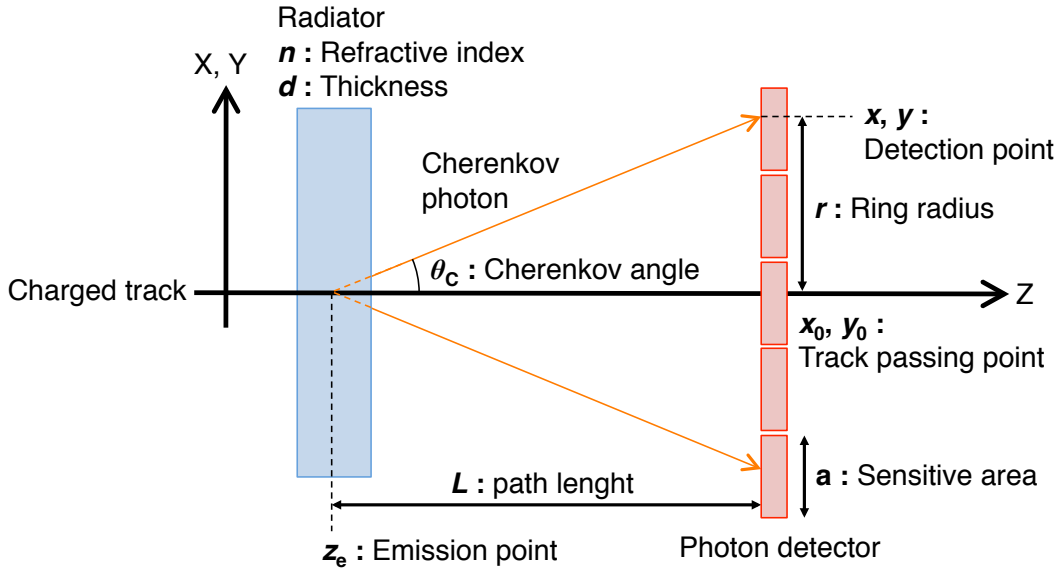


Figure 6.8: The schematic of the considerable parameters used for to determine of the Cherenkov angle resolution  $\theta_C$ .

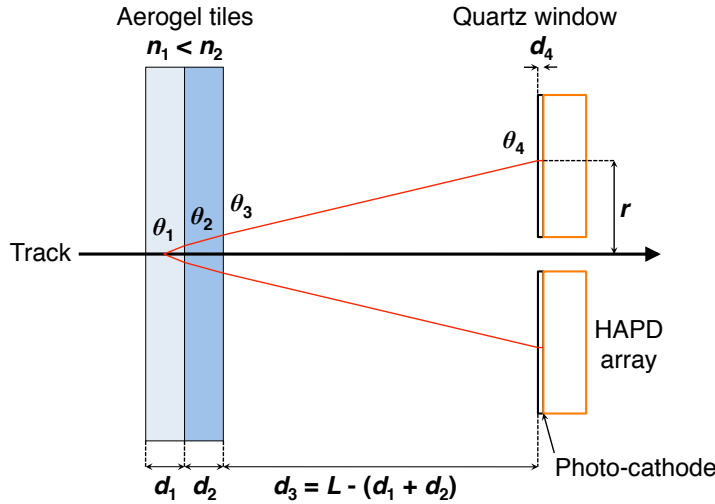


Figure 6.9: The schematic of the principle of Cherenkov angle reconstruction at the ARICH counter.  $d_i$  are thickness of each materials,  $\theta_1$  is the emission angle corresponding to  $\theta_C$ , and  $\theta_i$  are refractive angle  $n_i$  at the  $i$ th material given by the Snell's law Eq.(4.1). The emission point  $z_e$  is assumed at the middle of  $d_1$ .

### 6.3.2 Cherenkov angle resolution $\sigma_\theta$

Fig. 6.8 shows the geometrical parameters used to determine the Cherenkov angle resolution  $\sigma_\theta$  In this prototype ARICH counter test. The  $\sigma_\theta$  can be estimated by the following errors:

1. Measurement errors for photon detection point  $(x, y, z)$ .

2. Geometric error originated from the photon emission point  $z_e$ .
3. Chromatic error due to the dependency of a photon energy  $E$  in the refractive index.
4. Incident position error for the entering charged particle.

The total Cherenkov angle resolution is given by following relation as:

$$\sigma_\theta = \sqrt{\sum_i \left( \frac{\partial \theta}{\partial v_i} \sigma_{v_i} \right)^2}, \quad (6.3)$$

where  $v_i = x, y, z, z_e, E, x_H$  are the variables contributing to the angle resolution, and  $x_H$  is the difference between the measured and correct position of an incident charged particle. Here, I ignore the correlations among the variables, since they are expected to be small enough.

Geometrical constants in the prototype ARICH counter system used to estimate the Cherenkov angle resolution  $\sigma_\theta$ , are listed in Table 6.4. In the following subsection, I estimate how uncertainties of variables can contribute into the Cherenkov angle resolution  $\sigma_\theta$  obtained by the beam test using the prototype ARICH counter. Here, the Cherenkov angle  $\theta_C$  for an electron with momentum of 5 GeV/ $c$  at the upstream aerogel  $n_1$  is estimated as 299.84 mrad by using Eq.(3.5).

Table 6.4: Geometrical constants in the prototype ARICH system.

Refractive index $n_1$	1.0467
Radiator thickness $d_1$	20.3 mm
Emission point $z_e$	$d_1/2 = 10.15$ mm (middle of thickness)
Path length $L$	$200.0(\text{mm}) - \frac{d_1}{2} = 189.85$ mm
HAPD pixel size $a$	4.9 mm

### 1. Position measurement errors

This error is evaluated from position resolutions  $(\sigma_x, \sigma_y)$  that are originated in the determination accuracies of the photon detection point  $(x, y)$  on a photon detector surface. When photon detectors having pixelated sensitive squared pads with a pixel size of  $a \times a$ , are employed for a RICH counter and when  $a$  is sufficiently smaller than a path length  $L$  ( $a \ll L$ ), we can consider that  $\sigma_x$  and  $\sigma_y$  approximately correspond to the position resolution of a sensitive pixel size  $\sigma_{\text{pix}}$ . It can be estimated by the following equation:

$$\sigma_x = \sigma_y = \sigma_{\text{pix}} \equiv \frac{a}{\sqrt{12}}. \quad (6.4)$$

This error is an irreducible error, and can not be reduced without using a smaller pixel size photon detector. Although, in general, the determination of detection point is performed

three-dimensionally, the error for  $z$  direction can be approximately ignored when the path length  $L$  is sufficiently longer than the Cherenkov ring radius  $r$ .

When condition  $\tan \sigma_\theta(x) \sim \sigma_\theta(x)$  is satisfied (i.e.  $\sigma_\theta(x) \ll 1$ ), the factor  $\partial\theta/\partial x$  can be considered as the geometrical conversion factor between the angle and the spacial resolution. Finally, the corresponding resolution  $\sigma_\theta(x)$  in the Cherenkov angle can be estimated as follows:

$$\sigma_\theta(x) = \left( \frac{\partial\theta}{\partial x} \right) \sigma_{\text{pix}} = \frac{a}{L\sqrt{12}} \cos^2 \theta_C. \quad (6.5)$$

In our prototype ARICH counter,  $\sigma_\theta(x)$  is estimated as 6.80 mrad.

## 2. Geometric error

This error stems from an uncertainty in the emission point  $z_e$  of Cherenkov photons along a radiator thickness  $d$ . When we calculate the Cherenkov angle, a emission point  $z_e$  is fixed as the middle of  $d$  approximately. Because, in principle,  $z_e$  can not be measured, it has an irreducible error  $\sigma_{z_e}$  defined as follows:

$$\sigma_{z_e} \equiv \frac{d}{\sqrt{12}}. \quad (6.6)$$

This error can not be reduced without making the radiator thickness thinner or without making the path length  $L$  to be much longer than  $d$  ( $d \ll L$ ).

When condition  $\tan \sigma_\theta(z_e) \sim \sigma_\theta(z_e)$  is satisfied (i.e.  $\sigma_\theta(z_e) \ll 1$ ), the factor  $\partial\theta/\partial z_e$  can be considered as the geometrical conversion factor between the angle and the spacial resolution. Finally, the corresponding resolution  $\sigma_\theta(z)$  in the Cherenkov angle can be estimated as follows:

$$\sigma_\theta(z_e) = \left( \frac{\partial\theta}{\partial z_e} \right) \sigma_{z_e} = \frac{d}{L\sqrt{12}} \cos \theta_C \sin \theta_C. \quad (6.7)$$

In our prototype ARICH counter,  $\sigma_\theta(z_e)$  is estimated as 8.71 mrad.

## 3. Chromatic error

This error contributes in the Cherenkov angle resolution through the variation of a radiator refractive index  $n$  depending on a Cherenkov photon energy  $E$ , and it is determined by the dispersion of radiator materials.

The corresponding resolution  $\sigma_\theta$  with respect to a chromatic error  $\sigma_E$  is evaluated as follows:

$$\sigma_\theta(E) = \left( \frac{\partial\theta}{\partial n} \right) \left( \frac{\partial n}{\partial E} \right) \sigma_E, \quad (6.8)$$

where  $E = hc/\lambda$  is energy of the detected Cherenkov photon with the wavelength  $\lambda$ .

The first factor of Eq.(6.8) is obtained by the derivative of Eq.(3.4), as

$$\frac{\partial\theta}{\partial n} = \frac{1}{n \tan \theta_C}. \quad (6.9)$$

The second factor of Eq.(6.8) is known as the radiator dispersion. In general, this dispersion can be explained by the Lorenz-Lorentz relation as follows:

$$\frac{n^2 - 1}{n^2 + 2} = Cf(E), \quad (6.10)$$

where  $C$  is the material density dependent constant, and  $f(E)$  is the energy dependency of the refractive index  $n$ , respectively.

Since the silica aerogel used in the ARICH counter is a low density material (0.02–0.5 g/cm<sup>3</sup>), the energy dependency of the refractive index of an aerogel is negligible. Thus we can consider that the energy dependency corresponding to the second factor in Eq.(6.8) is approximately a spread of a refractive index  $\sigma_n$ . Therefore the chromatic error can be represented by the accuracy of the refractive index as follows:

$$\sigma_\theta(E) \simeq \frac{\sigma_n}{n \tan \theta_C}. \quad (6.11)$$

The  $\sigma_n$  for the aerogel with  $n = 1.05$  was measured by [36], then the  $\sigma_n = 0.0008$  was obtained. By using the above value,  $\sigma_\theta(E)$  is estimated as 2.47 mrad.

#### 4. Incident particle position error

This error is given by the position resolution  $x_H$  of the tracking detector. Fig. 6.10 shows the schematic of the determination of the angular resolution  $\sigma_\theta(x_H)$  from the tracking error. The track incident position  $x_H$  at the HAPD surface is determined by interpolating the track using the information from a pair of MWPCs located in just front and rear of the light-tight box.  $x_H$  is given as  $x_H = \alpha x_2 + (1 - \alpha)x_1$ , where  $\alpha = L'/\Delta Z = 0.598$ . Then, the incident position error  $\Delta x_H$  is given as  $(\Delta x_H)^2 \simeq \alpha^2(\Delta x_2)^2 + (1 - \alpha)^2(\Delta x_1)^2$ , where  $\Delta x_1$  and  $\Delta x_2$  correspond to the one-dimensional position resolution of a MWPC. Since two MWPCs have the same position resolution of  $\Delta x_1 = \Delta x_2 = 2/\sqrt{12}$  mm,  $\Delta x_H$  is estimated as 0.423 mm.

The conversion from the position resolution  $\Delta x_H$  to the angular resolution  $\sigma_\theta$  is the same as that from the position resolution of a HAPD ( $\sigma_{\text{pix}}$ ) and is given as follows:

$$\sigma_\theta(x_H) = \frac{\Delta x_H}{L} \cos^2 \theta_C. \quad (6.12)$$

As the result,  $\sigma_\theta(x_H)$  is estimated as 2.03 mrad for the beam test.

Note that this is not a part of the intrinsic resolution of the ARICH. The incident particle position is given by CDC at Belle II, and the resolution estimated in above should be different at Belle II.

#### Total angular resolution $\sigma_\theta$

Since the correlations among the above four errors are expected to be small enough, the total angular resolution  $\sigma_\theta$  is estimated by the square root of the summing of them in quadrature. As the result, we can estimate the  $\sigma_\theta$  is to be 11.50 mrad.

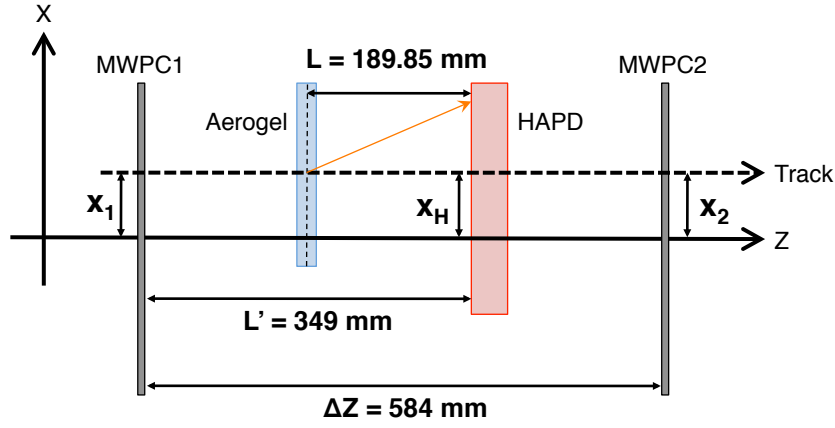


Figure 6.10: The schematic of the determination of the tracking resolution  $\sigma_{x_H}$ .

### 6.3.3 Cherenkov photon yield $N_{pe}$

The number of detected photoelectrons  $N_{pe}$  can be estimated by the Frank-Tamm relation Eq.(3.7) adding detection efficiencies of the RICH counter. For the (prototype) ARICH counter, they correspond to the quantum efficiency  $\epsilon_Q(E)$ , transmittance  $T$ , and geometrical acceptance  $\epsilon_a$ .

In order to evaluate the fraction of  $N_{pe}$  in the radiator, the transmittance  $T(\lambda)$  and the emission point dependency are described in this section. In general, the total transmittance  $T(\lambda)$  is given as follows:

$$T(\lambda) = A \cdot S(\lambda), \quad (6.13)$$

where  $A$  is the absorption without  $\lambda$  dependence, and  $S(\lambda)$  is the inner scattering that is dominantly the Rayleigh scattering depending to  $\lambda^4$  for the aerogel radiator.

#### Absorption

The  $N_{pe}$  degradation that is independent of wavelength, is explained as the absorption  $A$  in the radiator.  $A$  is defined using the absorption length  $\Lambda_A$  as follows:

$$A = \exp\left[-\frac{d}{\Lambda_A}\right]. \quad (6.14)$$

$A$  is also one of the Hunt parameter, and if a radiator has a good optical quality,  $A$  should be close to one.

#### Rayleigh scattering

Because the wavelength of a Cherenkov photon is mainly distributed around the visible light range (200–800 nm), the Rayleigh scattering becomes the dominant source of the  $N_{pe}$  degradation in the aerogel radiator. The transmission regards to the Rayleigh scattering

in the silica aerogel  $S(\lambda)$  is usually represented as follows:

$$S(\lambda) = \exp \left[ -\frac{Cd}{\lambda^4} \right], \quad (6.15)$$

where  $\lambda$  is wavelength of a Cherenkov photon,  $d$  is the radiator thickness, and  $C$  is called the Hunt parameter [62], respectively. The  $C$  indicates clarity of the radiator, and the combination  $Cd$  is usually measured in  $[\mu\text{m}^4]$  units. If a radiator has a good optical quality,  $C$  should be close to zero.

### Emission point dependency

In practical situation, there is an ambiguity about the emission point  $z$ . Furthermore a Cherenkov photon is emitted with the Cherenkov angle  $\theta_C$  in the radiator. Therefore  $d$  in Eq.(6.14) and (6.15) should be replaced to the effective path length as follows:

$$d \rightarrow \frac{d - z_e}{\cos \theta_C}. \quad (6.16)$$

By calculating the integral of the Eq.(3.7) for  $z_e$  instead of  $x$ , the differential  $dN_{\text{pe}}/d\lambda$ , which takes into account the above transmittance and the emission point dependency, is obtained as follows:

$$\begin{aligned} \frac{dN_{\text{pe}}}{d\lambda} &= N_0 \int_0^d T(\lambda) dz_e, \\ &= N_0(\lambda) \epsilon_Q(E) \epsilon_a \int_0^d \exp \left[ -\frac{(d - z_e)}{\Lambda(\lambda) \cos \theta_C} \right] dz_e, \\ &= N_0(\lambda) \epsilon_Q(E) \epsilon_a \Lambda(\lambda) \cos \theta_C \left( 1 - \exp \left[ -\frac{d}{\Lambda(\lambda) \cos \theta_C} \right] \right), \end{aligned} \quad (6.17)$$

where

$$\frac{1}{\Lambda(\lambda)} \equiv \frac{C}{\lambda^4} + \frac{1}{\Lambda_A}, \quad (6.18)$$

$$N_0(\lambda) \equiv \frac{2\pi\alpha}{\lambda^2} \sin^2 \theta_C. \quad (6.19)$$

### Estimation of $N_{\text{pe}}$

According to the above absorption and scattering in aerogel tiles, the number of detected photoelectrons  $N_{\text{pe}}$  can estimate in the following. The number of photoelectrons from the upstream aerogel tile  $N_1$  is estimated by the following equation:

$$\begin{aligned} N_1 &= 2\pi\alpha \sin^2 \theta_{C1} \epsilon_a \int \exp \left( -\frac{d_2}{\Lambda_2(\lambda) \cos \theta_{C1}} \right) \\ &\quad \times \Lambda_1(\lambda) \cos \theta_{C1} \left( 1 - \exp \left( -\frac{d_1}{\Lambda_1(\lambda) \cos \theta_{C1}} \right) \right) \epsilon_q(\lambda) \lambda^{-2} d\lambda, \end{aligned} \quad (6.20)$$

where  $\theta_{C1}$  is the Cherenkov angle in the upstream aerogel tile, and  $\Lambda_1$  and  $\Lambda_2$  are total transmission length for the radiator with  $n_1$  and  $n_2$ , respectively.

The number of photoelectrons from the downstream aerogel tile  $N_2$  is estimated by the following equation:

$$N_2 = 2\pi\alpha \sin^2 \theta_{C2} \epsilon_a \times \int \Lambda_2(\lambda) \cos \theta_{C1} \left( 1 - \exp \left( -\frac{d_2}{\Lambda_2(\lambda) \cos \theta_{C2}} \right) \right) \epsilon_q(\lambda) \lambda^{-2} d\lambda, \quad (6.21)$$

where  $\theta_{C2}$  is the Cherenkov angle in the downstream aerogel tile. Here,  $\epsilon_a$  is the photon acceptance of the prototype ARICH including the geometrical acceptance and detection efficiency of the HAPD, and is estimated to be around 42% in the test,  $\epsilon_q$  is the quantum efficiency of each HAPD as shown in Fig. 6.11,  $\lambda$  is the wavelength of a Cherenkov photon and  $\alpha$  is the fine structure constant. Finally, total number of photoelectron is obtained as follows:

$$N_{pe} = N_1 + N_2. \quad (6.22)$$

As the result, the number of photoelectrons is estimated to be  $N_{pe} = N_1 + N_2 = 2.787 + 7.969 = 10.756$ .

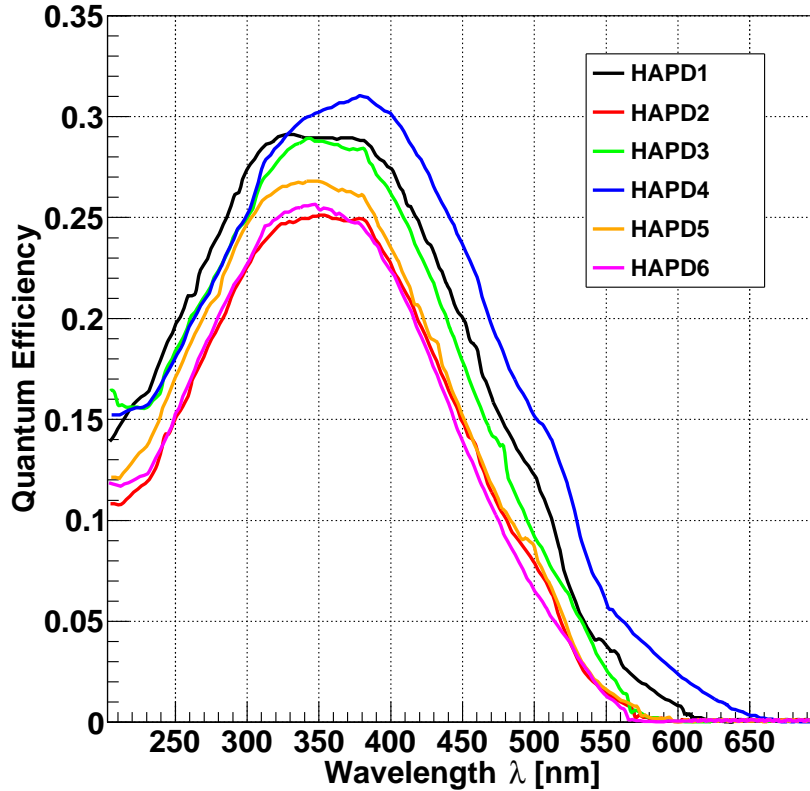


Figure 6.11: Quantum efficiencies of HAPDs mounted in the prototype ARICH counter as a function of wavelength [54].

### 6.3.4 Summary of prospections

Here, I conclude the expected measurement variables and Cherenkov angle resolution.

$$\theta_C^{\text{exp}} = 299.84 \text{ mrad}, \quad (6.23)$$

$$N_{\text{pe}}^{\text{exp}} = N_1 + N_2 = 2.787 + 7.969 = 10.756. \quad (6.24)$$

Table 6.5: Error estimation in the measurement of Cherenkov angle  $\theta_C$ .

	Error	Corresponding resolution [mrad]
Position measurement $\sigma_\theta(x)$		6.80 [Eq.(6.5)]
Emission point $\sigma_\theta(z_e)$		8.71 [Eq.(6.7)]
Chromatic $\sigma_\theta(E)$		2.47 [Eq.(6.11)]
Tracking $\sigma_\theta(x_H)$		2.03 [Eq.(6.12)]
Total		11.50

## 6.4 Analysis

### 6.4.1 Analyzed data set

The beam status and configuration of the prototype ARICH that are used for this study, are summarized in Table 6.6 and Table 6.1, respectively.

Table 6.6: Information of the analyzed beam test data.

Run#	Date	beam energy [GeV/c]	DAQ time (rate)	# of acquired events
125	May 26, 2015	5.0	881.7 sec (235.2 Hz)	207,415

### 6.4.2 Single-track extraction

Fig. 6.12 shows the event display for the typical event.

In order to evaluate the basic performance of the ARICH, we analyzed the number of detected Cherenkov photoelectrons and their angular resolution. Multi-track events were also rejected by using information from trigger counters and MWPC modules. Those selections at the hardware level, however can not fully reject multi-track events. We also applied an analytical selection to farther reject such events in offline analysis.

Fig. 6.14 shows the distribution of the number of detected Cherenkov photons per event. Only photons within the ring area with Cherenkov angle in the range of  $\pm 45$  mrad

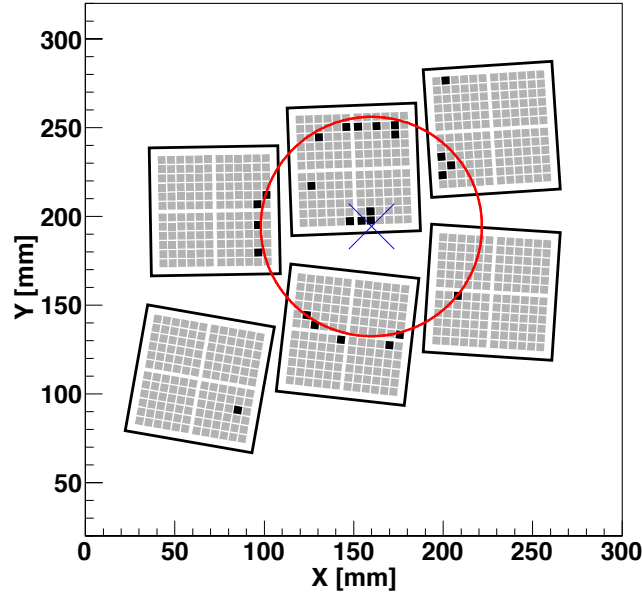


Figure 6.12: An example of the hit map for the typical event.

around the expected Cherenkov angle were counted. Here, 45 mrad equals  $3\sigma$  of the Cherenkov photons angular distribution obtained by fit.

In order to separate single track events from multi-track events, we assumed that the distribution (Fig. 6.14) was represented by the following form:

$$A_1 Po(N + B) + A_2 Po(2N + B) + A_3 Po(3N + B), \quad (6.25)$$

where  $Po(x)$  is the Poisson function,  $A_i$  are coefficients corresponding to number of events with  $i$  tracks,  $N$  is the number of detected Cherenkov photons per track and  $B$  is the average number of uncorrelated background hits per event.

Fig. 6.16 shows angular distribution of the Cherenkov light, which was extracted form after the rejection of multiple track events. The extraction was performed by fitting the distributions of number of photoelectrons using Eq.(6.25) for every 0.002 rad of the Cherenkov angle distribution as shown in Fig. 6.15. Here  $A_1$  in Eq.(6.25) corresponds to the number of events of single-track for each Cherenkov angle.

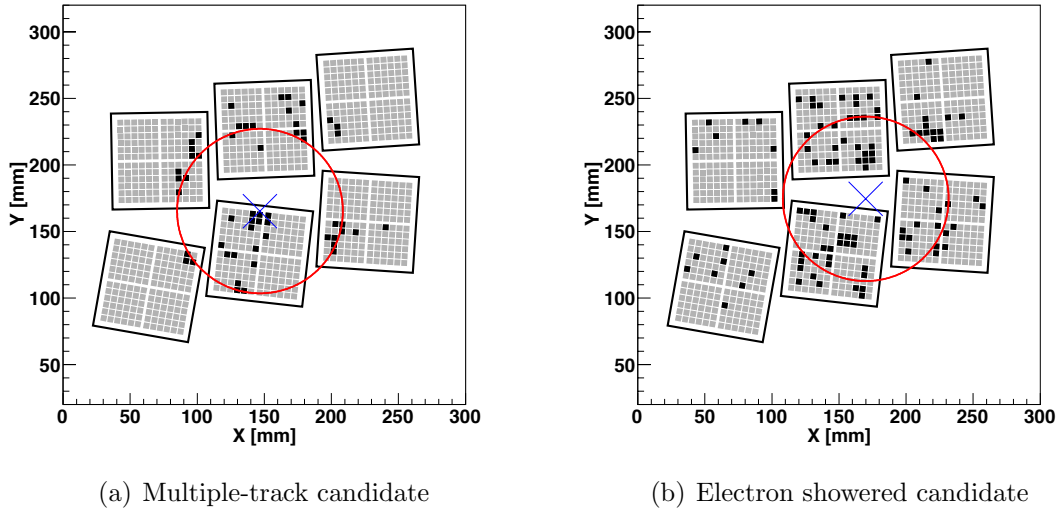
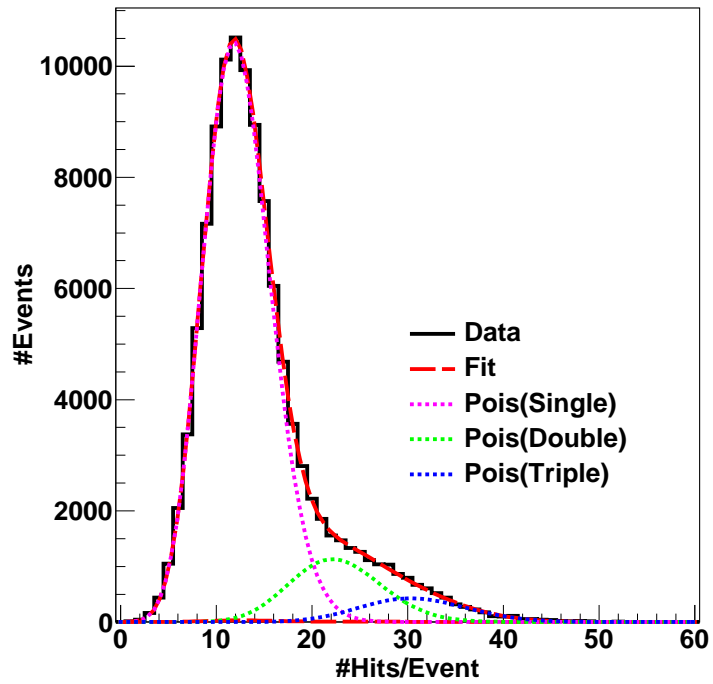


Figure 6.13: Examples of the hit map that were considered the multiple track event.



(a) Number of detected hits per an event

Figure 6.14: Distribution of the number of detected photons per an event. The solid line (red) represents the fitted function (Eq.(6.25)), and the dotted lines (blue) show decomposed Poisson functions corresponding to single, double and triple track events.

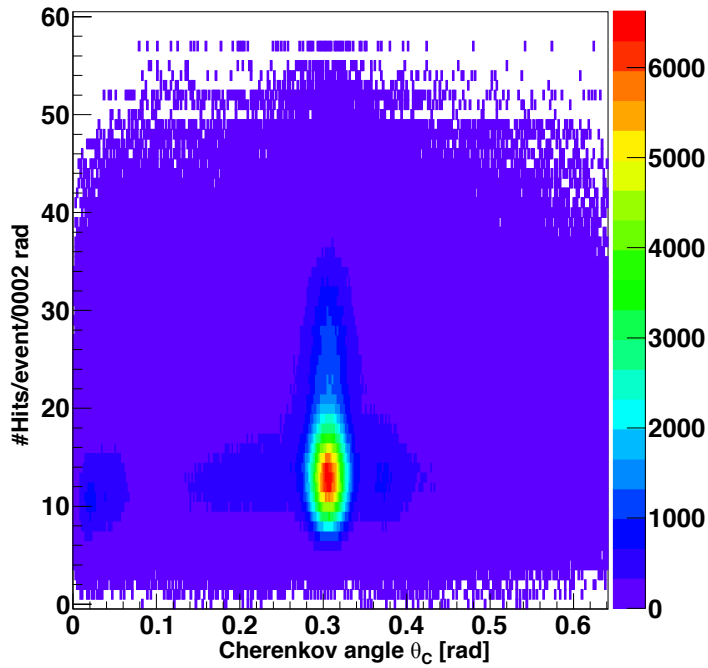


Figure 6.15: Number of hits per an event as a function of reconstructed emission angle.

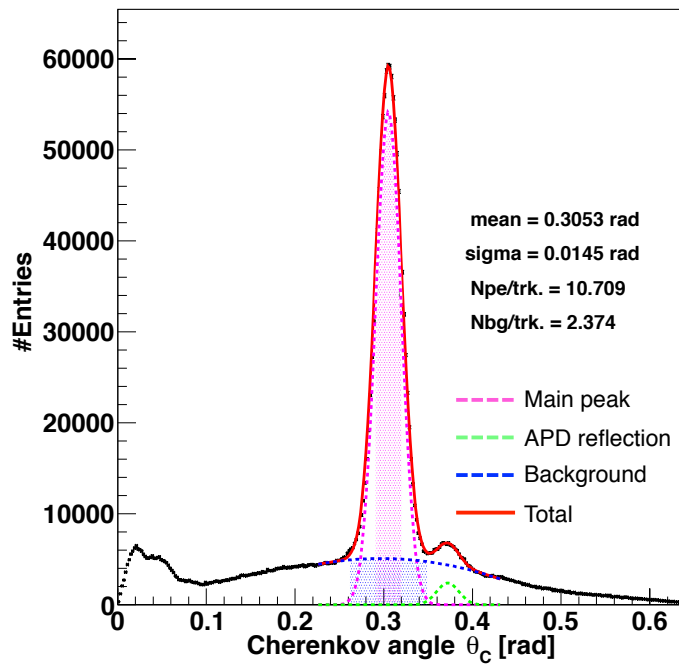


Figure 6.16: The extracted Cherenkov angular distribution. The solid line (red) represents the fitting function. The dotted lines represent the primary peak (magenta), the secondary peak (green) and background structures (blue).

## 6.5 Results

### 6.5.1 Observation of a Cherenkov ring

Fig. 6.17 shows the Cherenkov ring images from the prototype, a typical hit map of an event and the accumulated hit positions with respect to the track. We successfully observe very clear ring images using the prototype ARICH counter including irradiated HAPD.

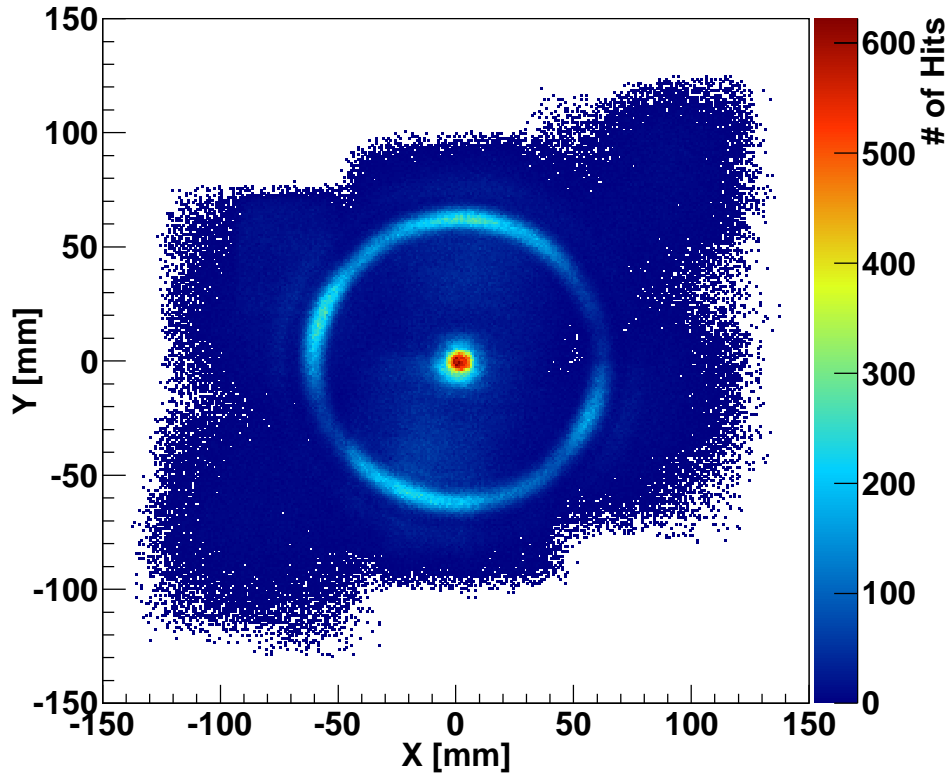


Figure 6.17: The accumulated Cherenkov ring image.

### 6.5.2 Measurement of Cherenkov angle $\theta_C$

Fig. 6.18 shows the comparison between the Cherenkov distribution with and without aerogel tiles. The red line corresponds to the data with dual aerogel tiles, and the green line corresponds to the data without any aerogel tiles. The data without aerogel tiles means that the distribution was formed by the contribution besides the Cherenkov light generated in the aerogel tile.

The peak indicated as (1) is the primary Cherenkov photons peak. The peak of (2) generated by the Cherenkov photon that produced in the entering quartz of the HAPD. As shown in Fig. 6.19 (a), the Cherenkov photon generated in the quartz should be totally reflected in the quartz. Therefore, that photon can convert to a photoelectron that forms

the small peak below 0.1 rad. The peak of (3) generated by the internal reflection of the Cherenkov photon on the APD surface. As shown in Fig. 6.19 (b), the Cherenkov photon that did not convert to a photoelectron, should be reflected on the APD surface. Therefore, the reflected photon can convert to a photoelectron that forms the small peak around the 0.36 rad. The broad distribution of (4) corresponds to the Rayleigh scattering light.

The Cherenkov angle is obtained by fitting the extracted Cherenkov angle distribution Fig. 6.16 with a Gaussian corresponding to a magenta dashed line for the primary Cherenkov peak, 2nd-order polynomial function corresponding to a blue dashed line for the background including the Rayleigh scattering, and a Gaussian corresponding to a green dashed line for the peak by the APD reflected photons. The red solid line corresponds to the total fitting function summing of the above three functions. By the fitting with the above function, we obtained the Cherenkov emission angle  $\theta_C$  to be  $305.30 \pm 0.16$  mrad, and the angular resolution  $\sigma_\theta$  to be 14.47 mrad from the Gaussian assumption.

The measured Cherenkov angle (305.30 mrad) and angular resolution (14.47 mrad) are slightly different compared with the above estimations to be 299.84 mrad and 11.50 mrad for  $\theta_C$  and  $\sigma_\theta$ , respectively. The main cause of these discrepancies between the expectations and measurements may be considered by the effect of the electric field distortion in the HAPD without a magnetic field. By this effect, the Cherenkov photon entering in near the wall of the HAPD can not be detected the correct position (see Fig. 5.7). Then, by considering the correction of this effect without a magnetic field, we expect to reduce these discrepancies.

### 6.5.3 Photoelectron yield

We obtained the average number of detected photoelectrons  $N_{pe}$  from the area above the background form. It amounts to  $N_{pe} = 10.71 \pm 0.11$  per a track. The result is almost consistent with expected  $N_{pe}$  (= 10.756).

### 6.5.4 Estimation of $\pi/K$ separation power

The performance of the  $\pi/K$  separation  $n_S$  is can be estimated using the Eq.(3.11):

$$n_S = \frac{\Delta\theta_C}{\sigma_\theta} \sqrt{N_{pe}}.$$

Here,  $\Delta\theta_C$  is the difference of Cherenkov angles between pion and kaon, it is calculated to be 23.7 mrad at 4 GeV/ $c$  by calculating Cherenkov angles to be 0.2979 rad and 0.2742 rad for a pion and a kaon, respectively. By using the above results of  $\theta_C$  (=14.47 mrad) and  $N_{pe}$  (= 10.71),  $n_S$  corresponds to  $5.36\sigma$  of the  $\pi/K$  separation. Therefore we confirmed that the prototype ARICH counter had sufficient  $\pi/K$  separation power for the Belle II experiment.

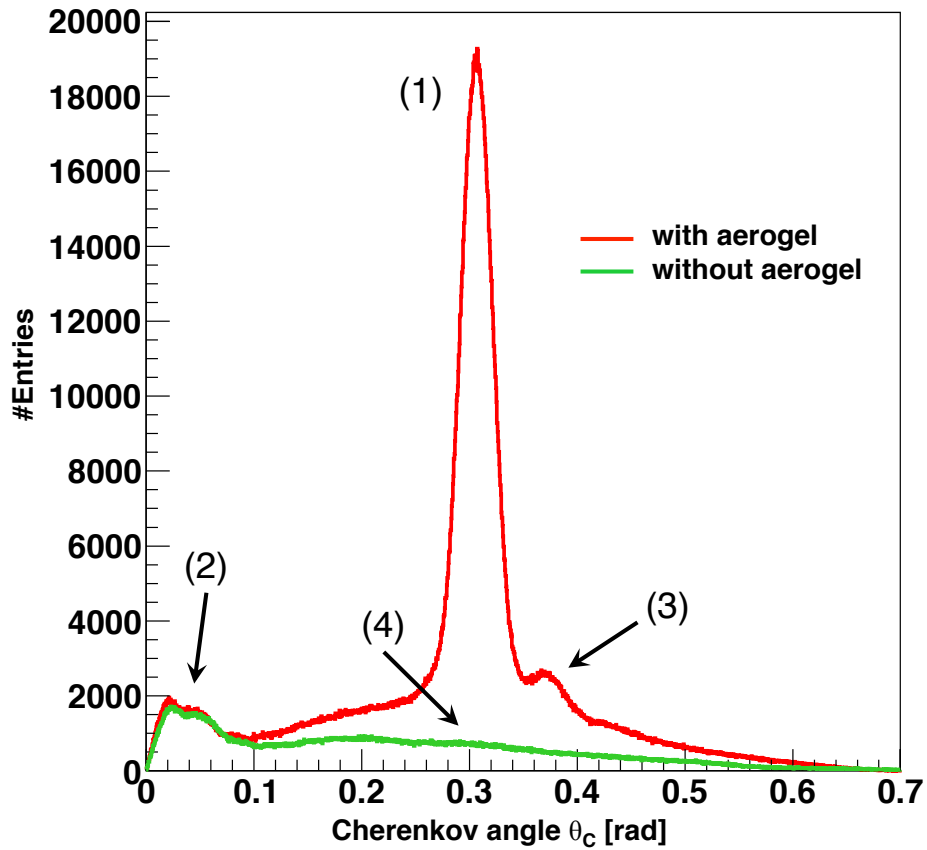


Figure 6.18: The comparison between the distribution with and without aerogel tiles. The red line indicates the data with aerogel tiles, and the green line is the data without any aerogel tiles. Numbers in the figure indicate that (1) the main peak by a Cherenkov light from aerogel tiles, (2) the peak corresponds to Cherenkov photons generated in the entering window quartz of an HAPD, (3) the peak correspond to the reflected light on the APD surface, and (4) the broad distribution generated by the Rayleigh scattering in aerogel tiles, respectively.

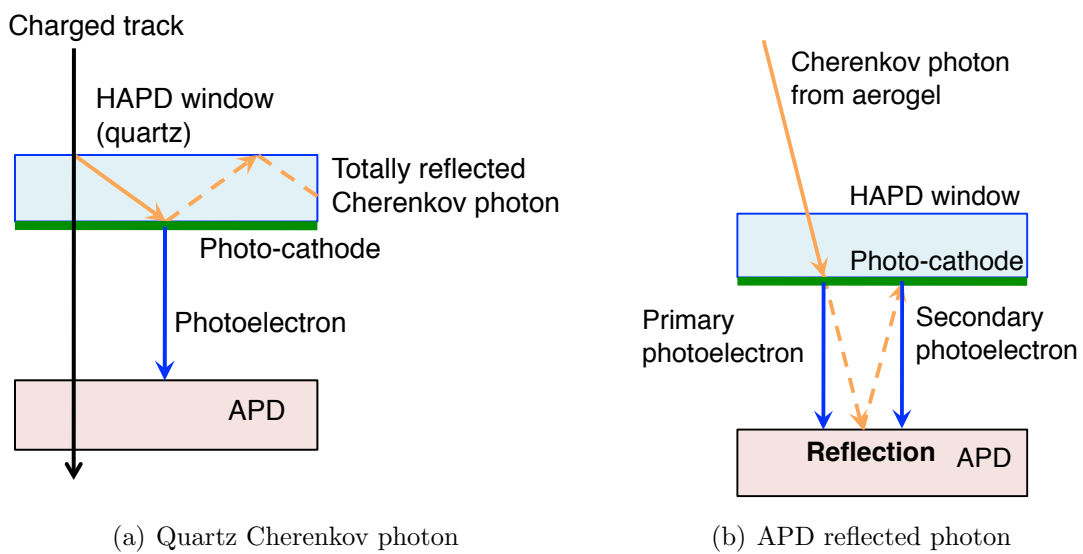


Figure 6.19: Schematically explanations for (a) the Cherenkov photon generated in the window quartz of the HAPD, and (b) the reflected photon on the APD surface in the HAPD.

# Chapter 7

## Evaluation of the PID performance

In this chapter, I discuss the performance of the  $\pi/K$  separation that is estimated from the resolution of an accumulated Cherenkov ring. To study the performance of the  $\pi/K$  separation of the ARICH counter in the realistic situation, we perform event-by-event analysis based on the likelihood method for the beam test data. I defined the probability density functions (PDFs) for distribution of the Cherenkov angle and number of detected photoelectrons. I prepare the PDFs for signal and background assumption. Here, the signal and background are assumed to be pion and kaon, respectively, to emulate  $\pi/K$  identification of the ARICH counter. I calculate Likelihoods for an event of the beam test. I estimate the performance of the  $\pi/K$  separation using Likelihood ratio.

### 7.1 Particle identification using a Likelihood method

In this analysis, we calculate two Likelihood values ( $\mathcal{L}^\pi$  and  $\mathcal{L}^K$ ) that represent the Likelihood to be a pion or a kaon. Using a Likelihood ratio that is calculated as

$$\mathcal{R}^\pi = \frac{\mathcal{L}^\pi}{\mathcal{L}^\pi + \mathcal{L}^K}, \quad (7.1)$$

we can identify a pion with assuming that the background is a kaon.

### 7.2 Definition of the Likelihood

A track that pass through ARICH produces multiple hits of Cherenkov photons. For each hits we can calculate Likelihood for a pion and a kaon as  $\mathcal{L}_{\text{hit}}^\pi = \mathcal{P}_{\text{hit}}(\theta|\theta_C^\pi)$  and  $\mathcal{L}_{\text{hit}}^K = \mathcal{P}_{\text{hit}}(\theta|\theta_C^K)$ , respectively. Here,  $\theta$  denotes angle of a hit of a Cherenkov photon,  $\theta_C^\pi$  ( $\theta_C^K$ ) denotes expected Cherenkov and for pion (kaon) assumption, and  $\mathcal{P}_{\text{hit}}(\theta|\theta_C^\pi)$  and  $\mathcal{P}_{\text{hit}}(\theta|\theta_C^K)$  are defined as probability density functions of Cherenkov angle  $\theta_C$  for pion and kaon assumption, respectively.

The Likelihood for a track can be calculated by taking the product of likelihoods for the hits. The number of hits is also a random Poisson variable with mean value  $N_{\text{pe}}$ , the expected number of photoelectrons. The Likelihood that is usually called extended

Likelihood, can be defined as:

$$\mathcal{L}^\pi \equiv \mathcal{L}^\pi(n_{\text{hit}}, \theta) = \frac{(N_{\text{pe}}^\pi)^{n_{\text{hit}}}}{n_{\text{hit}}!} e^{-N_{\text{pe}}^\pi} \prod_{i=1}^{n_{\text{hit}}} \mathcal{L}_{\text{hit}}^\pi(\theta_i), \quad (7.2)$$

where,  $N_{\text{pe}}^\pi$  is the expected number of photoelectrons for pion assumption,  $n_{\text{hit}}$  is the number of hits of a track, and  $i$  is a index that runs other hits. Former term of the Likelihood that is calculated using number of hits only, can be defined as

$$\mathcal{L}^\pi(n) \equiv \frac{(N_{\text{pe}}^\pi)^{n_{\text{hit}}}}{n_{\text{hit}}!} e^{-N_{\text{pe}}^\pi}, \quad (7.3)$$

and latter term of the Likelihood that is calculated using number of hits only, can be defined as

$$\mathcal{L}^\pi(\theta) \equiv \prod_{i=1}^{n_{\text{hit}}} \mathcal{L}_{\text{hit}}^\pi(\theta_i). \quad (7.4)$$

### 7.3 Construction of Probability Density Functions

The PDF for the number of detected photoelectrons ( $N$ ) per event is assumed to be a single Poisson distribution as follows:

$$\mathcal{P}(N|N_{\text{pe}}) = \frac{(N_{\text{pe}})^N}{N!} e^{-N_{\text{pe}}}. \quad (7.5)$$

The mean  $N_{\text{pe}}$  is quoted from the expected value calculated using Eq.(6.22) with the particle mass, the momentum and refractive indices of aerogel layers as parameters. In 3.5 GeV/ $c$ , the expected number of detected photoelectrons is 10.629 and 8.938 for pion and kaon, respectively.

Note that, we made the PDF of the Cherenkov angle  $\Theta$  for pion ( $\mathcal{P}_{\text{hit}}(\Theta|\theta_C^\pi)$ ) and kaon ( $\mathcal{P}_{\text{hit}}(\Theta|\theta_C^K)$ ) based on the electron data because the beam test is performed using the electron beam. Parameters used for calculating the Likelihood  $\mathcal{L}^\pi$  ( $\mathcal{L}^K$ ) are summarized in Table 7.1.

In order to generate the PDF of the Cherenkov angle as a function of momentum for the given mass assumption, we parametrized the Cherenkov angular distribution as the combination of some known functions. The distributions for the primary Cherenkov peak and secondary peak made by the reflections of the photons at the APD surface are assumed as Gaussian. The slightly wide peak below 0.1 rad is originated from the Cherenkov photons, which were generated in the quartz window of the HAPD and assumed as two Gaussians and an 8th-order polynomial. The uncorrelated background is assumed as an 8th-order polynomial. Therefore, the entire distribution is fitted by four Gaussians and two 8th-order polynomial. Fig. 7.1 (a) shows the fitted distribution of the Cherenkov angle.

The entrance window is made of silica quartz with the refractive index of  $n = 1.46$ . Cherenkov photons generated in the quartz window are internally reflected, and when

they reach the photo-cathode plane, they may be converted to photoelectrons with a probability of the quantum efficiency. Those Cherenkov photons create the primary peak corresponding to the Cherenkov angle of about  $\theta = 0.02$  rad as shown in Figs. 7.1. In general, the number of Cherenkov photons  $N_{\text{quartz}}$  generated in the quartz depends on the particle velocity  $\beta$ . Thus it differs for pions and kaons. The  $N_{\text{quartz}}$  contribution in the main Cherenkov peak around 0.3 rad can be estimated by the number of total reflection of Cherenkov photons generated in the quartz. This value is considered to be proportional to  $1/(d \sin \theta_{\text{quartz}})$ , where  $d = 3$  mm is the width of the quartz window of the HAPD and  $\theta_{\text{quartz}}$  is a Cherenkov angle in the quartz with  $n = 1.46$ . These value at 3.5 GeV/ $c$  are evaluated to be 0.458 and 0.462 for pions and kaons, respectively. They are close to each other and thus, we do not need to consider the species of particles when we evaluate the contamination in the main Cherenkov peak.

At the beam test, we obtained data by removing all the aerogels from the light-tight box in order to estimate the amount of background hits. This data was fitted with a composite function, which had two Gaussians for broad peak below 0.1 rad and an 8th-order polynomial for uncorrelated background. Fig. 7.1 (b) shows the components of the fitting function. The dotted lines represent the primary Cherenkov peak and secondary peak. A dashed line is contributed from only uncorrelated background. A solid line is used to combine them, and it corresponds to the fitting function in Fig. 7.1 (a). The primary Cherenkov peak and secondary peak for the background (kaon) assumption are shifted from the signal (pion) assumption according to the Cherenkov angle difference between pions and kaons depending on the momentum. The primary Cherenkov peak and secondary Cherenkov peak are added into the uncorrelated background to form the PDF. The created PDFs for pion and kaon at 3.5 GeV/ $c$  are shown in Fig. 7.1 (c).

Table 7.1: The definition of parameters used for calculating the Likelihood.

	Expected	Measurement	Parameter
Cherenkov angle	$\theta_C^\pi, \theta_C^K$	$\theta$	$\Theta$
# of detected photoelectrons	$N_{\text{pe}}^\pi, N_{\text{pe}}^K$	$n_{\text{hit}}$	$N$

## 7.4 Analysis and results

We estimated the PID performance of the ARICH counter for pion and kaon at 3.5 GeV/ $c$  using single-track events taken with 5 GeV/ $c$  electron. In order to select single-track events, we select data containing the number of detected photoelectrons below a cut value  $N_{\text{cut}}$  as the filled area in Fig. 7.2. We set  $N_{\text{cut}}$  at 17.08 corresponding to  $\mu_2 - 1.17\sigma_2$ , where  $\mu_2$  is the mean value of the Poisson distribution for double-track events ( $2N + B = 21.22$ ) using Eq.(6.25), and  $\sigma_2$  is  $\sqrt{\mu_2}$ .

Number of selected events with  $n_{\text{hit}} < N_{\text{cut}} = 17.08$  was 97,279, while number of multiple-tracks-events with the condition was 3,445 among them. The latter corresponds to the area of the Poisson distribution of double- and triple-tracks below  $N_{\text{cut}}$ . Therefore, the multiple-tracks contamination is about 3.5%, which is sufficiently small.

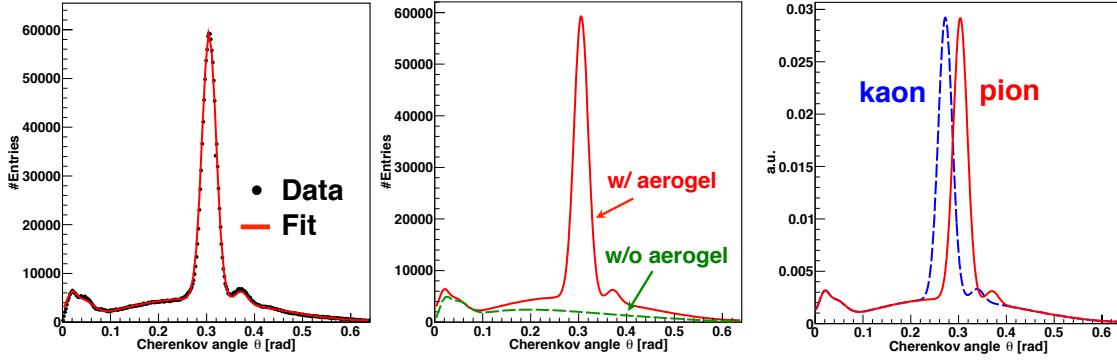


Figure 7.1: Construction scheme of the PDF for the Cherenkov angle. (a) Fitting into event selection applied data. The fitting function of four Gaussians and two 8th-order polynomials. (b) Parametrized distributions. The dotted lines (magenta) represent the Cherenkov signal peak. The dashed line (green) represents the common background. Solid line (red) represents the combined distribution. (c) PDF examples for pion and kaon at 3.5 GeV/ $c$ .

Because the expected Cherenkov angle  $\theta_C^\pi$  ( $= 0.2973$  rad) and expected number of photoelectrons  $N_{pe}^\pi$  ( $= 10.629$ ) for 3.5 GeV/ $c$  pions are close to expected  $\theta_C^e$  ( $= 0.2998$  rad) and expected  $N_{pe}^e$  ( $= 10.756$ ) for 5.0 GeV/ $c$  electrons, the selected data can be regarded as a data sample of 3.5 GeV/ $c$  pions. Fig. 7.3 shows the selected data distribution and PDFs of the Cherenkov angle for pion and kaon at 3.5 GeV/ $c$ .

We calculate the Likelihood ratio  $\mathcal{R}^\pi$  using Eq.(7.1). These quantities were calculated for every event. We also define the Likelihood ratio per event for kaon  $\mathcal{R}^K$  using the following equation:

$$\mathcal{R}^K = \frac{\mathcal{L}^K}{\mathcal{L}^\pi + \mathcal{L}^K} = 1 - \mathcal{R}^\pi. \quad (7.6)$$

Fig. 7.4 shows Likelihood ratio  $\mathcal{R}(\pi)$  for the momentum assumption of 3.5 GeV/ $c$ . The solid line and dotted line represent the  $\mathcal{R}(\pi)$  and  $\mathcal{R}(K)$  respectively.

We define the  $\pi$  identification efficiency for pion  $\varepsilon^\pi$  and kaon fake rate  $\varepsilon_K$  as the fraction of the number of events above the value  $\mathcal{R}_{cut}$  and the number of total events. It is equivalent to the following equation,

$$\varepsilon_\pi = \frac{\#Events(\mathcal{R}^\pi > \mathcal{R}_{cut})}{\#Events(All)},$$

$$\varepsilon_K = \frac{\#Events(\mathcal{R}^K > \mathcal{R}_{cut})}{\#Events(All)}.$$

When  $\mathcal{R}_{cut}$  is set at 0.2, we obtained  $\varepsilon_\pi$  and  $\varepsilon_K$  as 97.4% and 4.9%, respectively.

Fig. 7.5 and Fig. 7.6 show the log-Likelihood difference between pions and kaons at 2.2 GeV/ $c$  and 3.5 GeV/ $c$ , respectively. The log-Likelihoods are calculated  $\Delta \log \mathcal{L}^\pi = \log \mathcal{L}^\pi - \log \mathcal{L}^K$  and  $\Delta \log \mathcal{L}^K = \log \mathcal{L}^K - \log \mathcal{L}^\pi$  for pions and kaons, respectively. From Fig. 7.5, the distance between the mean of the distribution for pion and kaon at 2.2 GeV/ $c$

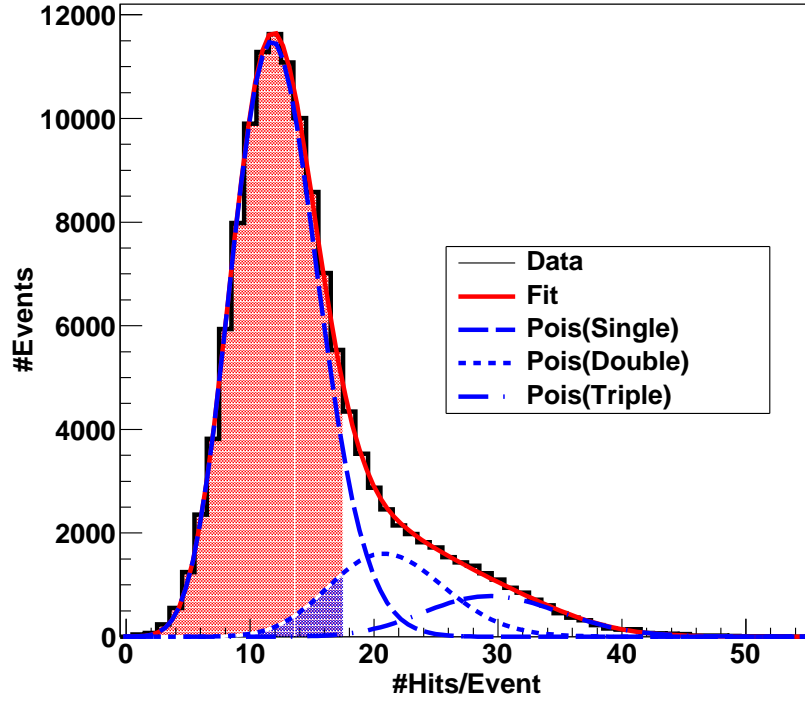


Figure 7.2: Distribution of the number of detected photons per an event, which is consisted with Fig.6.14. The region filled with a mesh indicates the selected event required the single-track condition  $n_{\text{hits}} \leq N_{\text{cut}} \equiv \mu_2 - 1.17\sigma_2 = 17.08$ .

corresponds to 43.1, and the root mean square value (rms) of the distribution corresponds to 8.86. These results indicate the  $\pi/K$  separation of  $4.87\sigma$ . In a similar manner, the distance of log-Likelihood distributions and the rms value at  $3.5\text{ GeV}/c$  from Fig.7.6 are to be 25.1 and 6.24, respectively, and then correspond to the  $\pi/K$  separation of  $4.02\sigma$ . Therefore I confirm that the prototype ARICH counter satisfy the requirement PID performance for the momentum up to  $3.5\text{ GeV}/c$ .

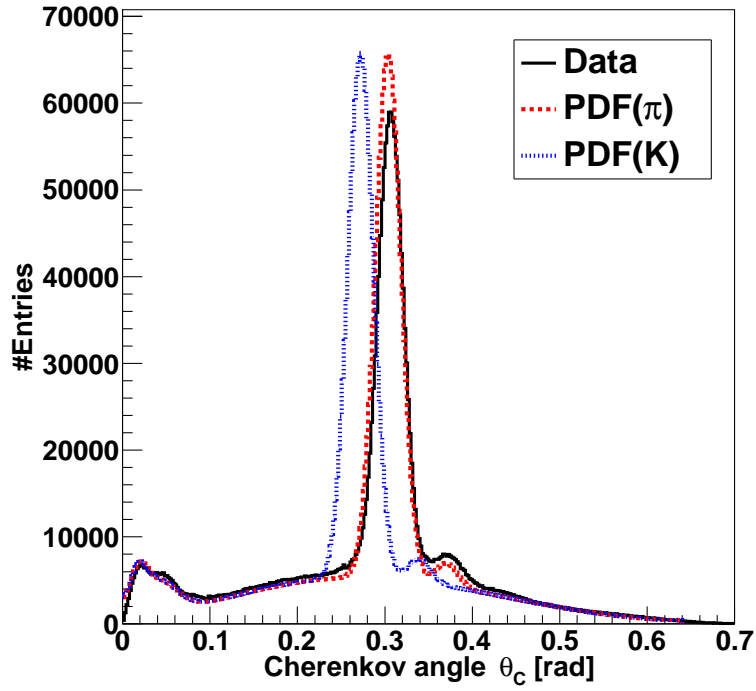


Figure 7.3: Cherenkov angular distribution of the beam test data with PDFs multiplied with number of events for pion and kaons at 3.5 GeV/c.

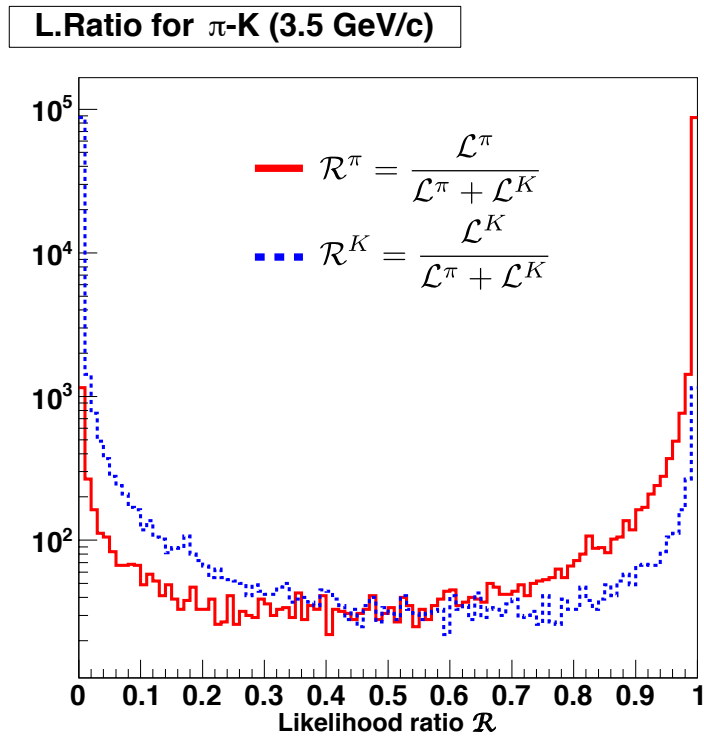


Figure 7.4: Likelihood ratio distribution for pions and kaons at 3.5 GeV/c.

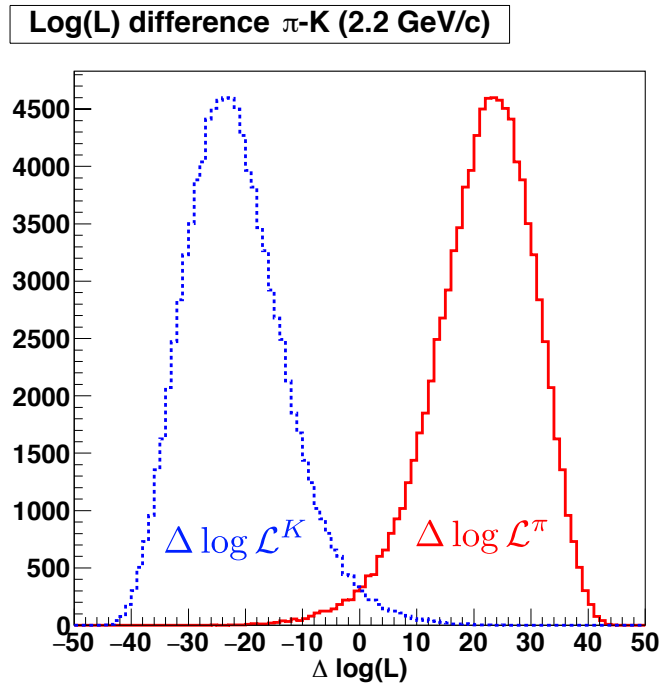


Figure 7.5: Distribution of the Likelihood difference between the pions (solid red line) and kaons (dashed blue line) at 2.2 GeV/ $c$ .

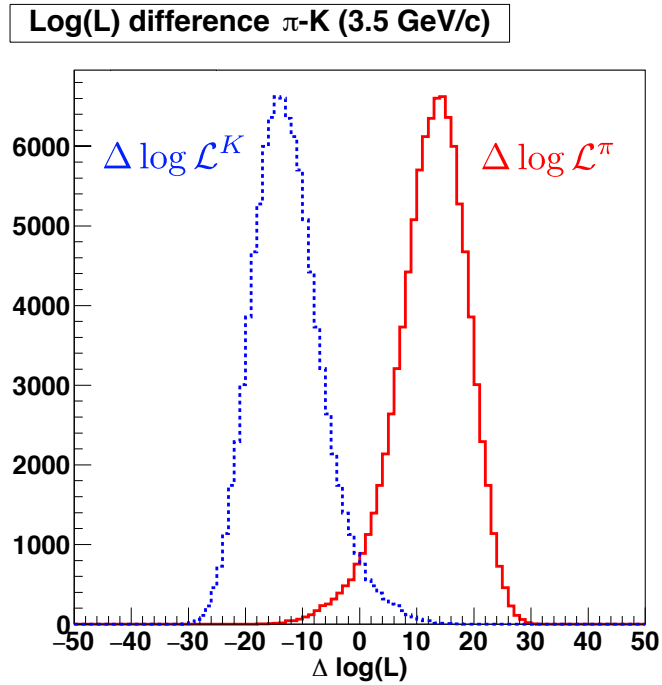


Figure 7.6: Distribution of the Likelihood difference between the pions (solid red line) and kaons (dashed blue line) at 3.5 GeV/ $c$

## 7.5 Discussion

To see the impact of the upgrade of the end-cap PID device from the ACC to the ARICH counter, I discuss the reduction of statistical error of a rare  $B$  decay process by use of PID information from ARICH. Assuming that the integrated luminosity of  $50 \text{ ab}^{-1}$  is delivered by SuperKEKB, the statistical error that is associated in a measurement of  $B^0 \rightarrow \pi^+\pi^-$  as a signal mode, against  $B^0 \rightarrow K^+\pi^-$  as a background mode, was estimated using the results of the beam test using the prototype ARICH counter. The  $B^0 \rightarrow \pi^+\pi^-$  decay is one of the mode that have the highest momentum pions among the  $B$  meson decays. Therefore, if we estimate the statistical error of this decay process, it is sufficient because the other decays, which are decaying into low momentum particles, should have better  $\pi/K$  identification and thus background suppression than of  $B^0 \rightarrow \pi^+\pi^-$ .

I compared the statistical error without and with the  $\pi/K$  identification provided by the ARICH with assuming the pion efficiency obtained from the prototype counter performance test. The statistical error can be estimate by the following equation:

$$\sigma_{\text{stat}} = \frac{\sqrt{S+B}}{S}, \quad (7.7)$$

where  $S$  and  $B$  are the number of reconstructed events for a signal mode ( $B^0 \rightarrow \pi^+\pi^-$ ) and a background mode  $B^0 \rightarrow K^+\pi^-$ , respectively.  $S$  or  $B$  for entering the (forward end-cap) ARICH region corresponding to  $17^\circ < \theta < 35^\circ$ , can estimate by the following equation:

$$S = \int \mathcal{L} dt \times \sigma_{B\bar{B}} \times BR \times \epsilon_{\text{Rec}} \times \epsilon_{\text{Acc}}. \quad (7.8)$$

Here,  $\int \mathcal{L} dt = 50 \text{ ab}^{-1}$  is the target integrated luminosity of SuperKEKB.  $\sigma_{B\bar{B}} = 1.1 \text{ nb}$  is the cross section of a  $B\bar{B}$  pair production.  $BR$  is a branching ratio for the decay mode, which are found in Ref.[34].  $\epsilon_{\text{Rec}}$  is a reconstruction efficiency for  $B^0 \rightarrow \pi^+\pi^-$  and  $K^+\pi^-$ , and were estimated from the results of  $B^0 \rightarrow \pi^+\pi^-$  decays measurement using the  $772 \times 10^6$   $B\bar{B}$  pairs collected by the Belle detector [63].  $\epsilon_{\text{Acc}}$  is the acceptance of the ARICH region viewing from the center-of-mass system of Belle II, which corresponds to 12%. All parameters used for the calculation of the statistical errors are summarized in Table 7.2.

Without ARICH,  $S$  and  $B$  are obtained to be  $2.53 \times 10^4$  and  $7.89 \times 10^4$ , respectively, then the statistical error in the measurement of  $B^0 \rightarrow \pi^+\pi^-$  at  $50 \text{ ab}^{-1}$  can be estimated to be 1.3% by the Eq.(7.7). With ARICH the  $\pi$  identification efficiency  $\epsilon_\pi$  of 97.4% and the  $K$  fake rate  $\epsilon_K$  of 4.9% by the prototype ARICH performance at  $3.5 \text{ GeV}/c$  are applied into the above numbers, then  $N$  and  $B$  are obtained to be  $2.46 \times 10^4$  and  $3.87 \times 10^3$ , respectively. The result corresponds to the statistical error of 0.69%. Thus by using the ARICH counter as the forward end-cap PID device of the Belle II detector, the statistical error in the measurement of  $B^0 \rightarrow \pi^+\pi^-$  can be reduce by about 60%. This result indicates that if the ARICH were absent, we may need 2.8 times the  $B\bar{B}$  collision data to have the same statistical uncertainty with ARICH.

Table 7.2: The summary of parameters used for the estimation of statistical error for  $B^0 \rightarrow \pi^+\pi^-$ .

Parameter	$B^0 \rightarrow \pi^+\pi^-$	$B^0 \rightarrow K^+\pi^-$	Ref.
Integrated luminosity $\int \mathcal{L}dt$	50 $\text{ab}^{-1}$		
Cross section $\sigma_{B\bar{B}}$	1.1 nb		
Branching ratio $BR$	$5.12 \times 10^{-6}$	$1.96 \times 10^{-5}$	[34]
Reconstruction efficiency $\epsilon_{\text{Rec}}$	0.75	0.61	[63]
ARICH region acceptance $\epsilon_{\text{Acc}}$	0.12		
Expected # events			Expected statistical error
without ARICH	$2.53 \times 10^4$	$7.89 \times 10^4$	1.3%
with ARICH	$2.46 \times 10^4$	$3.87 \times 10^3$	0.69%

# Chapter 8

## Conclusion

To search for physics beyond the standard model at the high-luminosity frontier, the construction of the detector for the Belle II experiment at the Super KEK-*B*-factory started in 2011. In the Belle II experiment, the particle identification (PID) of charged pions and kaons for the wide-range of momenta up to 3.5 GeV/*c* is required. Since the forward end-cap region of the Belle II detectors is limited along the beam direction, the proximity focusing type Ring Imaging Cherenkov (RICH) counter with silica aerogel radiator, which is named ARICH counter, is adopted for the PID device of Belle II.

A silica aerogel radiator satisfy our requirements for the radiator; suitable refractive index and high transmission length, thus it is a unique material as a radiator for the ARICH counter. In order to improve the Cherenkov angle resolution  $\sigma_\theta$  without any losses of detected photoelectrons, the dual radiator scheme that consists the combination of the slightly different of refractive indices  $n_1 = 1.045$  and  $n_2 = 1.055$  for the upstream and the downstream, respectively, is introduced in the ARICH counter.

A photon detector of the ARICH counter is required so that it can be operated in a high magnetic field of 1.5 T. It is also required to have large sensitive area with high position resolution, and to have radiation hardness during the 10-year Belle II operation. As the solution for that, the 144-ch multi-anode Hybrid Avalanche Photo Detectors (HAPDs) were developed and studied by the ARICH development group cooperating with Hamamatsu Photonics K.K. The remaining concern at the development of an HAPD had been the radiation hardness. In the front of the end-cap region of Belle II, a one MeV-equivalent neutron fluence of  $1 \times 10^{12} \text{ cm}^{-2}$  and a  $\gamma$ -ray dose of up to approximately 1 kGy are expected in total of 10-year operation. We found that the solution for the neutron damage is the choice of the avalanche photo-diode (APD) in an HAPD having a thinner P-layer than N-layer. We also found that the readout electronics that has the shorter shaping time of around 100 ns, can reduce a shot noise in increasing leakage current from the irradiated HAPD. Therefore the readout ASIC (SA03) that has the optimal shaping time of 100 ns, was developed. For damages by  $\gamma$ -ray, we found out that the protection film on the APD surface was easily charged up by  $\gamma$ -ray. After the improvement of the surface of the APD, we confirmed that the HAPD have sufficient  $\gamma$ -ray dose tolerance. To confirm the radiation hardness of the HAPD contained with the improved APD chips, we carried out the series of neutron and  $\gamma$ -ray irradiation tests. As a results, we found that the irradiated sample that was irradiated with one MeV-equivalent neutron fluence

of  $0.86 \times 10^{12} \text{ cm}^{-2}$  and with the  $\gamma$ -ray dose of 1 kGy, have sufficient performance. We conclude that the HAPD is tolerable for neutron and  $\gamma$ -ray radiation expected for 10-year Belle II operation.

In order to confirm that the final design of the ARICH satisfy our requirement, we performed the electron beam test using the prototype ARICH counter at DESY test beam line T24. The prototype ARICH was observed the clear Cherenkov ring image and measured the Cherenkov angle  $\theta_C$  to be 305.3 mrad with the angular resolution  $\sigma_\theta$  of 14.47 mrad and the number of detected photoelectrons of 10.71 per an event. These observed values are consistent to the prospects from the design of the ARICH system.

In order to estimate the PID performance of the ARICH counter at Belle II, an event-by-event analysis based on the likelihood method for the beam test data are demonstrated. As the result, I found that the ARICH counter can provide the  $\pi/K$  separation with the pion identification efficiency of above 99% with the kaon fake rate of 5% for the momentum up to 2.5 GeV/ $c$ , which is the typical momentum range for the flavor tagging. At the momentum of 3.5 GeV/ $c$ , the pion identification efficiency of 97.4% with the kaon fake rate of 4.9% was obtained. The distributions of log likelihood difference shows 4.02  $\sigma$  separation between pions and kaons at momentum of 3.5 GeV/ $c$ . We confirm that the developed ARICH counter satisfy the requirement of the Belle II experiment. The performance at the high momentum region is expected to be further improved by using the information in the whole range of Cherenkov angle distribution such as the Cherenkov photon generated in the quartz window and photoelectrons reflected on the APD surface.

# Acknowledgement

The results in this thesis have been made by the efforts of a lot of people, to whom I would like to thank.

First of all and foremost, I would like to thank to Prof. Takayuki Sumiyoshi who gives me the great opportunity to study the particle physics and to join the Belle II collaboration. He gives me a lot of precise experience in my years in the laboratory. I can't find enough words to describe my gratitude to him.

I would also like to thank to Assoc. Prof. Hidekazu Kakuno. He gives me a lot of advices and suggestions with his experienced intelligence. The discussions with him were essential ingredient to achieve this study.

I am grateful to all member of Belle II Aerogel RICH development group, especially, Assoc. Prof. Ichiro Adachi, Assoc. Prof. Shohei Nishida and Dr. Koji Hara for their many support and useful advices. They also give me the chance to join many experiments outside my university such as the DESY beam test. I would also like to thank to Aerogel RICH Ljubljana members, especially Prof. Peter Križan, Prof. Samo Korpar, Assoc. Prof. Rok Pestotnik. They give me many suggestion of the analytic strategy in my study and the knowledges of the HAPD.

I would grateful to Dr. Tetsuro Kumita for his many suggestions and advices, especially his correction of English grammar and contexts for my writings were a decisive element for all time in my study.

I would like to thank to Dr. Junpei Maeda, Dr. Tsunayuki Matsubara, and Dr. Tomoyuki Konno. Discussions with them and suggestion from a point of non-collaborator's view of them, were very helpful to me.

I would like to appreciate to current and (a lot of) former colleagues of my laboratory and other institutes, especially Mr. Ryosuke Kataura of Niigata University student. I got the support which couldn't finish counting, from him about the beam test simulation. I would also like to thank my friends at the other university, especially Dr. Kentaro Negishi and Mr. Yoshinori Arita, who were the student in the same grade of me.

Finally, I would like to thank my family and local friends very much for their a lot of support and understanding in my long school life and study. And I would like to appreciate all people who encouraged me during my time in Tokyo Metropolitan University.



# Bibliography

- [1] A. D. Sakharov, JETP Lett. **5**, 24 (1967).
- [2] J. H. Christenson *et al.*, Phys. Rev. Lett. **13**, 138 (1964).
- [3] L. Wolfenstein, Phys. Rev. Lett. **13**, 562 (1964).
- [4] M. Kobayashi and T. Maskawa, Prog. Theor. Phys. **49**, 652 (1973).
- [5] J. Batley *et al.*, Physics Letters B **544**, 97 (2002).
- [6] A. Alavi-Harati *et al.* [KTeV Collaboration], Phys. Rev. D **67**, 012005 (2003).
- [7] H. Nesemann and B. Sarau, IEEE NS-32 , 1644 (1985).
- [8] D. L. Rubin, Part. Accel. **26**, 63 (1990).
- [9] A. Bevan (ed.) *et al.*, Eur. Phys. J. C **74** (2014).
- [10] B. Aubert *et al.*, Nucl. Instr. Meth. A **479**, 1 (2002).
- [11] A. Abashian *et al.*, Nucl. Instr. Meth. A **479**, 117 (2002).
- [12] S. Kurokawa and E. Kikutani, Nucl. Instr. Meth. A **499**, 1 (2003).
- [13] T. Iijima *et al.*, Nucl. Instr. Meth. A **453**, 321 (2000).
- [14] I. Adam *et al.*, Nucl. Instr. Meth. A **538**, 281 (2005).
- [15] B. Aubert *et al.* [BABAR Collaboration], Phys. Rev. Lett. **87**, 091801 (2001).
- [16] K. Abe *et al.* [Belle Collaboration], Phys. Rev. D **66**, 032007 (2002).
- [17] CKM fitter group web site, [http://ckmfitter.in2p3.fr/www/html/ckm\\_main.html](http://ckmfitter.in2p3.fr/www/html/ckm_main.html).
- [18] E. Barberio *et al.* [Heavy Flavor Averaging Group], arXiv:0808.1297 [hep-ex] (2008).
- [19] H.-Y. Cheng *et al.*, Phys. Rev. D **72**, 014006 (2005).
- [20] T. Aushev *et al.*, arXiv:1002.5012 [hep-ex] (2010).
- [21] D. Atwood *et al.*, Phys. Rev. Lett. **79**, 185 (1997).
- [22] B. Grinstein *et al.*, Phys. Rev. D **71**, 011504 (2005).

- [23] K. Ikado *et al.* [Belle Collaboration], Phys. Rev. Lett. **97**, 251802 (2006).
- [24] I. Adachi *et al.* [Belle Collaboration], arXiv:0809.3834 [hep-ex] (2008).
- [25] S.-W. Lin *et al.* [Belle Collaboration], Nature **452** (2008).
- [26] M. Gronau, Phys. Lett. B **627**, 82 (2005).
- [27] I. Adachi *et al.* [Belle Collaboration], arXiv:0809.4366 [hep-ex] (2008).
- [28] H. Kichimi *et al.*, Nucl. Instr. Meth. A **453**, 315 (2000).
- [29] T. Abe *et al.*, arXiv:1011.0352 [physics.ins-det] (2010).
- [30] Superkekb group web site, <http://www-superkekb.kek.jp>.
- [31] P. A. Čerenkov, Phys. Rev. **52**, 378 (1937).
- [32] I. M. Frank and I. Tamm, C. R. Acad. Sci. URSS **14**, 109 (1937).
- [33] J. Seguinot and T. Ypsilantis, CERN-LAA/PI/91-004 (1991).
- [34] K. A. Olive *et al.* [Particle Data Group], Chin. Phys. C **38**, 090001 (2014).
- [35] I. Adachi *et al.*, Nucl. Instrum. Meth. **A355**, 390 (1995).
- [36] M. Tabata *et al.*, Nucl. Instr. Meth. A **668**, 64 (2012).
- [37] J. V. Jelley, Proc. Phys. Soc. A **64**, 82 (1951).
- [38] J. Atkinson and V. Perez-Mendez, Rev. Sci. Instr. **30** (1959).
- [39] T. Sumiyoshi *et al.*, Nucl. Instr. Meth. A **433**, 385 (1999).
- [40] A. Roberts, Nucl. Instr. Meth. **9**, 55 (1960).
- [41] J. Seguinot and T. Ypsilantis, Nucl. Instr. Meth. **142**, 377 (1977).
- [42] G. Charpak *et al.*, Nucl. Instrum. Meth. **164**, 419 (1979).
- [43] T. Ypsilantis, CERN-EP/89-150 (1989).
- [44] N. Akopov *et al.*, Nucl. Instr. Meth. A **479**, 511 (2002).
- [45] K. Ackerstaff *et al.*, Nucl. Instr. Meth. A **417**, 230 (1998).
- [46] T.-A. Shibata, Nucl. Instr. Meth. A **766**, 267 (2014).
- [47] T. Lohse *et al.*, Proposal for HERA-B, DESY PRC-94/02 (1994).
- [48] I. Ario *et al.*, Nucl. Instr. Meth. A **516**, 445 (2004).
- [49] A. A. Alves, Jr. *et al.* [LHCb Collaboration], Journal of Instr. **3**, S08005 (2008).

- [50] S. Amato *et al.* [LHCb Collaboration], LHCb: RICH technical design report, CERN-LHCC-2000-037 (2000).
- [51] C. Matteuzzi, Nucl. Instr. Meth. A **766**, 245 (2014).
- [52] M. Akatsu *et al.*, Nucl. Instr. Meth. A **440**, 124 (2000).
- [53] T. Hayakawa, Nucl. Instr. Meth. A **766**, 255 (2014).
- [54] Hamamatsu Photonics K.K. (<http://www.hamamatsu.com>) .
- [55] M. Tabata *et al.*, Nucl. Instr. Meth. A **766**, 212 (2014).
- [56] T. Matsumoto *et al.*, Nucl. Instr. Meth. A **521**, 367 (2004).
- [57] T. Iijima *et al.*, Nucl. Instr. Meth. A **548**, 383 (2005).
- [58] A. Seljak *et al.*, Journal of Instr. **6**, C12051 (2011).
- [59] S. Korpar *et al.*, Nucl. Instr. Meth. A **766**, 145 (2014).
- [60] S. Iwata *et al.*, Development of a RICH counter with 144-ch Hybrid Avalanche Photo-Detectors for the Belle II experiment, in *Nuclear Science Symposium and Medical Imaging Conference (NSS/MIC), 2012 IEEE*, pp. 1490–1494, 2012.
- [61] Test beams at desy, <http://particle-physics.desy.de/e252106/>.
- [62] E. Aschenauer *et al.*, Nucl. Instr. Meth. A **440**, 338 (2000).
- [63] J. Dalseno *et al.* [Belle Collaboration], Phys. Rev. D **88**, 092003 (2013).

